Title

Control Design for Systems with Bounded Actuators and Applications

Author

Sadeghi Reineh, Maryam

Publication Date

2018

UNIVERSITY OF CALIFORNIA,
IRVINE

Control Design for Systems with Bounded Actuators and Applications

DISSERTATION

submitted in partial satisfaction of the requirements
for the degree of

DOCTOR OF PHILOSOPHY

in Mechanical and Aerospace Engineering

by

Maryam Sadeghi Reineh

Dissertation Committee:
Professor Faryar Jabbari, Chair
Professor Jacob Brouwer
Professor Solmaz Kia

2018

DEDICATION

To my dear husband and parents

TABLE OF CONTENTS

LIST OF FIGURES

LIST OF TABLES

ACKNOWLEDGMENTS

Writing this dissertation would not have been possible without the help, support and friendship of many people. Firstly, I wish to thank my advisor, Prof. Faryar Jabbari, for being an outstanding mentor and friend. In addition to exposing me to his wide range of research interests and helping to guide my own research, he inspired me to define new challenges and pursue them successfully. I will always remember the meetings with him when I was frustrated at my own lack of progress, and left his office with a big smile full of energy and inspiration to continue. His inclusive model of leadership did much to help me realize my potential.

I would also like to thank the other members of my committee: Prof. Jacob Brouwer and Prof. Solmaz Kia. I truly enjoyed working with them on various research projects, and I benefited greatly from the clarity of vision they brought to my work.

My dear parents, have always encouraged me to pursue excellence and supported me in my every endeavor. To them I owe my love of knowledge and desire to excel. They have also been a great source of love, support, and understanding for me and my family, despite the great distance separating them from us.

I owe the greatest debt of gratitude to my husband, Ali, who has always been at my side throughout graduate school. Our life together is my greatest joy, and it, above all, is my greatest source of strength.

CURRICULUM VITAE

Maryam Sadeghi Reineh

EDUCATION

Doctor of Philosophy in Mechanical and Aerospace Engineering **2014-2018**
University of California, Irvine *Irvine, California*

GPA: 4.0/4
Master of Science in Mechanical Engineering **2010-2012**
Linkoping University *Linkoping, Sweden*

GPA: 4.0/4
Bachelor of Science in Aerospace Engineering **2006-2010**
Sharif University of Technology *Tehran, Iran*

EXPERIENCE

Process Engineer **July 2018– Present**
Applied Materials *Santa Clara, California*

Research Assistant **September 2014– June 2018**
University of California, Irvine *Irvine, California*

Intern **June 2017– September 2017**
Thor Trucks *North Hollywood, California*

Research Assistant **June 2012–August 2014**
Linkoping University *Linkoping, Sweden*

Intern **January 2012– June 2012**
Ohlins Racing, Advanced Suspension *Stockholm, Sweden*

HONORS AND AWARDS

Graduate Research Fellowship **2014–2015**
Department of Mechanical and Aerospace Engineering
University of California, Irvine
ZONTA International Amelia Earhart Fellowship **2017**
Society of Women Engineers in Orange County **2016**

REFEREED PUBLICATIONS

Journal Paper [**J**], Peer Reviewed Conference paper [**C**]

[J3] Maryam Sadeghi Reineh, Solmaz S. Kia, and Faryar Jabbari. New Anti-Windup Structure for Magnitude and Rate Limited Inputs and Peak-Bounded Disturbances, *Automatica*, 2018.
[J2] Maryam Sadeghi Reineh and Faryar Jabbari. Enhanced Power Generation in SOFCs using Artificial Limits on Actuator Control Signals. *ASME Journal of Electrochemical Energy Conversion and Storage*, 2018.
[J1] Maryam Sadeghi Reineh and Matteo Pelosi, Physical Modeling and Simulation Analysis of an Advanced Automotive Racing Shock Absorber using the 1D Simulation Tool AMESIM, *SAE Int. Journal of Passenger Cars-Mechanical Systems*, May 2013, vol. 6, pp. 7-17.
[C6] Maryam Sadeghi Reineh and Faryar Jabbari. Thermal Control of Solid Oxide Fuel Cells: An Anti-Windup Approach for Maximizing Usable Power, *IEEE Conference on Control Technology and Applications*, August 2017, Kohala Coast, HI.
[C5] Maryam Sadeghi Reineh, Solmaz S. Kia and Faryar Jabbari. Anti-Windup Designs for Systems with Amplitude and Rate Bounded Actuators, *IFAC World Congress*, July 2017, Toulouse, France.
[C4] Maryam Sadeghi Reineh and Faryar Jabbari. Use of Anti-Windup Techniques for Control of Solid-Oxide Fuel Cells, *SAE Small Engine Technology Conference*, November 2016, Charleston, SC.
[C3] Maryam Sadeghi Reineh, Solmaz S. Kia, and Faryar Jabbari. Multi-Stage Anti-Windup for LTI Systems with Actuator Magnitude and Rate Saturation, *American Control Conference*, July 2016, Boston, MA.
[C2] Maryam Sadeghi Reineh, Martin Enqvist, and Fredrik Gustafsson, IMU-based Vehicle Load Estimation under Normal Driving Conditions, *53rd IEEE Conference on Decision and Control*, December 2014, Los Angeles, CA.
[C1] Maryam Sadeghi Reineh, Martin Enqvist, and Fredrik Gustafsson, Detection of Roof Load for Automotive Safety Systems, *52nd IEEE Conference on Decision and Control*, December 2013, Florence, Italy.

FUTURE PUBLICATIONS

[J4] Maryam Sadeghi Reineh, Ali Fazli Yeknami, Michael Green, and Faryar Jabbari. A High Dynamic Range $\Delta\Sigma$ Modulator using Anti-Windup Compensated Integrators, *Submitted to IEEE Trans. Control Systems Technology*, 2018.
[J5] Maryam Sadeghi Reineh and Faryar Jabbari. Leader-Follower Tracking for General Multi-Agent Systems with Unknown Leader Input and Limited Actuation, *Manuscript under preparation*, 2018.

ABSTRACT OF THE DISSERTATION

Control Design for Systems with Bounded Actuators and Applications

By

Maryam Sadeghi Reineh

Doctor of Philosophy in Mechanical and Aerospace Engineering

University of California, Irvine, 2018

Professor Faryar Jabbari, Chair

Input saturation is known as a common and inevitable challenge in control system design. Commands beyond the magnitude and rate limits of physical actuators are truncated by saturation bounds and, as a result, system performance can degrade substantially, even leading to instability. Therefore, reliable execution of control loops requires either rigorous guarantees that for the expected exogenous inputs the actuator saturation bounds will not be violated, or appropriate measures have to be in place to counteract the actuator saturation's adverse effects.

In many applications, actuators can be saturated both in terms of the size of the input that the controller command implies and the rate at which the input can change; i.e., magnitude and rate actuator saturation, respectively. In this thesis, multiple Magnitude and Rate Anti-Windup (MRAW) structures are designed and their performance is evaluated on various physical systems. A novel structure for AW compensation for rate limited actuation is proposed which is less conservative than structures currently used accommodating energy and peak bounded exogenous signals. The new structure and the peak-to-peak analysis applied provide compensation for more practical problems with tighter rate bounds which could not be solved using the traditional AW structures. To reduce conservatism further, the proposed technique is combined with multi-stage AW loops to obtain different gains for different levels of saturation.

In the second part of the dissertation, the proposed theoretical results are applied to a few fields of application encountering control input saturation in an unconventional manner. As of the first application, the use of artificial actuator limits in control of energy systems is proposed with the objective of maximizing the net generated power. We study a Solid Oxide Fuel Cell (SOFC) controlled by a Multi-Input-Multi-Output (MIMO) compensator, which uses the blower/fan power and cathode inlet temperature as actuators. The usable power of the FC is maximized by limiting the air flow rate deliberately, when an increase in power is demanded. Possible rate bounds on the cathode inlet temperature are also modeled. These bounds could represent the physical limitations (due to slow dynamics of heat exchangers) and/or a control concept for accommodating the power saving objective. Applying proper limits to the amplitude and rate of the actuator signals, and incorporating Anti-Windup (AW) techniques, can raise the net power of the FC by 16% with negligible effects on the spatial temperature profile.

In the second area of application, the issue of integrator overload in common Analog-to-Digital Converters is studied and modeled in terms of control saturation. This thesis presents a robust stabilized continuous-time (CT) $\Delta\Sigma$ modulator employing the anti-windup (AW) feedback control technique, preventing integrators overload and maintaining an acceptable performance simultaneously. This is considered as an unconventional use of AW technique applied to a system without an ordinary *plant* and *controller*. The proposed technique accommodates arbitrarily large inputs and can be applied to multi-loop modulators. According to simulations, using AW augmentations, for a 50% higher dynamic range (DR), integrators do not overload and the signal-to-distortion-ratio (SNDR) drops less than 1dB from the maximum SNDR of the modulator.

Finally, the issue of actuator saturation and benefits of AW augmentations for a specific type of leader-follower tracking problem in multi-agent systems is studied which best fits the type of problem analyzed in this thesis. We study the leader-follower tracking problem composed of agents with general linear dynamics and an active leader with nonzero unknown input. A distributed continuous state feedback controller is proposed with optimized performance ensuring the convergence of the followers' trajectories to the leader agent. A general high performance output feedback control is also designed, based on the relative measurements of the neighbors, as an alternative to the state feedback approach, beneficial in case of measurement restrictions. Anti-Windup (AW) compensation scheme is then introduced in order to protect the stability of the network and improve the performance in the presence of actuator limitations. The effectiveness of results is finally supported by numerical simulations.

Chapter 1

Introduction

1.1 Motivation

Control design aims at employing mathematical modeling to present physical systems in terms of a number of inputs and outputs, and design controllers, in order for the system to reach a desired performance. In the control process, system outputs measured by the sensors are compared to the desired reference through a feedback line and the controller determines with an updated input to handle the error signal. The input is then applied to the system by means of the physical actuators with a specific range of application, as with any other physical device. The limited capacity of actuators can cause actuator saturation which degrades the system performance significantly and may even lead to instability. Despite extensive investigations, the issue of actuator saturation is still one of the major challenges in control design for a large range of applications.

In many applications, the actuator can fail to deliver required input both in terms of the size of the effort transmitted to the system, and the rate at which the input can change, technically called the magnitude and rate actuator saturation, respectively.

In this dissertation the issue of actuator magnitude and rate saturation and its effects on system performance and stability are studied in details. Multiple Magnitude and Rate Anti-Windup (MRAW) compensation loops are designed to overcome the difficulties caused by saturation. The performance of the proposed techniques are evaluated in a number of unconventional applications such as the use artificial saturation bounds in energy systems to maximize power generation, AW design for a system without an actual plant and controller, as well as the application to multi-agent systems.

1.2 Contributions

Input saturation is clearly a nonlinear phenomenon which needs to be addressed, in order not to threaten the internal stability and/or deteriorate system performance. In general, there are two alternatives to approach the issue. One way is to design the controller considering all of the limitations and nonlinearities from the beginning. The resulting nonlinear control design increases the level of the complexity of the controller and may become impractical in many cases. On the other hand, it is possible to design a highly desirable controller for the unconstrained system, regardless of the saturation nonlinearities, and then introduce some modifications to the controller known as Anti-Windup (AW) compensation with two main objectives: first, to maintain the characteristics of the unconstrained system, as long as there is no saturation, and second, to guarantee a stability region together with an improved performance once the system is encountered with saturation nonlinearities.

1.2.1 Magnitude and Rate Anti-Windup Design

Designing anti-windup gains for systems facing actuator rate saturation is regional, and there exists nearly no solution, for a general system, to guarantee the stability of the closed-loop system globally. Therefore, it is always necessary to make an assumption on the disturbance signal applying to the system, and design AW gains under that assumption. Here, the Magnitude and Rate Anti-Windup (MRAW) design is studied for two types of the disturbance signals, energy bounded and peak bounded, and their performance and range of application are compared.

To start with, the MRAW design is performed using the common energy-to-peak approach, in which the exogenous disturbance signal is assumed to be energy (norm) bounded. The proposed approach results in AW gains ensuring the local stability of the closed-loop system and improving the performance in the presence of saturation. However, as illustrated by the numerical examples presented here, as well as the ones used in literature (e.g. [19], [50]), the norm boundedness assumption on the disturbance signal can be limiting in terms of the real problems it can be applied to.

Next, in order to address this issue, instead of applying a bound to the energy of the exogenous signal, the signal is assumed to be peak bounded. Having this assumption, the MRAW design is performed using the peak-to-peak approach. In order to broaden the feasibility range of the peak-to-peak design when the rate limits are tight, and also to achieve higher performance AW gains, a new schematic of the MRAW design is proposed in *Sec.* 3.5 which is somewhat different from the standard design and manipulate the AW gains. Based on the numerical results presented, the peak-to-peak approach for the new design, the MRAW is feasible for much tighter saturation bounds and its performance is significantly better than the energy-to-peak result. Moreover, the new technique results in better performance for both the peak-to-peak and energy-to-peak approaches.

As the next major contribution in this study, the idea of multi-stage AW, first introduced in [33], is applied to the MRAW designs presented here. In single-stage MRAW, a single set of AW gains are used, usually as soon as saturation is encountered. Given that often the signal is mildly above the saturation levels, use of the same gains that should accommodate arbitrary large signals can lead to significant conservatism. The main idea of the multi-stage design is to schedule the anti-windup gains based on the saturation level of the control commands. As a result, when the amount of the control signal moderately exceeds the saturation bounds, more aggressive AW gains are allowed to enhance the system performance, while maintaining the stability. In this study the concept of multi-stage AW is applied only to the rate block with two stages of saturation, since it is often the critical constraint. However, the idea can be extended to multi-stage design for both the magnitude and rate saturation elements, with ease. For brevity, details are omitted.

1.2.2 Fuel Cell Application

In the second phase of the study, the idea is to apply the proposed AW techniques to physical systems encountering actuator magnitude and rate saturation. Fuel cells, electro-chemical energy conversion systems, are becoming more common due to their high efficiency and ultra low emissions. A detailed model of a Solid Oxide Fuel Cell (SOFC), as a common type of high temperature fuel cell, integrated with a blower model is studied here. Power following and its consequent large changes in the temperature profile are among the major challenges in transient operation of solid oxide fuel cells. Ensuring desirable load following while minimizing thermal fatigue and material damage can only be possible by employing control techniques. The controller designed initially assumes ideal actuation and uses two control inputs: the blower power and the cathode inlet temperature. At peak demand, the controller seeks an increase in the air flow, thus, a larger power for the blower is required. This forces the fuel cell to provide a lower net power level and results in a larger error signal transfered to the controller, where the controller further increases the demand. The idea to address the issue is to limit the air flow rate by putting an artificial bound on the blower power. Like any other physical system, actuation limitations can cause severe performance degradation and even system failure. Anti-windup techniques are then used to recover the performance of the unconstrained system while having more of the fuel cell power available for external use.

The second input to the fuel cell model is the cathode inlet temperature. The rate at which the temperature can change may also be limited due to actuator imperfections. The cathode inlet temperature rate saturation can cause significant changes in temperature profiles and thus threaten the overall system stability. The rate AW techniques proposed here, using peak-to-peak analysis, are applied to the fuel cell model in order to minimize the drawbacks of the input rate saturation.

1.2.3 Cooperative Control Application

Control of a network of cooperative agents has received tremendous attention in recent years and a variety of issues have been studied including control, communications, security or connection preservation. Among the various consensus and cooperation problems in networked multi-agent systems (e.g. [47, 16]), this work is focused on the problem of tracking (or following) a leader by a group of agents. In the majority of related results such as [66, 37, 23], the leader's input is considered to be either zero or available to all follower agents. However, this can be a highly restrictive assumption in many applications, specifically for large networks. The leader may require a nonzero control input in order to take specific actions, and/or its input might not be available to a subset, or even any of the followers, for instance, when the leader appears to be an uncooperative target.

In this thesis, we study the distributed tracking control of multi-agent systems with an active leader with bounded nonzero time-variant input signal. Furthermore, the restrictive assumption of the availability of the leader's input to all agents is not a requirement here. In fact, we consider a case in which the leader receives no information from any of the followers and its input is not available to any of the following agents.

The availability of full-state information, for control design, could be a restrictive assumption in many applications. Therefore, the results in this thesis have been extended to an output feedback controller using measured output information.

Among the issues that have received relatively limited attention, in cooperative control of multi-agent systems, is the potential for encountering actuator limitations, which is one of the most common problems faced in high performance control of single agent (non-network) systems. In this note, we also develop an anti-windup approach for use in cooperative control problems.

1.2.4 Analog-to-Digital Conversion Application

Delta-sigma analog-to-digital converters (ADCs) have been extensively used for applications that require a wide dynamic range (DR) such as digital audio, wireless communication, and biomedical systems [56, 61]. A wide DR can be achieved by increasing either the number of quantization levels or the loop filter order. The latter often causes instability, while the former needs a highly linear multi-bit digital-to-analog converter (DAC). To avoid instability, the single-loop high-order (> 2) modulators require intensive signal scaling by insertion of loop coefficients and/or reduction of internal signal swing [40], but these restrict the DR. On the other hand, cascading of stable first- or second-order modulators can build stable high-order modulators, but cascaded modulators are sensitive to non-idealities in the analog components, requiring expanded analog performance parameters, and thus, excessive power consumption.

Stability of single-loop high-order $\Delta\Sigma$ modulators ($\Delta\Sigma$Ms) is mainly restricted by integrator overloading. Large internal signals may overload the integrator/op-amp, particularly when the input amplitude approaches the modulator's full-scale level. The quantizer then cannot follow the large internal signal effectively, which causes the signal grow further inside the loop even beyond the supply voltage, leading to modulator instability. This signal limitation, caused by integrator overload, will lead to nonlinear behavior, thereby generating harmonic distortion in the output power spectrum.

In this thesis, we introduce an integrator using a local feedback inspired by the anti-windup (AW) control technique [50], [22] that mitigates overloading effects without aggressive signal scaling, resulting in a higher DR. The aim of using AW feedback is to monitor the integrator output constantly and detect any undesired overloading that may lead to instability. We show here, by modeling and simulation results, how the integrator overloading can be avoided and the resulting SNDR degradation can be improved. The sufficient condition for stability is derived using the well-known Lyapunov approach accompanied with a guaranteed performance bound provided by the optimal AW gains for the local feedback.

1.3 Thesis outline

The thesis outline is as follows. In Chapter 2, a short review of the magnitude and rate AW designs studied in the literature is given. Chapter 3 presents the main theoretical contributions: standard and new MRAW designs, energy-to-peak and peak-to-peak designs, single-stage and multi-stage schemes and their feasibility conditions. Simulation results for all of the designs introduced in Chapter 3 are also presented and compared in this chapter. Chapter 4 covers the fuel cell application of the presented MRAW designs. The cooperative tracking control problem in multi-agent systems with limited actuation, as the second application of the thesis, is studied in Chapter 6. Chapter 5 investigates the saturation non-ideality in analog-to-digital converters and shows how AW compensation may be beneficial in resolving this issue.

Chapter 2

Literature Review

There is an extensive body of research on actuator saturation and techniques to address or accommodate it. Naturally, a great many techniques have been developed in design of anti-windup augmentation, a detailed review of which is beyond the space limitations here. We thus focus mostly on the well known techniques closest to the results presented here.

2.1 Amplitude and Rate Anti-windup Design

Early results including [35] made significant contribution toward a systematic approach to anti-windup design. Parameter dependent Lyapunov functions are used, for instance in [8], and many results employ Linear Matrix Inequality (LMI) to render the problem into a convex optimization problem (e.g., in [44] and [22]). In

[27, 26, 25, 12] and [17] a variety of regional results are developed for systems that are not necessarily open loop stable.

Among the large number of results, one of the more popular approaches is to design a high performance controller, ignoring the actuator limitations. This results in highly desirable performance in small signal regimes. To prevent instability and ensure some performance in the presence of saturation, the system is then augmented by anti-windup (AW) loops that become activated once the controller commands exceed actuator limits (see, for a small but critical sample [22, 27, 64]). This approach is particularly suitable when the periods of saturation are relatively infrequent and the system is operating under the high performance compensation most of the time (without facing saturation).

In addition (or separate from) bounds on the actuator magnitude, rate saturation has also been shown to be a critical issue. Limits on the rate of the actuator force can result in extreme performance degradation or even instability, leading to significant interest in anti-windup designs that address rate limits (see for example [4] or [18]). For some of the early work, one can consult, for example [29, 5, 46]. Among more recent work, [54] relies on the algebraic Riccati equation, and several free parameters to influence the performance level and size of the region of attraction. Closer to the results presented here, in [19] the rate saturation is characterized by generating the derivative of the control signal, assuming the controller to be linear and strictly proper. Moreover, a key feedback loop with a free parameter is introduced in order to avoid an unstable cancellation between the ideal derivative operator and the integrator.

As with nearly all rate and magnitude limitation results, the AW gains guarantee performance and stability in ‘regional’ sense, i.e., given a bound on the reference command (or disturbance). The key technical element used relies on slack variables introduced in the work of Lin and Hu (see, for example, [39] and [24]). These in turn were used to develop regional results for systems without asymptotically stable open loop, early on in [12] and then in a relatively large body of work (see, for example, [27, 17]).

In the vast majority of these results, a single set of AW gains are used, usually as soon as saturation is encountered. Given that often the signal is mildly above the saturation levels, use of the same gains that should accommodate arbitrary large signals can lead to significant conservatism. As initially presented in [33], the main idea of the multi-stage design is to schedule the anti-windup gains based on the saturation level of the control commands. As a result, when the amount of the control signal moderately exceeds the saturation bounds, more aggressive AW gains are allowed to enhance the system performance, while maintaining the stability.

2.2 Leader-Follower Tracking with Limited Actuation

Distributed tracking control of homogeneous multi-agent systems has been studied in [66, 37], assuming that the leader and the followers share exactly the same dynamics, thus, not applicable to the tracking problem of a leader with an unknown nonzero input. In [38], a distributed discontinuous tracking controller is proposed and non-smooth analysis tools are used to solve the tracking problem for multi-agent systems with nonzero leader input. The suggested algorithm also requires the leader's input to be bounded in order to handle the nonlinear term in the controller, which might not be practical given the unavailable nature of the signal. Here, we investigate the same problem studied in [38], however, we propose a linear state feedback controller capable of achieving tracking, avoiding discontinuities in the control process, as well as the boundedness assumption for the leader's input. In [66], taking advantage of the duality of the controller and observer design, an output feedback controller has been designed for synchronization problem of general linear systems using an LQR based optimization method. However, in [66], the leader is assumed to have zero input, therefore, the results presented are not applicable here. References [55, 21, 20], address this problem through robustness or reliability techniques by roughly speaking, designing controllers that can withstand severe degradation in actuation authority. Such approaches may lead to conservative results, as the control system requires resiliency to such failures. An alternative approach, that has been studied extensively for single agent systems ([8, 22, 27]), is to maintain a high performance controller but design anti-windup augmentation loops that become active only if actuators are saturated. This is the approach taken in this work.

2.3 Overload Prevention in Analog-to-Digital Converters

Design efforts have been made in the past to overcome integrator overload issue in high resolution analog-to-digital converters. In [3], the stability is achieved by bounding the internal node voltages through insertion of local feedback loops. The error caused by these loops is then canceled by appropriate digital corrections using a stable estimation of an infinite impulse response, increasing implementation complexity. Authors in [68] propose a compensation architecture for CT $\Delta\Sigma$Ms based on variable-structure control techniques offering soft-resetting as a better alternative to the conventional resetting presented in [3]. However, it requires the restrictive assumption of infinite sampling rate for the proof of stability.

In this thesis, we introduce an integrator using a local feedback inspired by the anti-windup (AW) control technique [21] that mitigates overloading effects without aggressive signal scaling, resulting in a higher DR. The aim of using AW feedback is to continuously monitor the integrator output and detect any undesired overloading that may lead to instability. We show here, by modeling and simulation results, how the integrator overloading can be avoided and the resulting SNDR degradation can be improved. The sufficient condition for stability is derived using the well-known Lyapunov approach accompanied with a guaranteed performance bound provided by the optimal AW gains for the local feedback. For arbitrary large modulator inputs, the AW-compensated integrator eliminates the need for digital integrators and additional cancellation filters used in [3] as well as the infinite sampling rate assumption made in [68]. For higher-order $\Delta\Sigma$ modulators, we place a saturation element after each integrator, in order to avoid voltage overload throughout the circuit.

Chapter 3

Magnitude and Rate Anti-Windup Design

3.1 Background

If saturation occurs occasionally (or episodically), a high performance nominal controller can be used while introducing some modifications to it, known as Anti-Windup (AW) compensation. This will maintain the characteristics of the unconstrained system and guarantee a stability region together with an improved performance once the saturation nonlinearities are encountered.

As discussed in [19], [50], the common energy-to-peak approach, in which the exogenous disturbance signal is assumed to be energy (norm) bounded, can be limiting in terms of the practical problems to which it can be applied. Here, in order to allow more realistic applications, reference signals are assumed to be peak bounded.

In order to broaden the feasibility range of the peak-to-peak design when the rate limits are tight, and also to achieve higher performance AW gains, a new schematic of the Magnitude and Rate Anti-Windup (MRAW) design is proposed in Section 3.5 which is somewhat different from the standard design in terms of AW feedback gains. As illustrated by the numerical results presented in Section 3.6, using the peak-to-peak approach for the new design, the MRAW is feasible for much tighter saturation bounds for both peak-to-peak and energy-to-peak cases. The guaranteed performance is also significantly better for both approaches ([52]).

Next, the idea of multi-stage AW, first introduced in [33], is applied to the MRAW designs presented here. In the traditional (single-stage) MRAW, a single set of AW gains are used, usually as soon as saturation is encountered. Given that often the signal is mildly above the saturation levels, use of the same gains that should accommodate arbitrary large signals can lead to significant conservatism. The main idea of the multi-stage design is to schedule the anti-windup gains based on the saturation level of the control commands. In this way, when the amount of the control signal moderately exceeds the saturation bounds, more aggressive AW gains are allowed to enhance the system performance. For brevity, the concept of multi-stage AW is applied only to the rate block with two stages of saturation, though it can be easily extended to the magnitude or both rate and magnitude saturation elements, and multiple stages.

3.2 Background and Preliminaries

We use $\mathbb{R}$, $\mathbb{R}_{\geq 0}$, and $\mathbb{R}_{>0}$ to denote the set of real, nonnegative real, and positive real numbers, respectively. We let 0_n denote the $n \times n$ matrix of zeros and I_n denote the $n \times n$ identity matrix. When clear from the context, we do not specify the matrix dimensions. For a matrix $A \in \mathbb{R}^{n\times m}$, $A^\top$ denotes its transpose, while $A_{(i)}$ denotes its ith row. For a symmetric matrix A, $A > 0$ indicates that A is positive definite. The block diagonal matrix of set of matrices $A_1, \ldots, A_N$ is $\text{diag}(A_1, \ldots, A_N)$. Any matrix whose columns form bases of the null space of matrix A is denoted by $\mathscr{N}_A$. Given a vector $v = [v_1, v_2, ..., v_n]$, v_i denotes the ith element of v, and $\text{diag}(v)$ is a n by n matrix with the elements of v on its diagonal. For $x \in \mathbb{R}$, $|x|$ is its absolute value and for $x \in \mathbb{R}^n$, $\|x\| = \sqrt{x^\top x}$ is the standard Euclidean norm while $\|f\|_2^2 = \lim_{t\to\infty} \int_0^t |f(\tau)^\top f(\tau)| d\tau$ is the $\mathscr{L}_2$ norm.

For vector $a \in \mathbb{R}^n$ and given bounds $p \in \mathbb{R}^n_{>0}$, we define the decentralized saturation function $\text{sat}_p(.) : \mathbb{R}^n \to \mathbb{R}^n$ as

$$\text{sat}_p(a) = \big(\text{sgn}(a_1)\min\{|a_1|, p_1\}, \cdots, \text{sgn}(a_n)\min\{|a_n|, p_n\}\big)^\top, \tag{3.1}$$

where sgn(.) is the sign function. The decentralized dead-zone function is defined as $\text{diag}(\text{dz}(a))$ where

$$\text{dz}(a) := a - \text{sat}_p(a). \tag{3.2}$$

$\text{He}(A)$ is $A + A^\top$. Here, $x \mapsto y \in [0, I_n]$ is the map from x to y *belonging to the sector*

$[0, I_n]$. This is equivalent to $y^\top(x-y) \geq 0$ for all $x \in \mathbb{R}^n$ ([31]). It is easy to see that if W is diagonal positive definite, then $y^\top W(x-y) \geq 0$ as well.

To study the feasibility of our proposed design LMIs in Sec. 3.7, the following elimination lemma is used [6].

Lemma 3.2.1 (Elimination Lemma) *Given a $n \times n$ real symmetric matrix Ψ, and two matrices $G \in \mathbb{R}^{m\times n}$ and $H \in \mathbb{R}^{p\times n}$, there exists a matrix $X \in \mathbb{R}^{p\times m}$ to solve the inequality*

$$\Psi + G^\top X^\top H + H^\top X G < 0, \tag{3.3}$$

if and only if

$$\mathcal{N}_G^\top \Psi \mathcal{N}_G < 0 \quad \text{and} \quad \mathcal{N}_H^\top \Psi \mathcal{N}_H < 0. \tag{3.4}$$

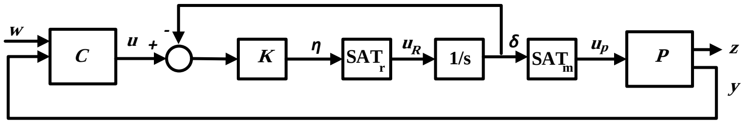

Figure 3.1: The basic setup of the control loop.

3.3 Problem Statement

Consider the system block diagram shown in Fig. 3.1, the linear plant P is given by

$$\begin{aligned} \dot{x}_p &= A_p x_p + B_1 w + B_2 u_p, \\ z &= C_1 x_p + D_{11} w + D_{12} u_p, \\ y &= C_2 x_p + D_{21} w + D_{22} u_p, \end{aligned} \tag{3.5}$$

with the state vector $x_p \in \mathbb{R}^{n_p}$, the control input $u_p \in \mathbb{R}^{n_u}$, the exogenous input $w \in \mathbb{R}^{n_w}$, the measurement output $y \in \mathbb{R}^{n_y}$, and the performance output $z \in \mathbb{R}^{n_z}$. The system matrix A_p is Hurwitz. The linear controller C is given by

$$\begin{aligned} \dot{x}_c &= A_c x_c + B_{cy} y + B_{cw} w, \\ u &= C_c x_c + D_{cy} y + D_{cw} w, \end{aligned} \tag{3.6}$$

with the controller state vector $x_c \in \mathbb{R}^{n_c}$, and the output vector $u \in \mathbb{R}^{n_u}$. Throughout this chapter, we assume that the actuators have magnitude and rate limits and, thus, the commands sent to the actuators should not exceed these bounds. Therefore, for every input, we require

$$|u_{pi}| \leq \mathsf{m}_i, \quad |\dot{u}_{pi}| \leq \mathsf{r}_i, \quad i \in \{1, \cdots, n_u\}, \tag{3.7}$$

with r_i and m_i as known positive constants.

The basic approach can be seen in Fig. 3.1, in which a first order filter and two saturation elements are inserted between the output of the compensator and the plant input. The proposed set up, which is easily realized with software, is often used as a model for magnitude and rate bounded actuators (e.g., [46],[58]). The input to the plant u_p is thus modeled as

$$\begin{aligned} u_p &= \mathrm{sat}_{\mathsf{m}}(\delta), \\ \dot{\delta} &= \mathrm{sat}_{\mathsf{r}}(K(u-\delta)), \end{aligned} \tag{3.8}$$

where $K = \mathrm{diag}(K_1, \cdots, K_{n_u}) \in \mathbb{R}_{>0}^{n_u \times n_u}$. It is assumed that the controller (3.6) is designed without any regard to the actuator saturation bounds. The plant input signal u_p, is clearly magnitude bounded. Moreover, since its derivative is bounded due to the saturation before the integral block, the signal is rate bounded as well. The set-up in Fig. 3.1 is similar but somewhat different from the one used in [19]. Here, even in the small signal regime, the first order block is a low pass filter that can affect the dynamics. Naturally, by choosing K large enough the effects can be made minimal while maintaining the original stability and performance for the unsaturated system. In contrast, in [19] a similar gain K is placed in such a way that it does not enter the dynamics unless saturation is encountered. Of course, [19] requires the derivative of the output of the compensator u to be obtained, which leads to assuming that the compensator does not have feed through or noise terms ($D_{cy} = 0, D_{cw} = 0$). The advantage of the proposed rate model over the one used in [19] is that here, there is no need to obtain the derivative of the controller's output signal, $\dot{u}$, in real time. While, K remains as a free parameter in both designs. The multi-stage approach, used here, can also be applied to the structure used in [19], though some of the technical details might have slightly different forms.

Assumption 1 (Internally stable unconstrained closed-loop) The nominal closed-loop

system comprised of (3.5), (3.6), and (3.8) in the absence of saturation is internally stable. □

3.4 MRAW Design

In the presence of actuator saturation nonlinearities (3.8), the stability and the performance guarantees may no longer be valid for the closed-loop system. The objective here is to design an anti-windup augmentation that introduces suitable additive modification signals $v_1 \in \mathbb{R}^{n_c}$ and $v_2 \in \mathbb{R}^{n_u}$ to the unconstrained controller (3.6), i.e.,

$$\begin{aligned} \dot{x}_c &= A_c x_c + B_{cy} y + B_{cw} w + v_1, \\ u &= C_c x_c + D_{cy} y + D_{cw} w + v_2. \end{aligned} \tag{3.9}$$

These modifications should make the closed-loop system internally stable with a guaranteed input-output performance level in the presence of saturation nonlinearities in the control loop.

Since the aim is a method that also applies to input rate saturation, such results will necessarily be local. Here, we assume that a possibly conservative estimate of the disturbance signal $w(t)$ is known.

Assumption 2 (Magnitude bound on exogenous input) The exogenous input entering the system satisfies $\|w\|_2 < s$ for some known $s \in \mathbb{R}_{>0}$. □

3.4.1 Energy-to-Peak Analysis

For zero initial conditions and a fixed input size $s \in \mathbb{R}_{>0}$, an anti-windup compensator must be designed such that the control output z of the modified control system satisfies

$$\|z\|_2 \leq \gamma \|w\|_2, \qquad \forall w \quad \text{such that} \quad \|w\|_2 \leq s. \tag{3.10}$$

Stability and acceptable performance are then guaranteed for disturbances satisfying this bound.

Single-Stage AW Design

The model shown by Fig. 3.2 is basically a position-feedback type of system with a saturation nonlinearity inside the loop. The goal is to design a suitable anti-windup system which imposes modifications to the unconstrained controller (3.6), in order to recover the performance of the unsaturated system, as much as possible. In this section the anti-windup gains are introduced to the nominal controller by adding signals to the state and output equations, as shown in (3.9).

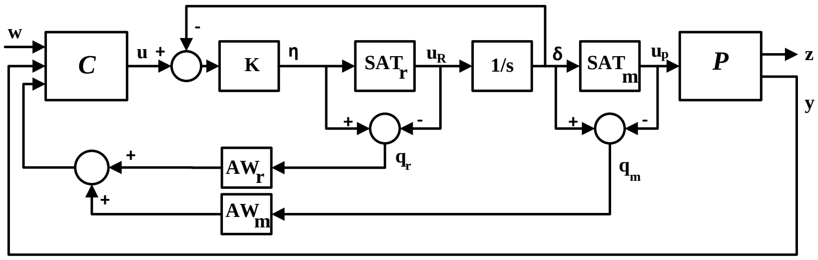

Figure 3.2: Single-stage anti-windup for system with magnitude and rate saturation.

Considering the system block diagram shown by Fig. 3.2, the static anti-windup blocks containing matrix gains

$$\begin{aligned} \mathrm{AW_R}(q_r) &= -\Lambda_r q_r, \\ \mathrm{AW_M}(q_m) &= -\Lambda_m q_m, \end{aligned} \tag{3.11}$$

are applied to the dead-zone functions

$$\begin{aligned} q_r &= \mathrm{dz}(\eta) = \eta - \mathrm{sat_R}(\eta) = \eta - u_R, \\ q_m &= \mathrm{dz}(\delta) = \delta - \mathrm{sat_M}(\delta) = \delta - u_p. \end{aligned} \tag{3.12}$$

According to Fig. 3.2, $u_R = \eta - q_r$ and $\eta = (u-\delta)K$, therefore, $u_R = (u-\delta)K - q_r$. Noting $\delta = \frac{1}{s}u_R$, the signal δ is defined as a new state variable with dynamics

$$\dot{\delta} = u_R = (u-\delta)K - q_r,$$

in which the signal u can be substituted from (3.6). It is relatively straight forward to build the augmented system with state vector $x = [x_p^\top \quad x_c^\top \quad \delta^\top]^\top$ and w, q_m, and q_r as input signals. The closed loop system with magnitude and rate saturation can be written as

$$\begin{aligned}
\dot{x} &= Ax + B_w w + (B_{q_m} - B_\eta \Lambda_m) q_m + (B_{q_r} - B_\eta \Lambda_r) q_r, \\
z &= C_z x + D_{zw} w + D_{zq} q_m, \\
u &= C_u x + D_{uw} w + (D_{uq} - D_{u\eta} \Lambda_m) q_m - D_{u\eta} \Lambda_r q_r,
\end{aligned} \tag{3.13}$$

with system matrices

$$\begin{aligned}
\left[\begin{array}{c} A \\ \hline C_z \\ \hline C_u \end{array}\right] &= \left[\begin{array}{ccc} A_p & 0 & B_2 \\ B_{cy}C_2 & A_c & B_{cy}D_{22} \\ KD_{cy}C_2 & KC_c & K(D_{cy}D_{22} - I) \\ \hline C_1 & 0 & D_{12} \\ \hline D_{cy}C_2 & C_c & D_{cy}D_{22} \end{array}\right], \\
\left[\begin{array}{c} B_w \\ \hline D_{zw} \\ \hline D_{uw} \end{array}\right] &= \left[\begin{array}{c} B_1 \\ B_{cy}D_{21} + B_{cw} \\ K(D_{cy}D_{21} + D_{cw}) \\ \hline D_{11} \\ \hline D_{cy}D_{21} + D_{cw} \end{array}\right], \\
\left[\begin{array}{c|c|c} B_{q_m} & B_\eta & B_{q_r} \\ \hline D_{zq} & D_{uq} & D_{u\eta} \end{array}\right] &= \left[\begin{array}{c|c|c} -B_2 & 0 & 0 \\ -B_{cy}D_{22} & [I \quad 0] & 0 \\ -KD_{cy}D_{22} & K[0 \quad I] & -I \\ \hline -D_{12} & -D_{cy}D_{22} & [0 \quad I] \end{array}\right].
\end{aligned} \tag{3.14}$$

The key technical element here relies on the so-called slack variables (see e.g. [39]). The following Lemma, inspired by (and quite similar to) [12], introduces the slack variable H_m and H_r.

Lemma 3.4.1 (Single-stage AW sector conditions) *Consider the polyhedral set S defined as*

$$S = \{x \in \mathbb{R}^n : |H_{m(i)}x| \leq \mathsf{m}_i, |H_{r(j)}x| \leq \mathsf{r}_i\}, \tag{3.15}$$
$$i = 1, ..., n_u.$$

where matrices H_m and H_r are free parameters to be determined. The deadzones q_m and q_r belong to the $[0 \quad I]$ *sector, following standard definitions:*

$$\eta \longmapsto q_r \in [0 \quad I], \quad \delta \longmapsto q_m \in [0 \quad I]. \tag{3.16}$$

Given (3.15) *and* (3.16)*, the following regional stability conditions hold for diagonal positive definite matrices W_r and W_m, for all $x \in S$.*

$$(a) \quad q_r^\top W_r(q_r - \eta + H_r x) \leq 0, \tag{3.17}$$
$$(b) \quad q_m^\top W_m(q_m - \delta + H_m x) \leq 0.$$

Proof. For simplicity, the proof here is shown for the scalar case, excluding the weighting matrices. However, the extension to the vector case is straightforward, since the saturation operator defined in (3.1) is decentralized and the weighting matrices W_r and W_m are diagonal and positive definite.

(a)

- if $|\eta| \leq \mathsf{r} \Rightarrow q_r = 0 \Rightarrow q_r(q_r - \eta + H_r x) \leq 0$,
- if $\eta > \mathsf{r} \Rightarrow q_r = \eta - \mathsf{r} > 0$, and since $x \in S \Rightarrow H_r x \leq \mathsf{r}$, thus, $q_r - \eta + H_r x \leq 0$. Having $q_r > 0$, we have

  $q_r(q_r - \eta + H_r x) \leq 0$,
- if $\eta < -\mathsf{r} \Rightarrow q_r = \eta + \mathsf{r} < 0$, and since $x \in S \Rightarrow H_r x \geq -\mathsf{r}$, thus, $q_r - \eta + H_r x \geq 0$. Having $q_r < 0$, we have

  $q_r(q_r - \eta + H_r x) \leq 0$.

(b) Similar to (a).

The following theorem presents the single-stage MRAW design which sets up a convex optimization problem and solves for the AW gains as design variables using the sector conditions discussed in Lemma 3.4.1.

Corollary 3.4.1 *Consider the Lyapunov function* $V = x^\top Q^{-1} x$ *with* $Q > 0$*, and a norm bounded exogenous input* $w(t)$ *satisfying* $||w(t)||_2 \leq s, \quad \forall t \geq 0$. *Then, starting from* $x(0) = 0$*, as long as*

$$\dot{V} - w^\top w < 0, \tag{3.18}$$

the trajectories of the closed-loop system $x(t)$ *belong to the set*

$$x(t) \in \mathscr{E}(Q^{-1}, s^2) = \{x : x^\top Q^{-1} x < s^2\}, \quad t \geq 0. \tag{3.19}$$

Proof. Let t be any time such that (3.18) holds for $[0,t]$. Then, integrating (3.18) from 0 to t results in

$$V(t) - V(0) - \int_0^t w^\top(\tau) w(\tau) \mathrm{d}\tau < 0. \tag{3.20}$$

Recalling the zero initial condition $x(0) = 0$, $V(0) = 0$ and norm boundedness condition $||w(t)||_2 \leq s$, (3.20) reduces to

$$V(t) = x^\top(t) Q^{-1} x(t) < s^2. \tag{3.21}$$

Therefore,

$$x(t) \in \mathscr{E}(Q^{-1}, s^2), \quad t \geq 0. \tag{3.22}$$

$\square$

Theorem 3.4.1 (Single-stage AW standard design: Energy-to-peak case) *Consider the disturbance signal satisfying* $\|w\|_2 \leq s$*, with* $x(0) = 0$*, and the plant and the controller introduced in* (3.5) *and* (3.6) *with the magnitude and rate limits* m *and* r*. Any solution to the LMI optimization problem*

$$\min_{Q, M_m, M_r, X_m, X_r, Y_m, Y_r, \gamma^2} \quad \gamma^2 \tag{3.23}$$

subject to

$$\begin{pmatrix} QA^\top + AQ & * & * & * & * \\ B_w^\top & -I & * & * & * \\ C_zQ & D_{zw} & -\gamma^2 I & * & * \\ \Phi_{4,1} & 0 & M_m D_{zq}^\top & \Phi_{4,4} & * \\ \Phi_{5,1} & KD_{uw} & 0 & \Phi_{5,4} & \Phi_{5,5} \end{pmatrix} < 0, \tag{3.24}$$

$$\begin{pmatrix} \mathsf{m}_i^2/s^2 & Y_{mi} \\ Y_{mi}^\top & Q \end{pmatrix} > 0, \quad \begin{pmatrix} \mathsf{r}_i^2/s^2 & Y_{ri} \\ Y_{ri}^\top & Q \end{pmatrix} > 0, \quad Q > 0, \tag{3.25}$$

where $i = 1, \ldots, n_u$, *and*

$$\begin{aligned} & M_m = W_m^{-1}, M_r = W_r^{-1}, X_m = \Lambda_m M_m, X_r = \Lambda_r M_r, \\ & \Phi_{4,1} = M_m B_{q_m}^\top - X_m^\top B_\eta^\top + [0 \quad 0 \quad I]Q - Y_m, \\ & \Phi_{5,1} = M_r B_{q_r}^\top - X_r^\top B_\eta^\top + [KC_u - [0 \quad 0 \quad K]]Q - Y_r, \\ & \Phi_{4,4} = -2M_m, \\ & \Phi_{5,4} = KD_{uq}M_m - KD_{u\eta}X_m, \\ & \Phi_{5,5} = -2M_r - 2KD_{u\eta}X_r, \end{aligned} \tag{3.26}$$

and $Y_m = H_m Q$ *and* $Y_r = H_r Q$, *results in the guaranteed* $\mathscr{L}_2$ *gain* γ *from* w *to* z.

Then, the trajectories of the closed-loop system (2.13), starting from the initial con-

ditions $x(0) = 0$*, and using anti-windup gains*

$$\Lambda_m = X_m M_m^{-1}, \quad \Lambda_r = X_r M_r^{-1}. \tag{3.27}$$

satisfy

$$x(t) \in \mathscr{E}(Q^{-1}, s^2) = \{x : x^\top Q^{-1} x < s^2\}, \quad t \geq 0. \tag{3.28}$$

Proof. Satisfaction of (3.25) implies that the set (3.28) is included in the polyhedral set (3.15) ([6])

$$\mathscr{E}(Q^{-1}, s^2) \subset S. \tag{3.29}$$

Consider a quadratic Lyapunov function $V = x^\top Q^{-1} x$ with $Q > 0$. Following standard techniques, inequality (3.24), having its third row and column removed, is equivalent to

$$\frac{d}{dt}(x^\top Q^{-1} x) - w^\top w - 2q_m^\top W_m(q_m - \delta + H_m x) - 2q_r^\top W_r(q_r - \eta + H_r x) < 0. \tag{3.30}$$

Trajectory $x(t)$ starts from zero, thus within $\mathscr{E}(Q^{-1}, s^2)$. As long as it is within $\mathscr{E}(Q^{-1}, s^2)$, it is also in S (strictly) thus, the inequalities in *Lemma.* 3.4.1 hold, i.e.,

$$q_r^\top W_r(q_r - \eta + H_r x) \leq 0, \quad q_m^\top W_m(q_m - \delta + H_m x) \leq 0, \tag{3.31}$$

and therefore, (3.30) reduces to

$$\frac{d}{dt}(x^\top Q^{-1}x) - w^\top w = \dot{V} - w^\top w < 0. \tag{3.32}$$

As proved in Corollary. 3.4.1, starting from $x(0) = 0$ and considering continuity of $x(t)$, as long as (3.32) is satisfied, the trajectories will remain in the set $\mathscr{E}(Q^{-1}, s^2)$ and thus, (3.28) holds.

Regarding the performance, the inequality (3.24) is equivalent to

$$\begin{aligned}&\frac{d}{dt}(x^\top Q^{-1}x) + \gamma^{-2} z^\top z - w^\top w - 2q_m^\top W_m(q_m - \delta + H_m x) \\ &- 2q_r^\top W_r(q_r - \eta + H_r x) < 0.\end{aligned} \tag{3.33}$$

Having the sector conditions (3.31), (3.33) reduces to

$$\frac{d}{dt}(x^\top Q^{-1}x) + z^\top z - w^\top w < 0. \tag{3.34}$$

which after integrating both sides leads to $||z||_2^2 \leq \gamma^2 ||w||_2^2$. □

The key part of the general approach to AW we are using is to replace the nonlinear $sat(u)$ term with variables q_m and q_r. The connections between u and q are sector conditions introduced in *Lemma* 3.4.1. For rate saturation, *Lemma* 3.4.1 allows us using slack/auxiliary variables to improve the results.

Multi-Stage AW Design

Here the concept of multi-stage AW, from [33], is applied to the rate bound saturation element. However, it can easily be applied to the magnitude, or rate and magnitude saturations along similar lines. For anti-windup design, we start by a somewhat standard approach, where the error between the input and output of saturation elements are used to generate anti-windup compensation. For simplicity, we use static gains as shown by Fig. 3.3. We aim to develop an approach that has more aggressive anti-windup gains for the cases where the rate saturation levels are modest. To meet this goal, an artificial saturation block is added to the rate saturation element with bounds larger than the actual saturation limits (Fig. 3.3). The new block is responsible for bounding the sector nonlinearity of the actual rate saturation block.

The static anti-windup blocks containing matrix gains

$$\begin{aligned} \mathrm{AW}_{\mathsf{m}}(q_m) &= -\Lambda_m q_m, \\ \mathrm{AW}_{\mathsf{r}}(q_r) &= -\Lambda_r q_r, \\ \mathrm{AW}_{\tilde{\mathsf{r}}}(\tilde{q}_r) &= -\tilde{\Lambda}_r \tilde{q}_r, \end{aligned} \tag{3.35}$$

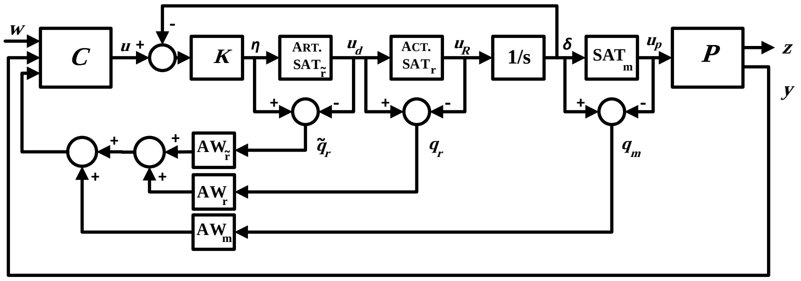

Figure 3.3: Multi-stage anti-windup for system with magnitude and rate saturation.

are applied to the dead-zone functions

$$\begin{aligned} q_m &= \mathrm{dz}(\delta) = \delta - \mathrm{sat_m}(\delta) = \delta - u_p. \qquad (3.36) \\ q_r &= \mathrm{dz}(u_d) = u_d - \mathrm{sat_r}(u_d) = u_d - u_R, \\ \tilde{q}_r &= \mathrm{dz}(\eta) = \eta - \mathrm{sat}_{\tilde{\mathrm{r}}}(\eta) = \eta - u_d. \end{aligned}$$

According to Fig. 3.3, $u_d = \eta - \tilde{q}_r$, $u_R = u_d - q_r$, and $\eta = K(u - \delta)$, therefore, $u_R = K(u - \delta) - \tilde{q}_r - q_r$. Noting that $\delta = \frac{1}{s} u_R$, the signal δ is defined as a new state variable with dynamics

$$\dot{\delta} = u_R = K(u - \delta) - \tilde{q}_r - q_r, \qquad (3.37)$$

in which the signal u can be substituted from (3.6). It is straight forward to build the augmented system with state vector $x = [x_p^\top \quad x_c^\top \quad \delta^\top]^\top \in \mathbb{R}^n$ and w, q_m, q_r, and $\tilde{q}_r$ as input signals. The closed-loop system with magnitude and rate saturation anti-windup gains can be written as

$$\begin{aligned}
\dot{x} &= Ax + B_w w + (B_{q_m} - B_\eta \Lambda_m) q_m + (B_{q_r} - B_\eta \Lambda_r) q_r \\
&\quad + (B_{q_r} - B_\eta \tilde{\Lambda}_r) \tilde{q}_r, \\
z &= C_z x + D_{zw} w + D_{zq} q_m, \\
u &= C_u x + D_{uw} w + (D_{uq} - D_{u\eta} \Lambda_m) q_m - D_{u\eta} \Lambda_r q_r \\
&\quad - D_{u\eta} \tilde{\Lambda}_r \tilde{q}_r,
\end{aligned} \tag{3.38}$$

where

$$\left[\begin{array}{c} A \\ \hline C_z \\ \hline C_u \end{array}\right] = \left[\begin{array}{ccc} A_p & 0 & B_2 \\ B_{cy} C_2 & A_c & B_{cy} D_{22} \\ K D_{cy} C_2 & K C_c & K(D_{cy} D_{22} - I) \\ \hline C_1 & 0 & D_{12} \\ \hline D_{cy} C_2 & C_c & D_{cy} D_{22} \end{array}\right], \tag{3.39}$$

$$\left[\begin{array}{c} B_w \\ \hline D_{zw} \\ \hline D_{uw} \end{array}\right] = \left[\begin{array}{c} B_1 \\ B_{cy} D_{21} + B_{cw} \\ K(D_{cy} D_{21} + D_{cw}) \\ \hline D_{11} \\ \hline D_{cy} D_{21} + D_{cw} \end{array}\right],$$

$$\left[\begin{array}{c|c|c} B_{q_m} & B_\eta & B_{q_r} \\ \hline D_{zq} & D_{uq} & D_{u\eta} \end{array}\right] = \left[\begin{array}{c|c|c} -B_2 & 0 & 0 \\ -B_{cy} D_{22} & [I \quad 0] & 0 \\ -K D_{cy} D_{22} & K[0 \quad I] & -I \\ \hline -D_{12} & -D_{cy} D_{22} & [0 \quad I] \end{array}\right].$$

The nominal closed loop system matrix A is Hurwitz, based on *Assumption 1*.

The artificial saturation block added for the rate aims at bounding the sector nonlinearity associated with the actual saturation block such that the corresponding deadzone q_r belongs to a smaller sector than $[0 \quad I]$. A larger limit of $\tilde{\mathsf{r}} = \frac{\mathsf{r}}{1-s_d}$, with $0 < s_d < 1$, is selected for the artificial element which guarantees $|u_d| < \frac{\mathsf{r}}{1-s_d}$. By setting $s_d = 0$, the second saturation element will never be activated, while by setting it close to 1, the sector condition $q_r \in [0 \quad I]$ of the single-stage design will be recovered. Therefore, by using $0 < s_d < 1$ the size of the rate deadzone sector is shrunk and consequently, more aggressive anti-windup gains may be triggered by q_r. The main idea is to have different anti-windup gains for when the rate command is high (triggered by $\tilde{q}_r$), than when it is modest ($\tilde{q}_r = 0$ but $q_r \neq 0$) which would result in more aggressive anti-windup gains.

The following Lemma, similar to [12], helps identify the key properties of slack variables (denoted by H with different subscripts).

Lemma 3.4.2 (Multi-stage AW sector conditions) *Consider the polyhedral set* $\bar{S}$ *defined as*

$$\bar{S} = \{x \in \mathbb{R}^n : |H_{m(j)}x| \leq \mathsf{m}_i, |\tilde{H}_{r(i)}x| \leq \tilde{\mathsf{r}}_i\}, \qquad (3.40)$$

$$i = 1, \ldots, n_u,$$

where matrices H_m *and* $\tilde{H}_r$ *are free parameters to be determined. Given the sector* *conditions*

$$\delta \longmapsto q_m \in [0 \quad I]_{W_m}, \quad u_d \longmapsto q_r \in [0 \quad s_d I]_{W_r}, \tag{3.41}$$
$$\eta \longmapsto \tilde{q}_r \in [0 \quad I]_{\tilde{W}_r},$$

for $x \in S$ as defined in (3.40)*, the following inequalities hold*

$$\begin{aligned} &(a) \quad q_m^\top W_m(q_m - \delta + H_m x) \le 0, \\ &(b) \quad q_r^\top W_r(q_r - s_d u_d) \le 0, \\ &(c) \quad \tilde{q}_r^\top \tilde{W}_r(\tilde{q}_r - \eta + \tilde{H}_r x) \le 0, \end{aligned} \tag{3.42}$$

with any diagonal positive definite matrices $\tilde{W}_r$, W_r and W_m.

Proof. For simplicity, the proof here is shown for the scalar case. However, the extension to the vector case is straightforward, since the saturation operator defined in (3.1) is decentralized and the weighting matrices W_r and W_m are diagonal and positive definite.

(a)

- if $|\delta| \le \mathsf{m} \Rightarrow q_m = 0 \Rightarrow q_m W_m(q_m - \delta + H_m x) \le 0$,
- if $\delta > \mathsf{m} \Rightarrow q_m = \delta - \mathsf{m} > 0$, and since $x \in \bar{S} \Rightarrow H_m x \le \mathsf{m}$, thus, $q_m - \delta + H_m x \le 0$. Having $q_m > 0$ and $W_m > 0$, we have

  $q_m W_m(q_m - \delta + H_m x) \le 0$,

- if $\delta < -\mathsf{m} \Rightarrow q_m = \delta + \mathsf{m} < 0$, and since $x \in \bar{S} \Rightarrow H_m x \geq -\mathsf{m}$, thus, $q_m - \delta + H_m x \geq 0$. Having $q_m < 0$ and $W_m > 0$, we have

  $q_m W_m (q_m - \delta + H_m x) \leq 0.$

(b)

- if $|u_d| \leq \mathsf{r} \Rightarrow q_r = 0 \Rightarrow q_r W_r (q_r - s_d u_d) \leq 0,$

- if $u_d > \mathsf{r} \Rightarrow q_r = u_d - \mathsf{r} > 0$ and since $|u_d| < \frac{\mathsf{r}}{1-s_d}$, we have, $q_r = u_d - \mathsf{r} < s_d u_d$. Since $q_r > 0$ and $W_r > 0$,

  $q_r W_r (q_r - s_d u_d) \leq 0,$

- if $u_d < -\mathsf{r} \Rightarrow q_r = u_d + \mathsf{r} < 0$ and since $|u_d| < \frac{\mathsf{r}}{1-s_d}$, we have, $q_r = u_d + \mathsf{r} > s_d u_d$. Since $q_r < 0$ and $W_r > 0$,

  $q_r W_r (q_r - s_d u_d) \leq 0.$

(c)

- if $|\eta| \leq \tilde{u}_r \Rightarrow \tilde{q}_r = 0 \Rightarrow \tilde{q}_r^\top (\tilde{q}_r - \eta + \tilde{H}_r x) \leq 0,$

- if $\eta > \tilde{u}_r \Rightarrow \tilde{q}_r = \eta - \tilde{u}_r > 0$, and since $x \in \bar{S} \Rightarrow \tilde{H}_r x \leq \tilde{u}_r$, thus, $\tilde{q}_r - \eta + \tilde{H}_r x \leq 0$. Having $\tilde{q}_r > 0$,

  $\tilde{q}_r^\top (\tilde{q}_r - \eta + \tilde{H}_r x) \leq 0,$

- if $\eta < -\tilde{u}_r \Rightarrow \tilde{q}_r = \eta + \tilde{u}_r < 0$, and since $x \in \bar{S} \Rightarrow \tilde{H}_r x \geq -\tilde{u}_r$, thus, $\tilde{q}_r - \eta + \tilde{H}_r x \geq 0$. Having $\tilde{q}_r < 0$,

  $\tilde{q}_r^\top (\tilde{q}_r - \eta + \tilde{H}_r x) \leq 0.$ □

Note that H_m and $\tilde{H}_r$ are associated with the magnitude and the artificial rate saturation elements, respectively, but, there is no slack variable for the original rate saturation block. The reason is that the $0 < s_d < 1$ plays the same role in the corresponding sector condition, thus, adding a new slack variable will not influence the result.

Next, we present the main result of this section that establishes the convex problem that will result in the anti-windup gains used in Fig. 3.3, along with their properties.

Theorem 3.4.2 (Multi-stage AW standard design: Energy-to-peak case) *Consider the plant and the controller introduced in* (3.5)*,* (3.6)*, and* (3.8)*, as well as the magnitude and rate limits* m *and* r*. Given any solution to the LMI problem*

$$\min_{Q,M_m,M_r,\tilde{M}_r,X_m,X_r,\tilde{X}_r,Y_m,\tilde{Y}_r,\gamma^2} \gamma^2 \tag{3.43}$$

subject to

$$\begin{pmatrix} QA^\top + AQ & * & * & * & * & * \\ B_w^\top & -I & * & * & * & * \\ C_zQ & D_{zw} & -\gamma^2 I & * & * & * \\ \Phi_{4,1} & 0 & M_m D_{zq}^\top & -2M_m & * & * \\ \Phi_{5,1} & KD_{uw} & 0 & \Phi_{5,4} & \Phi_{5,5} & * \\ \Phi_{6,1} & KD_{uw} & 0 & \Phi_{6,4} & \Phi_{6,5} & \Phi_{6,6} \end{pmatrix} < 0, \tag{3.44}$$

$$\begin{pmatrix} \mathsf{m}_i^2/s^2 & Y_{mi} \\ Y_{mi}^\top & Q \end{pmatrix} > 0, \quad \begin{pmatrix} \tilde{\mathsf{r}}_i^2/s^2 & \tilde{Y}_{ri} \\ \tilde{Y}_{ri}^\top & Q \end{pmatrix} > 0, \quad Q > 0, \tag{3.45}$$

where $i = 1, ..., n_u$,

$$\tilde{\mathsf{r}} = \frac{\mathsf{r}}{1 - s_d}, \tag{3.46}$$

and

$$\begin{aligned} M_m &= W_m^{-1}, \quad M_r = (W_r s_d)^{-1}, \quad \tilde{M}_r = \tilde{W}_r^{-1}, \\ X_m &= \Lambda_m M_m, \quad X_r = \Lambda_r M_r, \quad \tilde{X}_r = \tilde{\Lambda}_r \tilde{M}_r, \\ \Phi_{4,1} &= M_m B_{q_m}^\top - X_m^\top B_\eta^\top + [0 \quad 0 \quad I]Q - Y_m, \\ \Phi_{5,1} &= M_r B_{q_r}^\top - X_r^\top B_\eta^\top + [C_u - [0 \quad 0 \quad I]]KQ, \\ \Phi_{6,1} &= \tilde{M}_r B_{q_r}^\top - \tilde{X}_r^\top B_\eta^\top + [C_u - [0 \quad 0 \quad I]]KQ - \tilde{Y}_r, \\ \Phi_{5,4} &= KD_{uq}M_m - KD_{u\eta}X_m, \\ \Phi_{5,5} &= -2M_r s_d^{-1} - KD_{u\eta}X_r - KX_r^\top D_{u\eta}^\top, \\ \Phi_{6,4} &= KD_{uq}M_m - KD_{u\eta}X_m, \\ \Phi_{6,5} &= -\tilde{M}_r - KD_{u\eta}X_r - K\tilde{X}_r^\top D_{u\eta}^\top, \\ \Phi_{6,6} &= -2\tilde{M}_r - KD_{u\eta}\tilde{X}_r - K\tilde{X}_r^\top D_{u\eta}^\top, \end{aligned} \tag{3.47}$$

with $Y_m = H_m Q$ and $\tilde{Y}_r = \tilde{H}_r Q$, we use the following for the anti-windup gains

$$\Lambda_m = X_m M_m^{-1}, \quad \Lambda_r = X_r M_r^{-1}, \quad \tilde{\Lambda}_r = \tilde{X}_r \tilde{M}_r^{-1}. \tag{3.48}$$

Then, for disturbance signals satisfying $\|w\|_2 \leq s$, with $x(0) = 0$, the augmented closed loop system (2.27), has a guaranteed $\mathscr{L}_2$ gain of γ from w to z with the following reachable set

$$\mathscr{E}(Q^{-1}, s^2) = \{x : x^\top Q^{-1} x < s^2\}. \tag{3.49}$$

Proof. Following the sketch of the proof of *Theorem.* 3.4.1, satisfaction of (3.45) implies that the set (3.49) is included in the polyhedral set (3.40)

$$\mathscr{E}(Q^{-1}, s^2) \subset \bar{S}. \tag{3.50}$$

Inequality (3.44), having its third row and column removed, is equivalent to

$$\begin{aligned} &\frac{d}{dt}(x^\top Q^{-1} x) - w^\top w - 2q_m^\top W_m(q_m - \delta + H_m x) \\ &- 2q_r^\top W_r(q_r - s_d u_d) - 2\tilde{q}_r^\top \tilde{W}_r(\tilde{q}_r - \eta + \tilde{H}_r x) < 0. \end{aligned} \tag{3.51}$$

Given (3.50) and invoking *Lemma.* 3.4.2

$$\begin{aligned} q_m^\top W_m(q_m - \delta + H_m x) &\leq 0, \\ q_r^\top W_r(q_r - s_d u_d) &\leq 0, \\ \tilde{q}_r^\top \tilde{W}_r(\tilde{q}_r - \eta + \tilde{H}_r x) &\leq 0, \end{aligned} \tag{3.52}$$

and thus (3.51) reduces to

$$\frac{d}{dt}(x^\top Q^{-1}x) - w^\top w = \dot{V} - w^\top w < 0. \tag{3.53}$$

As proved in Corollary. 3.4.1, starting from $x(0) = 0$, as long as (3.53) is satisfied, the trajectories will remain in the set $\mathscr{E}(Q^{-1}, s^2)$ (3.49).

Regarding the performance, the inequality (3.44) is equivalent to

$$\begin{aligned} &\frac{d}{dt}(x^\top Q^{-1}x) + \gamma^{-2}z^\top z - w^\top w - 2q_m^\top W_m(q_m - \delta + H_m x) \\ &- 2q_r^\top W_r(q_r - s_d u_d) - 2\tilde{q}_r^\top \tilde{W}_r(\tilde{q}_r - \eta + \tilde{H}_r x) < 0. \end{aligned} \tag{3.54}$$

Having the sector conditions (3.52), (3.54) reduces to

$$\frac{d}{dt}(x^\top Q^{-1}x) + z^\top z - w^\top w < 0. \tag{3.55}$$

which after integrating both sides guarantees the $\mathscr{L}_2$ gain γ from w to z, $||z||_2^2 \leq \gamma^2 ||w||_2^2$. □

As discussed earlier, the two rate saturation blocks act on different levels of saturation. This gives the opportunity to use the signal based on q_r for high performance, and use the signal from the artificial saturation element $\tilde{q}_r$ for ensuring stability (and some performance) for all levels of saturation. The LMI (3.44) establishes the stability and performance when both saturation elements are present (saturated or not). To obtain high performance anti-windup gains, we consider the case in which the artificial element is not active and thus, does not exist, although it provides a bound for the signal that enters the second element. The resulting problem will be similar to the one stated in *Theorem 4.1*, except for the sixth row and column of (3.44) removed. Such a problem can give higher performance (lower γ) since the sector condition for the key nonlinear element is now made smaller. Of course, such a results is based on the assumption that, somehow, the magnitude of η is smaller than $\tilde{r}$, which cannot be guaranteed without the artificial saturation box (i.e., *Theorem 3.4.1*).

To ensure loop stability and aggressive anti-windup gains for moderate saturation levels, we solve both problems at the same time. By solving the two problems simultaneously, we can establish high gains for the moderate levels of saturation, and stability of the closed-loop for all levels. The results are summarized below.

Theorem 3.4.3 (Multi-stage AW-aggressive standard design: Energy-to-peak analysis) *Consider the the plant and the controller introduced in* (3.5), (3.6), *and* (3.8), *as well as the magnitude and rate limits* m *and* r. *Given any solution to the LMI problem*

$$\min_{Q,\bar{Q},M_m,M_r,\tilde{M}_r,X_m,X_r,\tilde{X}_r,Y_m,\tilde{Y}_r,\bar{Y}_m,\gamma^2,\bar{\gamma}^2} \quad c_1\gamma^2 + c_2\bar{\gamma}^2 \tag{3.56}$$

subject to

$$\begin{pmatrix} QA^\top + AQ & * & * & * & * & * \\ B_w^\top & -I & * & * & * & * \\ C_zQ & D_{zw} & -\gamma^2 I & * & * & * \\ \Phi_{4,1} & 0 & M_mD_{zq}^\top & -2M_m & * & * \\ \Phi_{5,1} & KD_{uw} & 0 & \Phi_{5,4} & \Phi_{5,5} & * \\ \Phi_{6,1} & KD_{uw} & 0 & \Phi_{6,4} & \Phi_{6,5} & \Phi_{6,6} \end{pmatrix} < 0, \tag{3.57}$$

$$\begin{pmatrix} \mathsf{m}_i^2/s^2 & Y_{mi} \\ Y_{mi}^\top & Q \end{pmatrix} > 0, \quad \begin{pmatrix} \tilde{\mathsf{r}}_i^2/s^2 & \tilde{Y}_{ri} \\ \tilde{Y}_{ri}^\top & Q \end{pmatrix} > 0, \quad Q > 0, \tag{3.58}$$

$$\begin{pmatrix} \bar{Q}A^\top + A\bar{Q} & * & * & * & * \\ B_w^\top & -I & * & * & * \\ C_z\bar{Q} & D_{zw} & -\bar{\gamma}^2 I & * & * \\ \bar{\Phi}_{4,1} & 0 & M_mD_{zq}^\top & -2M_m & * \\ \bar{\Phi}_{5,1} & KD_{uw} & 0 & \Phi_{5,4} & \Phi_{5,5} \end{pmatrix} < 0, \tag{3.59}$$

$$\begin{pmatrix} \mathsf{m}_i^2/s^2 & \bar{Y}_{mi} \\ \bar{Y}_{mi}^\top & \bar{Q} \end{pmatrix} > 0, \tag{3.60}$$

in which (3.57) *and* (3.58) *are identical to* (3.44) *and* (3.45)*, respectively. Moreover,*

$\bar{Y}_m = H_m\bar{Q}$ *and*

$$\bar{\Phi}_{4,1} = M_m B_{q_m}^\top - X_m^\top B_\eta^\top + [0 \quad 0 \quad I]\bar{Q} - \bar{Y}_m, \tag{3.61}$$
$$\bar{\Phi}_{5,1} = M_r B_{q_r}^\top - X_r^\top B_\eta^\top + [C_u - [0 \quad 0 \quad I]]K\bar{Q},$$

use (3.48) to obtain the anti-windup gains. The augmented closed-loop system (2.27) has the same reachable set as (3.49) and the $\mathscr{L}_2$ *gain* γ *from* w *to* z*, as long as the disturbance signals satisfy* $\|w\|_2 \leq s$ *and* $x(0) = 0$*. Moreover, for moderate levels of saturation specified as* $|\eta| \leq \tilde{\mathrm{r}} = \frac{\mathrm{r}}{1-s_d}$*,* $\bar{\gamma}$ *is the upper bound for the* $\mathscr{L}_2$ *gain.*

Proof. The first argument of the theorem is proven in *Theorem 3.4.2* (since (3.44) holds with the resulting gains). Using the Lyapunov function $V = x^\top \bar{Q}^{-1} x$ and following the same sketch of the proof of *Theorem 3.4.2*, the inequality (3.59) is equivalent to

$$\frac{d}{dt}(x^\top \bar{Q}^{-1} x) + \bar{\gamma}^{-2} z^\top z - w^\top w - 2q_m^\top W_m(q_m - \delta + H_m x) \tag{3.62}$$
$$-2q_r^\top W_r(q_r - s_d u_d) < 0.$$

For moderate levels of saturation specified as $|\eta| < \tilde{\mathrm{r}} = \frac{\mathrm{r}}{1-s_d}$, only the magnitude and the actual rate saturation elements are active and the sector conditions $\delta \longmapsto q_m \in [0 \quad I]_{W_m}$ and $u_d \longmapsto q_r \in [0 \quad s_d I]_{W_r}$ are in effect. Therefore, according to *Lemma 3.4.2*, the inequalities $q_m^\top W_m(q_m - \delta + H_m x) \leq 0$ and $q_r^\top W_r(q_r - s_d u_d) \leq 0$

will be satisfied. Hence, (3.62) leads to

$$\frac{d}{dt}(x^\top \bar{Q}^{-1} x) + \bar{\gamma}^{-2} z^\top z - w^\top w < 0, \tag{3.63}$$

which establishes $\bar{\gamma}$ as the performance measure, if the artificial saturation element avoids activation. By using larger values for c_2, more aggressive AW gains for moderate saturation levels can be achieved which results in a lower $\bar{\gamma}$ and thus, a better performance. However, this is at the cost of a larger γ, as the guaranteed $\mathscr{L}_2$ gain of the closed-loop system under general conditions. □

Remark 3.4.1 *Unique anti-windup gains Λ_m, Λ_r, and $\tilde{\Lambda}_r$ are guaranteed as long as the same matrices M_m, M_r, X_m, X_r, and $\tilde{X}_r$ are used in* (3.44) *and* (3.59)*. However, a different symmetric matrix $\bar{Q}$ in the Lyapunov function is allowed, in order to have an extra degree of freedom for solving the optimization problem.*

As a result, we now have three gains, one of which (i.e., $\tilde{\Lambda}_r$) will be used to guarantee stability and some performance only when the rate is significantly above the bound.

3.5 New MRAW Design

Consider the block diagram in Fig. 3.4. The model is the standard setup for magnitude and rate AW used in e.g. [50], except for the signal Γ, the first n_u elements of the magnitude and rate feedback signals, added to the controller output. Signal Γ directly affects the rate dynamics of the system and improves the performance.

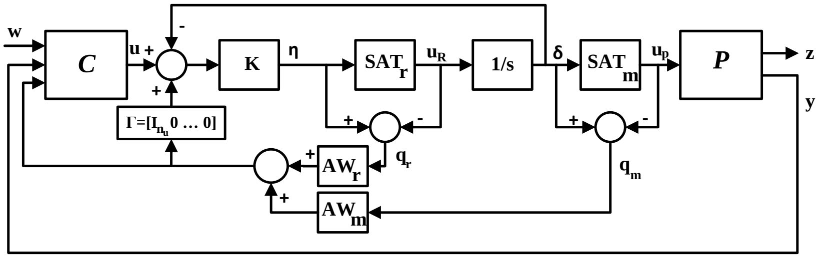

Figure 3.4: New static anti-windup design for system with magnitude and rate saturation.

Our objective is to obtain suitable additive modification signals $v_1 \in \mathbb{R}^{n_c}$ and $v_2 \in \mathbb{R}^{n_u}$ to the unconstrained controller (3.71), i.e.,

$$\begin{aligned} \dot{x}_c &= A_c x_c + B_{cy} y + B_{cw} w + v_1, \\ u &= C_c x_c + D_{cy} y + D_{cw} w + v_2, \end{aligned} \tag{3.64}$$

such that the closed-loop system is internally stable with a guaranteed input-output performance level.

3.5.1 Single-Stage AW Design

Our proposed AW augmentation is shown in Fig. 3.4, where static anti-windup blocks are

$$\mathrm{AW_R}(q_r) = -\Lambda_r q_r, \quad \mathrm{AW_M}(q_m) = -\Lambda_m q_m, \tag{3.65}$$

with

$$
\begin{aligned}
q_r &= \mathrm{dz}(\eta) = \eta - \mathrm{sat}_{\mathrm{R}}(\eta) = \eta - u_R, \\
q_m &= \mathrm{dz}(\delta) = \delta - \mathrm{sat}_{\mathrm{M}}(\delta) = \delta - u_p.
\end{aligned}
\tag{3.66}
$$

and $u_R = \eta - q_r$. Here, we also have

$$
\begin{aligned}
\eta &= K(u - \delta + \Gamma), \\
\Gamma &= [I_{n_u} \quad 0_{n_u \times n_c}](\Lambda_m q_m + \Lambda_r q_r).
\end{aligned}
\tag{3.67}
$$

Therefore, $u_R = K(u - \delta + \Gamma) - q_r$. Since $\delta = \frac{1}{s} u_R$, the signal δ is a new state variable with dynamics

$$
\dot{\delta} = K(u - \delta + \Gamma) - q_r, \tag{3.68}
$$

in which the signal u can be substituted from (3.71). According to (3.68), Γ enters the dynamics of the integrator directly. Moreover, v_1 and v_2 satisfy $v = AW_R(q_r) + AW_M(q_m)$ with $v = [v_1^\top \quad v_2^\top]^\top$.

Compared to the system matrices of the standard MRAW, only the B_η matrix has changed, having the gain K appearing in the last row block. As shown in the numerical examples in *Section* 3.6, this change improves the performance of the MRAW design significantly.

Energy Bounded Disturbance

The aim of the MRAW design is a method that also applies to input rate saturation. Such results will necessarily be local. Here, we assume that a possibly conservative estimate of the disturbance signal $w(t)$ is known.

Assumption 3 (Magnitude bound on exogenous input) The exogenous input entering the system satisfies $\|w\|_2 < s$ for some known $s \in \mathbb{R}_{>0}$. $\square$

For zero initial conditions and a fixed input size $s \in \mathbb{R}_{>0}$, an anti-windup compensator must be designed such that the control output z of the modified control system satisfies

$$\|z\|_2 \leq \gamma \|w\|_2, \qquad \forall w \quad \text{such that} \quad \|w\|_2 \leq s. \tag{3.69}$$

Stability and acceptable performance are then guaranteed for disturbances satisfying this bound.

The linear plant P is given by

$$\begin{aligned} \dot{x}_p &= A_p x_p + B_1 w + B_2 u_p, \\ z &= C_1 x_p + D_{11} w + D_{12} u_p, \\ y &= C_2 x_p + D_{21} w + D_{22} u_p, \end{aligned} \tag{3.70}$$

and the compensator C as

$$\begin{aligned} \dot{x}_c &= A_c x_c + B_{cy} y + B_{cw} w, \\ u &= C_c x_c + D_{cy} y + D_{cw} w. \end{aligned} \tag{3.71}$$

The closed loop system is given by

$$\begin{aligned} \dot{x} &= A x + B_w w + (B_{q_m} - B_\eta \Lambda_m) q_m + (B_{q_r} - B_\eta \Lambda_r) q_r, \\ z &= C_z x + D_{zw} w + D_{zq} q_m, \\ u &= C_u x + D_{uw} w + (D_{uq} - D_{u\eta} \Lambda_m) q_m - D_{u\eta} \Lambda_r q_r, \end{aligned} \tag{3.72}$$

with system matrices given by

$$\left[\begin{array}{c} A \\ \hline C_z \\ \hline C_u \end{array}\right] = \left[\begin{array}{ccc} A_p & 0 & B_2 \\ B_{cy} C_2 & A_c & B_{cy} D_{22} \\ K D_{cy} C_2 & K C_c & K(D_{cy} D_{22} - I) \\ \hline C_1 & 0 & D_{12} \\ \hline D_{cy} C_2 & C_c & D_{cy} D_{22} \end{array}\right], \tag{3.73}$$

$$\left[\begin{array}{c} B_w \\ \hline D_{zw} \\ \hline D_{uw} \end{array}\right] = \left[\begin{array}{c} B_1 \\ B_{cy}D_{21} + B_{cw} \\ K(D_{cy}D_{21} + D_{cw}) \\ \hline D_{11} \\ \hline D_{cy}D_{21} + D_{cw} \end{array}\right], \tag{3.74}$$

$$\left[\begin{array}{c|c|c} B_{q_m} & B_{\eta} & B_{q_r} \\ \hline D_{zq} & D_{uq} & D_{u\eta} \end{array}\right] = \left[\begin{array}{c|cc|c} -B_2 & 0 & 0 & 0 \\ -B_{cy}D_{22} & I & 0 & 0 \\ -KD_{cy}D_{22} & \mathbf{K}[\mathbf{1}\quad \mathbf{0}] & K & -I \\ \hline -D_{12} & \multicolumn{2}{c|}{-D_{cy}D_{22}} & [0\quad I] \end{array}\right].$$

Compared to the system matrices of the standard MRAW (3.14), only the B_{η} matrix has changed, having the gain K showing up in more places. According to the numerical examples, this change has improved the performance of the MRAW design significantly.

Theorem 3.5.1 (Single-stage AW new design: Energy-to-peak analysis) *Consider the disturbance signal satisfying* $\|w\|_2 \leq s$*, with* $x(0) = 0$*, and the plant and the controller introduced in* (3.5) *and* (3.6) *with the magnitude and rate limits* m *and* r*. Any solution to the LMI optimization problem*

$$\min_{Q,M_m,M_r,X_m,X_r,Y_m,Y_r,\gamma^2} \quad \gamma^2 \tag{3.75}$$

subject to

$$\begin{pmatrix} QA^\top + AQ & * & * & * & * \\ B_w^\top & -I & * & * & * \\ C_z Q & D_{zw} & -\gamma^2 I & * & * \\ \Phi_{4,1} & 0 & M_m D_{zq}^\top & \Phi_{4,4} & * \\ \Phi_{5,1} & KD_{uw} & 0 & \Phi_{5,4} & \Phi_{5,5} \end{pmatrix} < 0, \tag{3.76}$$

$$\begin{pmatrix} \mathsf{m}_i^2/s^2 & Y_{mi} \\ Y_{mi}^\top & Q \end{pmatrix} > 0, \quad \begin{pmatrix} \mathsf{r}_i^2/s^2 & Y_{ri} \\ Y_{ri}^\top & Q \end{pmatrix} > 0, \quad Q > 0, \tag{3.77}$$

where $i = 1, ..., n_u$, *and*

$$\begin{aligned} & M_m = W_m^{-1}, M_r = W_r^{-1}, X_m = \Lambda_m M_m, X_r = \Lambda_r M_r, && (3.78) \\ & \Phi_{4,1} = M_m B_{q_m}^\top - X_m^\top B_\eta^\top + [0 \quad 0 \quad I]Q - Y_m, \\ & \Phi_{5,1} = M_r B_{q_r}^\top - X_r^\top B_\eta^\top + [KC_u - [0 \quad 0 \quad K]]Q - Y_r, \\ & \Phi_{4,4} = -2M_m, \\ & \Phi_{5,4} = KD_{uq} M_m - KD_{u\eta} X_m + [K \quad 0] X_m, \\ & \Phi_{5,5} = -2M_r - 2KD_{u\eta} X_r + [K \quad 0] X_r + X_r^\top [K \quad 0]^\top, \end{aligned}$$

and $Y_m = H_m Q$ *and* $Y_r = H_r Q$, *results in the guaranteed* $\mathscr{L}_2$ *gain* γ *from* w *to* z, *for the augmented closed loop system (2.55) with anti-windup gains*

$$\Lambda_m = X_m M_m^{-1}, \quad \Lambda_r = X_r M_r^{-1}, \tag{3.79}$$

Proof. Similar to the proof of *Theorem.* 3.4.1. □

3.5.2 Multi-Stage AW Design

The block diagram of the multi-stage anti-windup design using the new structure is shown in Fig. 3.5.

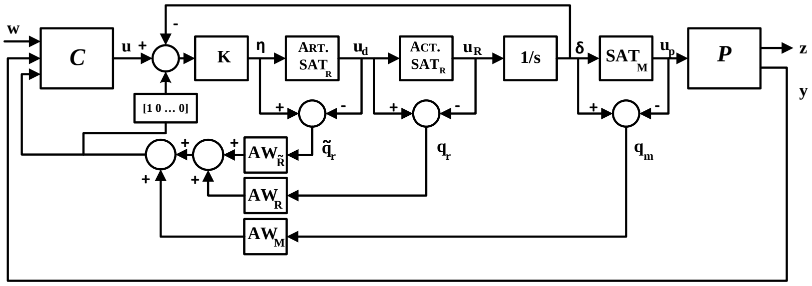

Figure 3.5: Multi-stage anti-windup for system with magnitude and rate saturation.

Theorem 3.5.2 (Multi-stage AW new design: Energy-to-peak analysis) *Consider the plant and the controller introduced in* (3.70)*,* (3.71)*, and* (3.8)*, as well as the magnitude and rate limits* m *and* r*. Given any solution to the LMI problem*

$$\min_{Q,M_m,M_r,\tilde{M}_r,X_m,X_r,\tilde{X}_r,Y_m,\tilde{Y}_r,\gamma^2} \quad \gamma^2 \tag{3.80}$$

subject to

$$\begin{pmatrix} QA^\top + AQ & * & * & * & * & * \\ B_w^\top & -I & * & * & * & * \\ C_zQ & D_{zw} & -\gamma^2 I & * & * & * \\ \Phi_{4,1} & 0 & M_m D_{zq}^\top & -2M_m & * & * \\ \Phi_{5,1} & KD_{uw} & 0 & \Phi_{5,4} & \Phi_{5,5} & * \\ \Phi_{6,1} & KD_{uw} & 0 & \Phi_{6,4} & \Phi_{6,5} & \Phi_{6,6} \end{pmatrix} < 0, \tag{3.81}$$

$$\begin{pmatrix} \mathsf{m}_i^2/s^2 & Y_{mi} \\ Y_{mi}^\top & Q \end{pmatrix} > 0, \quad \begin{pmatrix} \tilde{\mathsf{r}}_i^2/s^2 & \tilde{Y}_{ri} \\ \tilde{Y}_{ri}^\top & Q \end{pmatrix} > 0, \quad Q > 0, \tag{3.82}$$

where $i = 1, ..., n_u$,

$$\tilde{\mathsf{r}} = \frac{\mathsf{r}}{1 - s_d}, \tag{3.83}$$

and

$$
\begin{aligned}
M_m &= W_m^{-1}, \quad M_r = (W_r s_d)^{-1}, \quad \tilde{M}_r = \tilde{W}_r^{-1}, \qquad (3.84)\\
X_m &= \Lambda_m M_m, \quad X_r = \Lambda_r M_r, \quad \tilde{X}_r = \tilde{\Lambda}_r \tilde{M}_r,\\
\Phi_{4,1} &= M_m B_{q_m}^\top - X_m^\top B_\eta^\top + [0 \quad 0 \quad I]Q - Y_m,\\
\Phi_{5,1} &= M_r B_{q_r}^\top - X_r^\top B_\eta^\top + [C_u - [0 \quad 0 \quad I]]KQ,\\
\Phi_{6,1} &= \tilde{M}_r B_{q_r}^\top - \tilde{X}_r^\top B_\eta^\top + [C_u - [0 \quad 0 \quad I]]KQ - \tilde{Y}_r,\\
\Phi_{5,4} &= KD_{uq}M_m - KD_{u\eta}X_m + s_d K[1 \quad 0]X_m,\\
\Phi_{5,5} &= -2M_r s_d^{-1} - KD_{u\eta}X_r - KX_r^\top D_{u\eta}^\top + s_d K[1 \quad 0]X_r + s_d K X_r^\top [1 \quad 0]^\top,\\
\Phi_{6,4} &= KD_{uq}M_m - KD_{u\eta}X_m + K[1 \quad 0]X_m,\\
\Phi_{6,5} &= -\tilde{M}_r - KD_{u\eta}X_r - K\tilde{X}_r^\top D_{u\eta}^\top + K[1 \quad 0]X_r + s_d K\tilde{X}_r^\top [1 \quad 0]^\top,\\
\Phi_{6,6} &= -2\tilde{M}_r - KD_{u\eta}\tilde{X}_r - K\tilde{X}_r^\top D_{u\eta}^\top + K[1 \quad 0]\tilde{X}_r + K\tilde{X}_r^\top [1 \quad 0]^\top,
\end{aligned}
$$

with $Y_m = H_m Q$ and $\tilde{Y}_r = \tilde{H}_r Q$, we use the following for the anti-windup gains

$$\Lambda_m = X_m M_m^{-1}, \quad \Lambda_r = X_r M_r^{-1}, \quad \tilde{\Lambda}_r = \tilde{X}_r \tilde{M}_r^{-1}. \qquad (3.85)$$

Then, for disturbance signals satisfying $\|w\|_2 \leq s$, with $x(0) = 0$, the augmented closed loop system (2.62), has a guaranteed $\mathscr{L}_2$ gain of γ from w to z with the following reachable set

$$\mathscr{E}(Q^{-1}, s) = \{x : x^\top Q^{-1} x < s\}. \qquad (3.86)$$

Proof. Similar to the proof of *Theorem.* 3.4.2. □

Theorem 3.5.3 (Multi-stage AW-aggressive new design: Energy-to-peak analysis) *Consider the the plant and the controller introduced in* (3.70), (3.71)*, and* (3.8)*, as well as the magnitude and rate limits* m *and* r*. Given any solution to the LMI problem*

$$\min_{Q,\bar{Q},M_m,M_r,\tilde{M}_r,X_m,X_r,\tilde{X}_r,Y_m,\tilde{Y}_r,\bar{Y}_m,\gamma^2,\bar{\gamma}^2} \quad c_1\gamma^2 + c_2\bar{\gamma}^2 \tag{3.87}$$

subject to

$$\begin{pmatrix} QA^\top + AQ & * & * & * & * & * \\ B_w^\top & -I & * & * & * & * \\ C_zQ & D_{zw} & -\gamma^2 I & * & * & * \\ \Phi_{4,1} & 0 & M_m D_{zq}^\top & -2M_m & * & * \\ \Phi_{5,1} & KD_{uw} & 0 & \Phi_{5,4} & \Phi_{5,5} & * \\ \Phi_{6,1} & KD_{uw} & 0 & \Phi_{6,4} & \Phi_{6,5} & \Phi_{6,6} \end{pmatrix} < 0, \tag{3.88}$$

$$\begin{pmatrix} \mathsf{m}_i^2/s^2 & Y_{mi} \\ Y_{mi}^\top & Q \end{pmatrix} > 0, \quad \begin{pmatrix} \tilde{\mathsf{r}}_i^2/s^2 & \tilde{Y}_{ri} \\ \tilde{Y}_{ri}^\top & Q \end{pmatrix} > 0, \quad Q > 0, \tag{3.89}$$

$$\begin{pmatrix} \bar{Q}A^\top + A\bar{Q} & * & * & * & * \\ B_w^\top & -I & * & * & * \\ C_z\bar{Q} & D_{zw} & -\bar{\gamma}^2 I & * & * \\ \bar{\Phi}_{4,1} & 0 & M_m D_{zq}^\top & -2M_m & * \\ \bar{\Phi}_{5,1} & KD_{uw} & 0 & \Phi_{5,4} & \Phi_{5,5} \end{pmatrix} < 0, \tag{3.90}$$

$$\begin{pmatrix} \mathsf{m}_i^2/s^2 & \bar{Y}_{mi} \\ \bar{Y}_{mi}^\top & \bar{Q} \end{pmatrix} > 0, \tag{3.91}$$

in which (3.88) *and* (3.89) *are identical to* (3.81) *and* (3.82), *respectively. Moreover,* $\bar{Y}_m = H_m\bar{Q}$ *and*

$$\begin{aligned} \bar{\Phi}_{4,1} &= M_m B_{q_m}^\top - X_m^\top B_\eta^\top + [0 \quad 0 \quad I]\bar{Q} - \bar{Y}_m, \\ \bar{\Phi}_{5,1} &= M_r B_{q_r}^\top - X_r^\top B_\eta^\top + [C_u - [0 \quad 0 \quad I]]K\bar{Q}, \end{aligned} \tag{3.92}$$

use (3.85) to obtain the anti-windup gains. The augmented closed-loop system (2.70) has the same reachable set as (3.86) and the $\mathscr{L}_2$ *gain* γ *from* w *to* z*, as long as the disturbance signals satisfy* $\|w\|_2 \leq s$ *and* $x(0) = 0$*. Moreover, for moderate levels of saturation specified as* $|\eta| \leq \tilde{\mathsf{r}} = \frac{\mathsf{r}}{1-s_d}$, $\bar{\gamma}$ *is the upper bound for the* $\mathscr{L}_2$ *gain.*

Proof. Similar to the proof of Theorem. 3.4.3. □

Peak Bounded Disturbance

In this section the MRAW design is conducted using peak-to-peak analysis with disturbance signals satisfying $w^{\top}w \leq w_{max}$ for some known w_{max}. Energy-to-peak (or $\mathscr{L}_2$ gain) results can be obtained with minor and standard modifications and will not be repeated.

Here, the goal is to find the guaranteed peak of the closed-loop system performance output z while having a peak bounded disturbance signal.

Assumption 4 (No feed-through terms in performance output) For simplicity, the performance output is assumed to depend only on the states and have no feed-through terms, i.e. the matrices D_{11} and D_{12} are assumed to be zero. Thus, $z = C_1 x_p$. □

Remark 3.5.1 Including the u term in the performance output is relatively straightforward but complicates the LMIs, and inclusion of the w term would require a further line search. □

The linear plant P is assumed to be given by

$$\begin{aligned} \dot{x}_p &= A_p x_p + B_1 w + B_2 u_p, \\ z &= C_1 x_p, \\ y &= C_2 x_p + D_{21} w + D_{22} u_p, \end{aligned} \tag{3.93}$$

and the unconstrained controller C is given by (3.71). The closed loop system is thus given by

$$\begin{aligned}
\dot{x} &= Ax + B_w w + (B_{q_m} - B_\eta \Lambda_m) q_m + (B_{q_r} - B_\eta \Lambda_r) q_r, \\
z &= C_z x, \\
u &= C_u x + D_{uw} w + (D_{uq} - D_{u\eta} \Lambda_m) q_m - D_{u\eta} \Lambda_r q_r,
\end{aligned} \tag{3.94}$$

with system matrices given by

$$\left[\begin{array}{c} A \\ \hline C_z \\ \hline C_u \end{array}\right] = \left[\begin{array}{ccc} A_p & 0 & B_2 \\ B_{cy} C_2 & A_c & B_{cy} D_{22} \\ K D_{cy} C_2 & K C_c & K(D_{cy} D_{22} - I) \\ \hline C_1 & 0 & D_{12} \\ \hline D_{cy} C_2 & C_c & D_{cy} D_{22} \end{array}\right], \tag{3.95}$$

$$\left[\begin{array}{c} B_w \\ \hline D_{zw} \\ \hline D_{uw} \end{array}\right] = \left[\begin{array}{c} B_1 \\ B_{cy} D_{21} + B_{cw} \\ K(D_{cy} D_{21} + D_{cw}) \\ \hline D_{11} \\ \hline D_{cy} D_{21} + D_{cw} \end{array}\right],$$

$$\left[\begin{array}{c|c|c} B_{q_m} & B_\eta & B_{q_r} \\ \hline D_{zq} & D_{uq} & D_{u\eta} \end{array}\right] = \left[\begin{array}{c|cc|c} -B_2 & 0 & 0 & 0 \\ -B_{cy} D_{22} & I & 0 & 0 \\ -K D_{cy} D_{22} & K[I \quad 0] & K & -I \\ \hline -D_{12} & \multicolumn{2}{c|}{-D_{cy} D_{22}} & [0 \quad I] \end{array}\right].$$

Assumption 5 (Peak bound on exogenous input) The exogenous input w, for some known $w_{max} \geq 0$, satisfies

$$w^\top(t)w(t) \leq w_{max}^2, \quad \forall t \geq 0. \tag{3.96}$$

For a given $w_{max} \in \mathbb{R}_{>0}$, we wish to minimize

$$z^\top(t)z(t) \leq \chi^2, \ \text{ for } \ w^\top(t)w(t) \leq w_{max}^2, \ \forall t \geq 0. \tag{3.97}$$

where χ is the performance measure.

The following theorem presents the single-stage MRAW design which sets up a convex optimization problem and solves for the AW gains as decision variables.

Theorem 3.5.4 (Single-stage AW new design: Peak-to-peak analysis) *Consider the plant* (3.93) *and its nominal controller* (3.71)*. Assume that this system is exposed to peak-bounded disturbances with known upper bound $w_{max} \in \mathbb{R}$, i.e., $w^\top(t)w(t) \leq w_{max}^2$. Given the bounds m and r on the actuator magnitude and rate, respectively, assume that for a given $0 < \alpha < \frac{|Re(\lambda_{min}(A))|}{2}$, there exists a solution for*

$$\min_{Q,M_m,M_r,X_m,X_r,Y_m,Y_r,\chi^2} \quad \chi^2 \tag{3.98}$$

subject to

$$\begin{pmatrix} QA^\top + AQ + \alpha Q & * & * & * \\ B_w^\top & -\alpha I & * & * \\ \Phi_{3,1} & 0 & -2M_m & * \\ \Phi_{4,1} & KD_{uw} & \Phi_{4,3} & \Phi_{4,4} \end{pmatrix} < 0, \tag{3.99}$$

$$\begin{pmatrix} Q & QC_z^\top \\ C_zQ & \chi^2/w_{max}^2 \end{pmatrix} > 0, \quad \begin{pmatrix} \mathsf{m}_i^2/w_{max}^2 & Y_{mi} \\ Y_{mi}^\top & Q \end{pmatrix} > 0, \tag{3.100}$$

$$\begin{pmatrix} \mathsf{r}_i^2/w_{max}^2 & Y_{ri} \\ Y_{ri}^\top & Q \end{pmatrix} > 0, \tag{3.101}$$

where $i = 1, ..., n_u$, and

$$\begin{aligned} M_m &= W_m^{-1}, M_r = W_r^{-1}, X_m = \Lambda_m M_m, X_r = \Lambda_r M_r, \\ \Phi_{3,1} &= M_m B_{q_m}^\top - X_m^\top B_\eta^\top + [0 \quad 0 \quad I]Q - Y_m, \\ \Phi_{4,1} &= M_r B_{q_r}^\top - X_r^\top B_\eta^\top + [C_u - [0 \quad 0 \quad I]]KQ - Y_r, \\ \Phi_{4,3} &= KD_{uq}M_m - KD_{u\eta}X_m + K[1 \quad 0]X_m, \\ \Phi_{4,4} &= -2M_r - KD_{u\eta}X_r - KX_r^\top D_{u\eta}^\top \\ &\quad + K[1 \quad 0]X_r + KX_r^\top [1 \quad 0]^\top. \end{aligned} \tag{3.102}$$

Then, the trajectories of the closed-loop system (15), starting from the initial con-

ditions $x(0) \in \mathscr{E}(Q^{-1}, w_{max}^2)$*, and using anti-windup gains*

$$\Lambda_m = X_m M_m^{-1}, \quad \Lambda_r = X_r M_r^{-1}, \tag{3.103}$$

for $t \geq 0$ *satisfy*

$$x(t) \in \mathscr{E}(Q^{-1}, w_{max}^2) = \{x : x^\top Q^{-1} x < w_{max}^2\}, \tag{3.104}$$

$$z^\top(t) z(t) \leq \chi^2, \quad t \geq 0. \tag{3.105}$$

Proof 3.5.1 *Satisfaction of* (3.101) *implies that the set* (3.104) *is included in the polyhedral set* (3.15) *([6]),*

$$\mathscr{E}(Q^{-1}, w_{max}^2) \subset S. \tag{3.106}$$

Consider a quadratic Lyapunov function $V = x^\top Q^{-1} x$ *with* $Q > 0$*. Following standard techniques, inequality* (3.99) *is equivalent to*

$$\begin{aligned} &\frac{d}{dt}(x^\top Q^{-1} x) + \alpha x^\top Q^{-1} x - \alpha w^\top w \\ &- 2q_m^\top W_m(q_m - \delta + H_m x) - 2q_r^\top W_r(q_r - \eta + H_r x) < 0. \end{aligned} \tag{3.107}$$

Given (3.106) *and invoking Lemma 3.4.1*

$$q_r^\top W_r(q_r - \eta + H_r x) \leq 0, \quad q_m^\top W_m(q_m - \delta + H_m x) \leq 0,$$

if $x(t) \in \mathscr{E}(Q^{-1}, w_{max}^2)$*. Thus,* (3.107) *reduces to*

$$\dot{V} + \alpha(V - w^\top w) < 0. \tag{3.108}$$

For $x(0) \in \mathscr{E}(Q^{-1}, w_{max}^2)$*, as long as* (3.108) *is satisfied, the trajectories remain in the set* $\mathscr{E}(Q^{-1}, w_{max}^2)$*, and by continuity of* x*,* (3.104) *holds for all* t*.*
For performance, left inequality in (3.100) *can be expressed as* $x^\top Q^{-1} x - \frac{w_{max}}{\delta^2} x^\top C_z^\top C_z x > 0$*, which together with* (3.104) *guarantees (27).* ☐

Remark 3.5.2 *In Theorem 3.5.4,* α *enters the inequality in a product form. For optimized performance, a line search is done, as in other peak-to-peak gain problems. Energy-to-peak approach does not have the line search but give considerably more conservative results.*

Multi-Stage AW Design

The closed loop system is given by

$$\begin{aligned} \dot{x} &= Ax + B_w w + (B_{q_m} - B_\eta \Lambda_m) q_m + (B_{q_r} - B_\eta \Lambda_r) q_r \\ &\quad + (B_{q_r} - B_\eta \tilde{\Lambda}_r) \tilde{q}_r, \\ z &= C_z x, \\ u &= C_u x + D_{uw} w + (D_{uq} - D_{u\eta} \Lambda_m) q_m - D_{u\eta} \Lambda_r q_r \\ &\quad - D_{u\eta} \tilde{\Lambda}_r \tilde{q}_r, \end{aligned} \tag{3.109}$$

The following theorem employs the sector conditions introduced in Lemma 3.4.2 and establishes the optimization problem to obtain the AW gains in Fig. 3.5.

Theorem 3.5.5 (Multi-stage AW new design: Peak-to-peak analysis) *Consider the plant* (3.93) *and its nominal controller* (3.71). *Assume that this system is exposed to peak-bounded disturbances with known upper bound* $w_{max} \in \mathbb{R}$, *i.e.,* $w^\top(t)w(t) \leq w_{max}^2$. *Given the bounds* m *and* r *on the actuator magnitude and rate, respectively, assume that for a given* $0 < \alpha < \frac{|Re(\lambda_{min}(A))|}{2}$, *there exists a solution for*

$$\min_{Q,\bar{Q},M_m,M_r,\tilde{M}_r,X_m,X_r,\tilde{X}_r,Y_m,\tilde{Y}_r,\bar{Y}_m,\chi^2,\bar{\chi}^2} c_1\chi^2 + c_2\bar{\chi}^2 \tag{3.110}$$

subject to

$$\begin{pmatrix} QA^\top + AQ + \alpha Q & * & * & * & * \\ B_w^\top & -\alpha I & * & * & * \\ \Phi_{3,1} & 0 & -2M_m & * & * \\ \Phi_{4,1} & KD_{uw} & \Phi_{4,3} & \Phi_{4,4} & * \\ \Phi_{5,1} & KD_{uw} & \Phi_{5,3} & \Phi_{5,4} & \Phi_{5,5} \end{pmatrix} < 0, \tag{3.111}$$

and (4.38), *and* (3.101) *with* $\tilde{Y}_{ri}$ *substituted by* Y_{ri}, *and*

$$\begin{pmatrix} \bar{Q}A^\top + A\bar{Q} + \alpha\bar{Q} & * & * & * \\ B_w^\top & -\alpha I & * & * \\ \bar{\Phi}_{3,1} & 0 & -2M_m & * \\ \bar{\Phi}_{4,1} & KD_{uw} & \Phi_{4,3} & \Phi_{4,4} \end{pmatrix} < 0, \tag{3.112}$$

$$\begin{pmatrix} \bar{Q} & \bar{Q}C_z^\top \\ C_z\bar{Q} & \bar{\chi}^2/w_{max}^2 \end{pmatrix} > 0, \quad \begin{pmatrix} \mathsf{m}_i^2/w_{max}^2 & \bar{Y}_{mi} \\ \bar{Y}_{mi}^\top & \bar{Q} \end{pmatrix} > 0. \tag{3.113}$$

where $i = 1, ..., n_u$, $\tilde{\mathsf{r}} = \frac{\mathsf{r}}{1-s_d}$, *and*

$$M_m = W_m^{-1}, \quad M_r = (W_r s_d)^{-1}, \quad \tilde{M}_r = \tilde{W}_r^{-1}, \tag{3.114}$$

$$X_m = \Lambda_m M_m, \quad X_r = \Lambda_r M_r, \quad \tilde{X}_r = \tilde{\Lambda}_r \tilde{M}_r,$$

$$\Phi_{3,1} = M_m B_{q_m}^\top - X_m^\top B_\eta^\top + [0 \quad 0 \quad I]Q - Y_m,]$$

$$\Phi_{4,1} = M_r B_{q_r}^\top - X_r^\top B_\eta^\top + [C_u - [0 \quad 0 \quad I]]KQ,$$

$$\Phi_{5,1} = \tilde{M}_r B_{q_r}^\top - \tilde{X}_r^\top B_\eta^\top + [C_u - [0 \quad 0 \quad I]]KQ - \tilde{Y}_r,$$

$$\Phi_{4,3} = KD_{uq}M_m - KD_{u\eta}X_m + s_d K[1 \quad 0]X_m,$$

$$\Phi_{4,4} = -2M_r s_d^{-1} - KD_{u\eta}X_r - KX_r^\top D_{u\eta}^\top$$
$$+ s_d K[1 \quad 0]X_r + s_d KX_r^\top [1 \quad 0]^\top,$$

$$\Phi_{5,3} = KD_{uq}M_m - KD_{u\eta}X_m + K[1 \quad 0]X_m,$$

$$\Phi_{5,4} = -\tilde{M}_r - KD_{u\eta}X_r - K\tilde{X}_r^\top D_{u\eta}^\top$$
$$+ K[1 \quad 0]X_r + s_d K\tilde{X}_r^\top [1 \quad 0]^\top,$$

$$\Phi_{5,5} = -2\tilde{M}_r - KD_{u\eta}\tilde{X}_r - K\tilde{X}_r^\top D_{u\eta}^\top$$
$$+ K[1 \quad 0]\tilde{X}_r + K\tilde{X}_r^\top [1 \quad 0]^\top,$$

$$\bar{\Phi}_{3,1} = M_m B_{q_m}^\top - X_m^\top B_\eta^\top + [0 \quad 0 \quad I]\bar{Q} - \bar{Y}_m,$$

$$\bar{\Phi}_{4,1} = M_r B_{q_r}^\top - X_r^\top B_\eta^\top + [C_u - [0 \quad 0 \quad I]]K\bar{Q},$$

with $Y_m = H_m Q$, $\tilde{Y}_r = \tilde{H}_r Q$, $\bar{Y}_m = H_m \bar{Q}$.

The augmented closed loop system (3.109)*, has the same reachable set as (6.11) and performance level gain χ from w to z, as long as the disturbance signals satisfy $w^\top(t)w(t) \le w_{max}^2$ and $x(0) = 0$. Moreover, for moderate levels of saturation specified as $|\eta| \le \tilde{\mathsf{r}} = \frac{\mathsf{r}}{1-s_d}$, $\bar{\chi}$ is the upper bound for the performance level.*

Proof. Following the sketch of proof of Theorem 3.5.4, inequality (3.111) is equivalent to

$$\begin{aligned}&\frac{d}{dt}(x^\top Q^{-1}x) + \alpha x^\top Q^{-1}x - \alpha w^\top w \\ &- 2q_m^\top W_m(q_m - \delta + H_m x) - 2q_r^\top W_r(q_r - s_d u_d) \\ &- 2\tilde{q}_r^\top W_r(\tilde{q}_r - \eta + \tilde{H}_r x) < 0.\end{aligned} \tag{3.115}$$

Invoking Lemma 3.4.2, (3.115) reduces to (5.12), thus stability is guaranteed with performance level χ, based on the proof of Theorem 3.5.4.

For moderate levels of saturation specified as $|\eta| < \tilde{\mathsf{r}} = \frac{\mathsf{r}}{1-s_d}$, the sector condition $u_d \longmapsto q_r \in [0 \quad s_d I]$ is in effect and according to *Lemma* 3.4.2, the inequality $q_r^\top W_r(q_r - s_d u_d) \le 0$ will be satisfied. Using the Lyapunov function $V = x^\top \bar{Q}^{-1} x$ and following the same sketch of the proof of *Theorem 4.1*, the inequality (3.112), leads to

$$\frac{d}{dt}(x^\top \bar{Q}^{-1}x) + \alpha x^\top Q^{-1}x - \alpha w^\top w < 0, \tag{3.116}$$

and the left inequality in (3.113) establishes $\bar{\chi}$ as the performance measure, if the additional saturation element avoids activation. The feasibility of the multi-stage design is discussed in *Section* 3.7.2. $\square$

Remark 3.5.3 *Inequalities* (3.111) *and* (3.113) *ensure that the closed-loop system is stable with gain* χ*, while* (3.112) *indicates gain* $\bar{\chi}$ *in case of a command with rate of change below* $\tilde{\mathsf{r}} = \frac{\mathsf{r}}{1-s_d}$*. For moderate saturation cases, larger values for* c_2 *can be used in order to achieve lower values for* $\bar{\chi}$ *and thus, more aggressive AW gains. This is at the cost of a larger* χ*, which is the guaranteed gain for the closed-loop, without any assumptions on the rate signal. Here,* $\bar{\chi}$ *can be seen as a measure of the aggressiveness of AW gains.*

3.6 Simulation Results

The performance of the new single and multi-stage AW designs, using the energy-to-peak and peak-to-peak approaches, are presented in this section. The proposed techniques have been evaluated on both SISO and MIMO systems.

3.6.1 SISO Example

Consider the example from [14], for an aircraft pitch dynamics with the unconstrained system block diagram shown in Fig. 3.6. The aircraft transfer function $G_p(s)$ with the pitch rate, $\dot{\theta}$, as output, and the elevator deflection, δ, as input, is given by

$$G_p(s) = \frac{\dot{\theta}(s)}{\delta(s)} = \frac{-10(s+1)(s+0.01)}{(s^2+2s+2)(s^2+0.02s+0.0101)}.$$

For above transfer function, a forth-order minimal state-space representation is obtained with system matrices in controllable canonical form given by

$$\left[\begin{array}{c|c|c} A_p & B_2 & B_1 \\ \hline C_2 & D_{22} & D_{21} \end{array}\right] = \left[\begin{array}{cccc|c|c} -2.0200 & -2.0501 & -0.0602 & -0.0202 & 1 & 0 \\ 1 & 0 & 0 & 0 & 0 & 0 \\ 0 & 1 & 0 & 0 & 0 & 0 \\ 0 & 0 & 1 & 0 & 0 & 0 \\ \hline 0 & -10 & -10.1 & -0.10 & 0 & 0 \end{array}\right], \tag{3.117}$$

The performance output is then taken to be $z = y - w$.

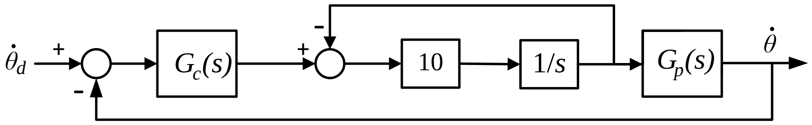

Figure 3.6: An aircraft pitch rate feedback control system.

First order controller

We use the suggested compensator in [14], which is a lead compensator designed for the unconstrained system given by

$$G_c(s) = -4\frac{s+2}{s+22}. \tag{3.118}$$

The input to the controller is the error signal $e = w - y$. To be consistent with the state-space representation given by (3.71), the reference signal w and the measurement output y are applied to the controller through two separate channels with $B_{cw} = -B_{cy}$. The first-order state-space realization of the controller is thus given by

$$\left[\begin{array}{c|c|c} A_c & B_{cy} & B_{cw} \\ \hline C_c & D_{cy} & D_{cw} \end{array}\right] = \left[\begin{array}{c|c|c} -22 & -1 & 1 \\ \hline 80 & 4 & -4 \end{array}\right]. \tag{3.119}$$

Second order controller

To verify the benefit that can be gained from the new design for anti-windup augmentation in multi-state unconstrained controllers, a lag compensator is added to the lead controller used in Section 3.6.1. The pole and zero of the lag part is selected close enough to the origin and to each other such that the response of the closed-loop system is not significantly affected by adding the lag controller. The new controller transfer function is now given by

$$G_c(s) = -4\frac{s+2}{s+22}\frac{s+0.0125}{s+0.0034}. \tag{3.120}$$

with the second order state-space realization

$$\left[\begin{array}{c|c|c} A_c & B_{cy} & B_{cw} \\ \hline C_c & D_{cy} & D_{cw} \end{array}\right] = \left[\begin{array}{cc|c|c} -22.0034 & -0.0748 & -1 & 1 \\ 1 & 0 & 0 & 0 \\ \hline 79.9636 & 0.1992 & 4 & -4 \end{array}\right]. \tag{3.121}$$

A settling time of less than 2 seconds and overshoot of less than 10% are the specification met by adding the controllers. Both the first and second order controllers achieve the same performance for the unconstrained closed-loop system.

Figure 3.7 compares the performance of the lead (single-state) and the lead-lag (double-state) controllers for the unconstrained system. A settling time of less than 2 seconds and percent overshoot of less than %10 are the specification met by adding the controllers. According to the figure, it is clear that the both the single-state and double-state controllers achieve the same performance for the unconstrained closed-loop system.

3.6.2 $\mathscr{L}_2$ Gain Results

Throughout this section, the performance of standard and new MRAW designs are compared. The AW gains used in this section are designed for the $\mathscr{L}_2$ gain approach

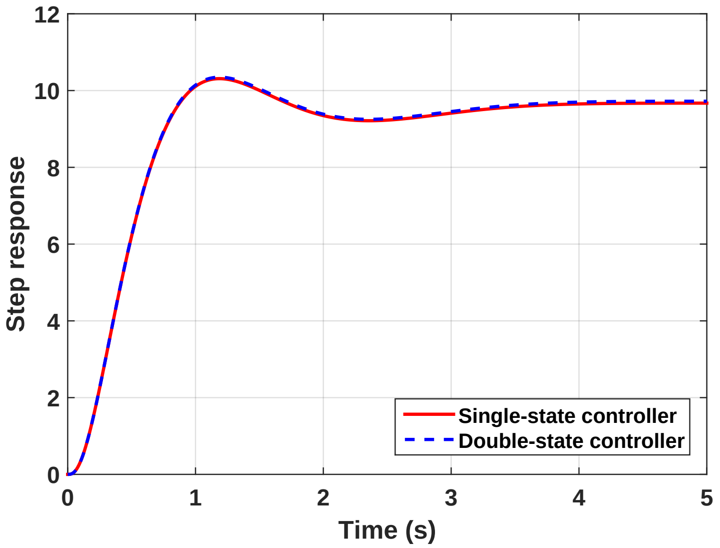

Figure 3.7: Step response of the unconstrained plant using a single and a double state controller.

(assuming a norm bounded disturbance $||w||_2 \leq s$, and solving for a guaranteed $\mathscr{L}_2$ gain of γ from w to z, $||z||_2^2 \leq \gamma^2 ||w||_2^2$). The algorithms for the standard $\mathscr{L}_2$ gain AW (without the Γ signal) can be found in e.g. [19] and [50]. The modification to incorporate the new Γ loop is quite similar to Theorem 3.5.4 and is not repeated.

The standard design is feasible for relatively high rate bounds when the signal is only moderately saturated. Therefore, for the $\mathscr{L}_2$ gain approach we are able to compare the effect of the AW gains achieved by the standard design to the ones the new design offers.

In Fig. 3.8, the magnitude and rate limits are selected as $m = 1, r = 11$, respectively, where the latter is the lowest value for r resulting in feasible LMIs for the standard design. In this example $s = 1$ and the reference signal is a unit step with duration of 1 second, satisfying the condition $||w||_2 < s$. When both of the standard and new approaches are able to solve problem, the AW gains achieved by the new design (bottom chart of Fig. 3.8) perform better than the traditional design gains (top chart), and are able to almost recover the performance of the unconstrained system.

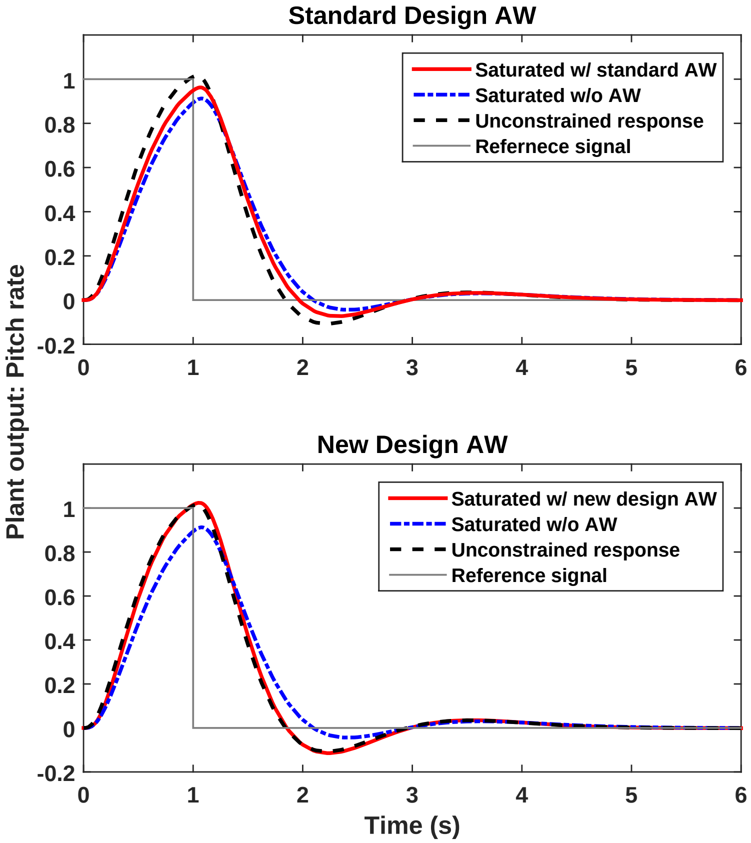

Figure 3.8: Performance of the standard and new AW designs using the $\mathscr{L}_2$ gain approach with $m = 1, r = 11$.

In order to better visualize the performance of the new design in improving the system response, the value of the rate bound is decreased and thus the rate signal saturates more. As mentioned before, the standard design is not feasible for low rate limits, while the new AW design is feasible and improves the performance of the saturated system significantly (Fig. 3.9). In Fig. 3.9, the limits are selected

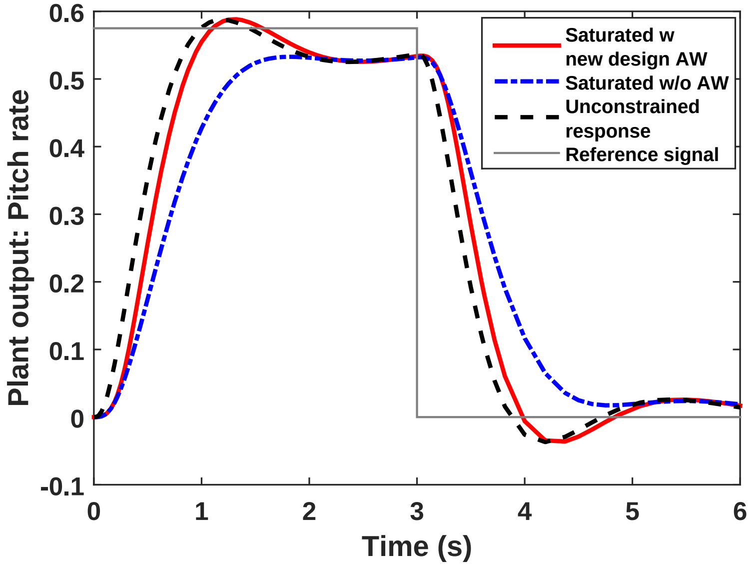

Figure 3.9: Performance of the new AW designs for low rate limits using the $\mathscr{L}_2$ gain approach $m = 1, r = 2$.

as $m = 1, r = 2$, and $s = 1$. As shown in Fig. 3.9, a step signal with peak value of less than 1 and duration of 3 seconds is selected as the reference signal $w(t) = \dot{\theta}_d(t)$, in order to capture the settling behavior of the system while not violating the disturbance bound $||w(t)||_2 < 1$ for all t.

The simulation results for the $\mathscr{L}_2$ gain approach are summarized in Table 3.1. The new design gives a much better performance measure. To summarize, using the $\mathscr{L}_2$

Table 3.1: Performance comparison for the $\mathscr{L}_2$ gain approach

r	$\gamma_{standard}$	γ_{new}
11	36.3457(Fig. 3.8 top)	1.3476 (Fig. 3.8 bottom)
2	not feasible	1.5223 (Fig. 3.9)

gain approach, both the standard and new MRAW designs are feasible for moderate rate saturation bounds ($r \geq 11$), while only the new design is feasible for lower limits. Similar result for the second-order controller (3.121) is achieved which is omitted to avoid repetition.

3.6.3 Peak-to-Peak Results

The results presented in this chapter (Theorem 3.5.4) are used to obtain the AW gains using the peak-to-peak approach. The peak-to-peak approach, using the standard AW design, is feasible for even higher bounds compared to the $\mathscr{L}_2$ gain approach presented in Section 3.6.2. The lowest rate limit for which the standard design is feasible ($r = 68$) does not saturate the rate signal significantly. The new design is feasible for much lower saturation bounds and the AW gains are capable of improving the performance significantly. Therefore, all of the results presented for the peak-to-peak approach are using the new MRAW design.

Figure 3.10 shows the influence of the new MRAW design in improving the performance of the magnitude and rate saturated system using the lead unconstrained compensator (single-state) in (3.118). In this figure the limits are selected as $m = 5, \quad r = 15$, and $w_{max} = 1$. The value of $\alpha = 0.03$ is selected based on a line search to reach the best performance measure χ. The peak-to-peak analysis allows for a more aggressive reference signal such as repeated step signals with peak value less than or equal to 1. This makes it possible to achieve higher rate saturation, and thus, more visible AW effect.

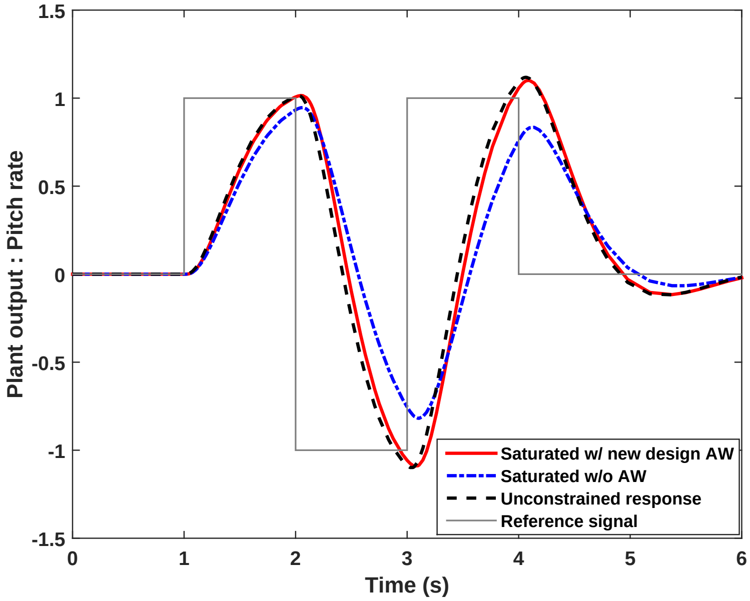

Figure 3.10: Performance of the new AW design using the peak-to-peak approach and the lead (single-state) controller, with $m = 5, r = 15$, and $w_{max} = 1$.

The simulation results for the peak-to-peak approach using the single-state controller are summarized in Table. 3.2. The new design gives a much better performance measure (lower χ). The same conclusion can be made for the second order controller in (3.121).

Table 3.2: Performance comparison for the peak-to-peak approach

r	$\chi_{standard}$	χ_{new}
70	57.7173	9.1070
15	not feasible	10.3157 (Fig. 3.10)

To better visualize the role of the AW technique in improving the saturated system performance, the controller's output and plant's input signals are plotted in Figures 3.11 and 3.12, respectively. In these figures, the effects of magnitude and rate saturation on control commands are shown. According to Fig. 3.11, the AW augmentation reduces the control command in order to minimize the drawbacks of input saturation.

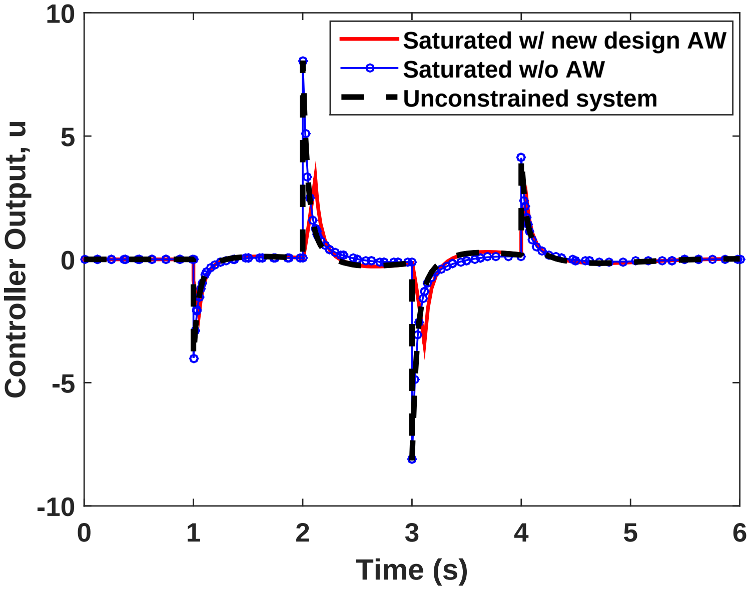

Figure 3.11: Controller output u, before saturation, with $m = 5, r = 15$, and $w_{max} = 1$.

Figure 3.12 shows the variation of the elevator deflection as the plant input. Although the AW augmentation pushes the controller to send a smaller signal (Fig. 3.11), it performs much better than the saturated system in recovering the plant input of the unconstrained system (Fig. 3.12). This is obtained by limiting the rate at which the input signal can change as shown by Fig. 3.13.

The performance of the new MRAW design using the second order lead-lag unconstrained compensator (3.121), is identical to the result shown in Fig. 3.10 for the lead controller. Details are omitted due to space limitation.

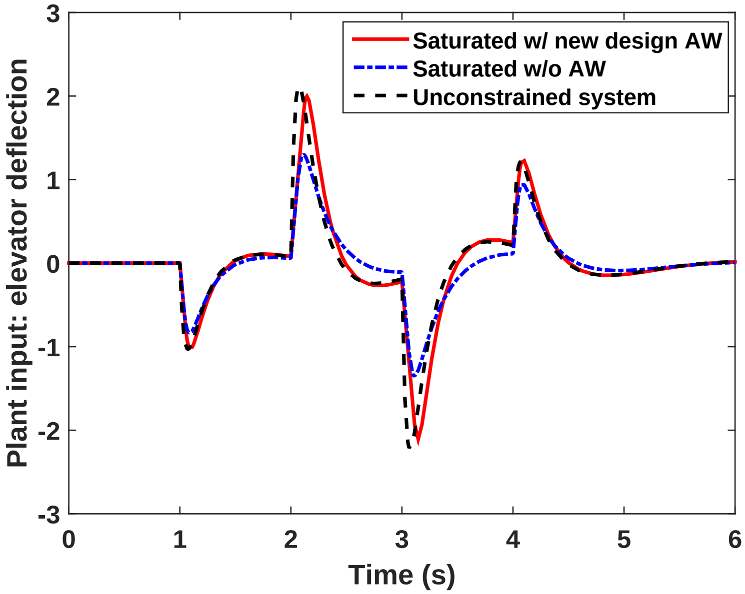

Figure 3.12: Plant input, u_p, with $m = 5, r = 15$, and $w_{max} = 1$.

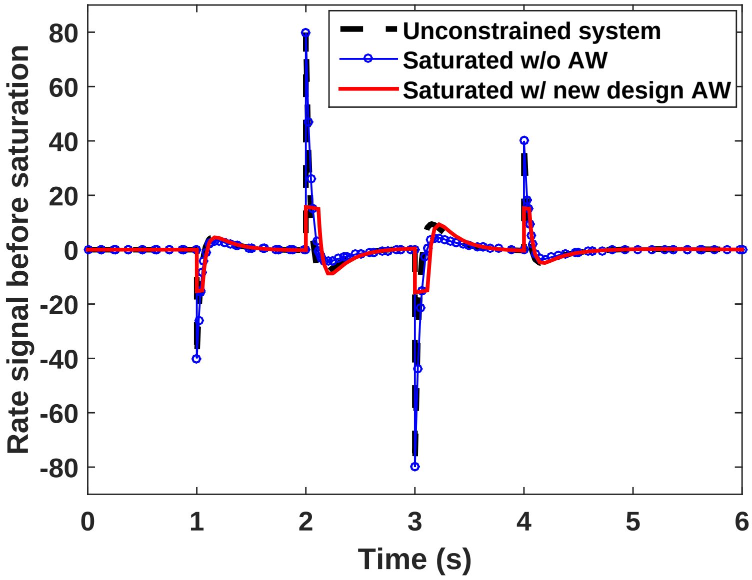

Figure 3.13: Rate signal before saturation, η, with $m = 5, r = 15$, and $w_{max} = 1$.

Multi-stage case: Using the peak-to-peak method, the lowest rate limit for which the standard design is feasible, $r = 68$, does not saturate the rate signal significantly.

The new design is feasible for much lower saturation bounds and the AW gains achieved are capable of improving the performance significantly.The limits for the input magnitude and rate are selected as $\mathsf{m} = 6$ and $\mathsf{r} = 10$, respectively.

For this example, the value of s_d is selected to be 0.2 and w_{max} is 1. Using the multi-stage design with $c_1 = 1$ and $c_2 = 10$, the static gains $\Lambda_m = [-0.3425 \quad 0.8710]^\top$, $\Lambda_r = [-0.0140 \quad -0.0344]^\top$, and $\tilde{\Lambda}_r = [-0.0651 \quad 0.2106]^\top$ are achieved with a guaranteed regional performance level of $\delta = 8.7359$. Moreover, assuming low to moderate rate saturation, a better performance measure of $\bar{\delta} = 6.7404$ can be achieved through a more aggressive AW design. The single-stage magnitude and rate anti-windup compensation results in $\delta = 7.701$ with $\Lambda_m = [-0.4664 \quad 1.4056]^\top$, $\Lambda_r = [-0.0258 \quad 0.0201]^\top$. The response of the system to a reference signal satisfying $w^\top w \leq 1$ is shown in Fig. 3.14 using both the multi-stage and the single-stage magnitude and rate AW designs. The response of the multi-stage design is closer to the performance of the unconstrained system, as the multi-stage design has improved the performance.

Figure 3.15 and Table 3.3 compare the response of the multi-stage augmentation using different s_d values, and the corresponding AW gains are reported in Table. 3.4. According to the table, a smaller s_d value allows for a better performance measure $\bar{\delta}$ assuming low to moderate saturation levels. Increasing the s_d, the effect of the multi-stage design becomes less and for s_d values close to 1 the performance of the single-stage design is recovered.

Figure 3.16 and Table 3.5 compare the response of the multi-stage augmentation using different c_2 values. By using a larger value for c_2, more aggressive AW gains

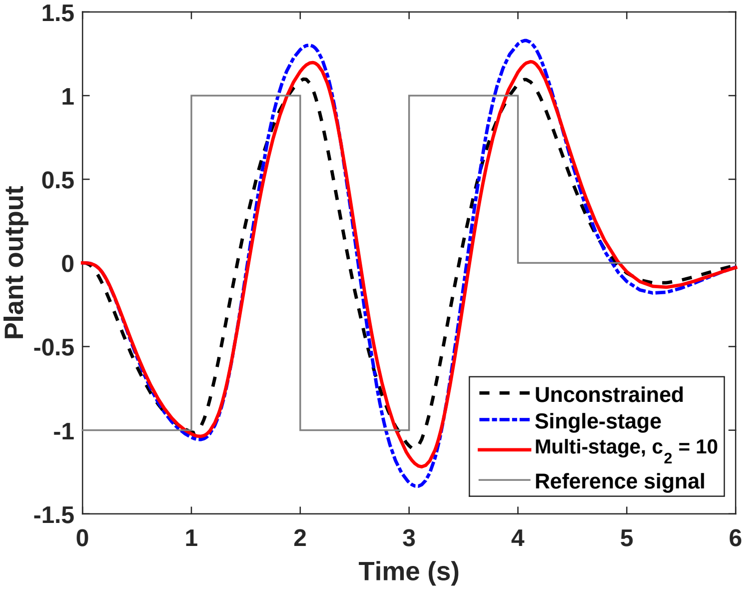

Figure 3.14: Performance of the multi-stage MRAW compared to the single-stage with $r = 6, m = 10, s_d = 0.2, \alpha = 0.03$.

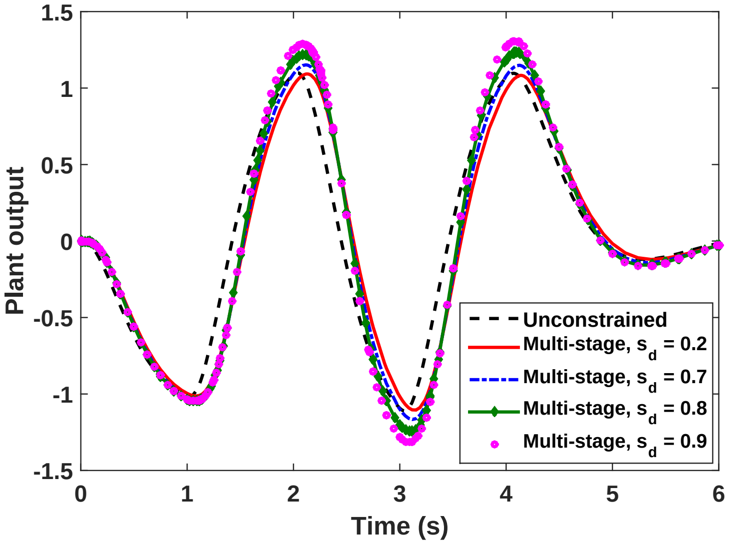

Figure 3.15: Performance of the multi-stage MRAW with different s_d values and $r = 6, m = 10, c_2 = 100, \alpha = 0.03$.

Table 3.3: Performance of the multi-stage MRAW with different s_d values with $r = 6, m = 10, c_2 = 100, \alpha = 0.03$

s_d	$\bar{\delta}$	δ
0.9	8.374	14.607
0.8	7.683	13.330
0.7	7.320	12.949
0.2	6.671	11.150

Table 3.4: Multi-stage MRAW gains for different s_d values with $r = 6, m = 10, c_2 = 100, \alpha = 0.03$

s_d	Λ_m	Λ_r	$\tilde{\Lambda}_r$
0.9	$[-0.3926, 1.0936]^\top$	$[-0.0169, -0.0204]^\top$	$[0.0855, -0.4954]^\top$
0.8	$[-0.3528, 0.9045]^\top$	$[-0.0200, -0.0062]^\top$	$[-0.1460, 0.5944]^\top$
0.7	$[-0.3274, 0.7867]^\top$	$[-0.0211, -0.0012]^\top$	$[-0.0180, -0.0125]^\top$
0.2	$[-0.2644, 0.5073]^\top$	$[-0.0015, -0.0925]^\top$	$[-0.0435, 0.1154]^\top$

for moderate saturation levels can be achieved which results in a lower $\bar{\delta}$ and thus a better performance. However, this is at a cost of a larger δ to guarantee the stability of the closed-loop system under general conditions. According to Table. 3.5 and Fig. 3.16, it is clear that by increasing c_2 the weight on the performance measure $\bar{\delta}$ is increased which results in a smaller $\bar{\delta}$ and a response closer to the unconstrained system performance for moderate saturation levels.

The corresponding AW gains for the multi-stage design using different s_d values are reported in Table. 3.6.

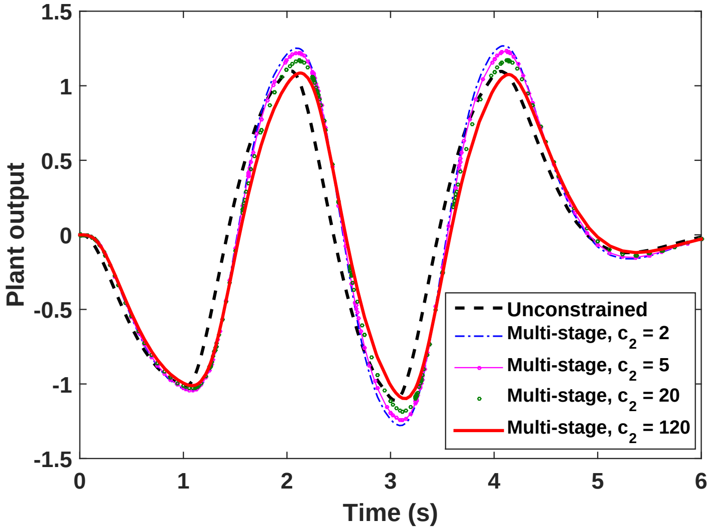

Figure 3.16: Performance of the multi-stage MRAW with different c_2 values and $r = 6, m = 10, s_d = 0.2, \alpha = 0.03$.

Table 3.5: Performance of the multi-stage MRAW with different c_2 values, with $r = 6, m = 10, s_d = 0.2, \alpha = 0.03$

c_2	$\bar{\delta}$	δ
2	6.885	8.139
5	6.791	8.433
20	6.704	9.138
120	6.669	11.473

Table 3.6: Multi-stage MRAW gains for different c_2 values, with $r = 6, m = 10, s_d = 0.2, \alpha = 0.03$

c_2	Λ_m	Λ_r	$\tilde{\Lambda}_r$
2	$[-0.3997, 1.1241]^\top$	$[-0.0351, 0.0645]^\top$	$[-1.3096, 6.0657]^\top$
5	$[-0.3666, 0.9788]^\top$	$[-0.0211, -0.0013]^\top$	$[-2.5226, 11.8480]^\top$
20	$[-0.3176, 0.7585]^\top$	$[-0.0088, -0.0585]^\top$	$[-2.0198, 9.6228]^\top$
120	$[-0.2581, 0.4770]^\top$	$[-0.0010, -0.0951]^\top$	$[-0.0360, 0.0789]^\top$

3.6.4 MIMO Example

In this section, the yaw/roll dynamics of an EMRAAT BTT missile model with system matrices is used to evaluate the performance of the proposed single-stage MRAW technique on MIMO plants. Here, the rudder and aileron angles are inputs controlled by actuators and the side slip angle and yaw rate are outputs measured by sensors. Actuators are assumed to have magnitude limits of m = 8 and rate limits of $r_1 = 60$ and $r_2 = 20$. According to Fig. 3.17, the performance of the systems degrades significantly due to actuator saturation and the proposed AW techniques is successful in recovering the performance of the unconstrained system. As a matter of fact, the performance of the new AW structure with $\chi_{new} = 52.5$ is considerably better than the performance of the standard design with $\chi_{old} = 122.2$ using $\alpha = 0.008$.

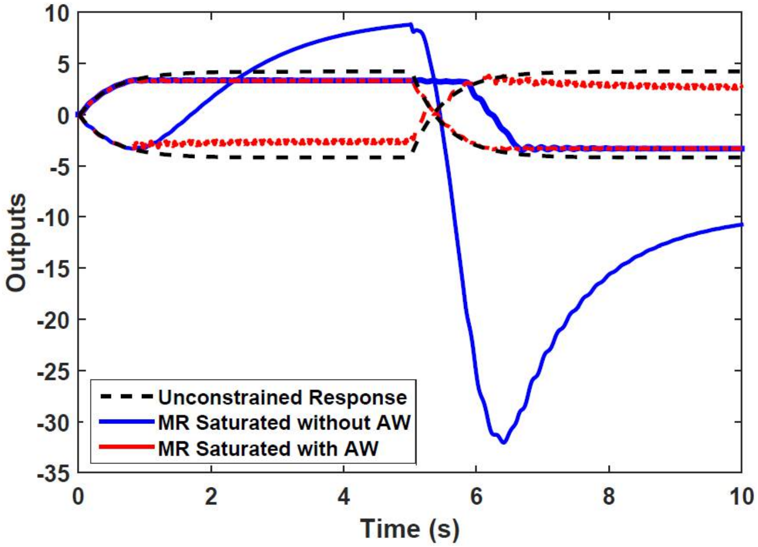

Figure 3.17: Response of the magnitude and rate saturated system with $m = 8; r_1 = 60; r_2 = 20$, with and without new peak-to-peak AW compensation.

3.6.5 Summary

The multi-stage AW compensation with a novel structure for peak bounded exogenous signals is presented. The new structure and the additional stage help reduce the conservatism encountered in the more traditional approaches, particularly for cases in which saturation is not persistent and the commands does not far exceed the actuator limitations. The benefit of the new AW structure is observed in both energy-to-peak and peak-to-peak approaches in terms of a better performance and the possibility to manage tighter rate bounds.

3.7 Feasibility Analysis

3.7.1 Standard Design: Energy-to-Peak

The feasibility of the multi-stage design *Theorem 3.4.3* is the same as the single-stage design *Theorem 3.4.1* since if *Theorem 3.4.1* has a solution, there is always one solution for *Theorem 3.4.3* by setting the 'bar' variables to be the same as the original ones used in *Theorem 3.4.1*. In fact, as it is clear in the numerical examples, the presence of $\bar{Q}$, $\bar{\gamma}$, and $\bar{Y}_m$, increases the degrees of freedom and allows for a better performance, i.e. smaller $\bar{\gamma}$. Moreover, the discussion in this section shows that the feasibility condition of the multi-stage design (*Theorem 4.1*) is also guaranteed by the feasibility of the single-stage design in which the artificial rate saturation block has not been used. As a result, adding the artificial element and obtaining more aggressive AW gains do not alter the solvability of the problem.

To show this, recall that the sufficient conditions for the multi-stage problem were (3.44) and (3.45). The next lemma investigates equivalent forms to gain a better understanding of the feasibility conditions.

Lemma 3.7.1 (Elimination lemma for multi-stage design) *The Linear Matrix inequality presented in* (3.44) *is feasible if and only if*

$$\begin{pmatrix} QA^\top + AQ & * & * \\ B_w^\top & -I & * \\ C_z Q & D_{zw} & -\gamma^2 I \end{pmatrix} < 0, \tag{3.122}$$

and

$$\begin{aligned} R &< 0, \\ R - NM^{-1}N^\top &< 0, \end{aligned} \tag{3.123}$$

in which

$$R = \begin{pmatrix} R_{11} & * & * & * & * \\ B_1^\top & -I & * & * & * \\ R_{31} & D_{11} & -\gamma^2 I & * & * \\ R_{41} & 0 & -M_m D_{12}^\top & -2M_m & * \\ R_{51} & 0 & R_{53} & R_{54} & R_{55} \end{pmatrix}, \tag{3.124}$$

with

$$\begin{aligned}
R_{11} &= He(A_p Q_{11} + B_2 Q_{13}^\top), && (3.125)\\
R_{31} &= C_1 Q_{11} + D_{12} Q_{13}^\top,\\
R_{41} &= -M_m B_2^\top + Q_{13}^\top - \sum_{i=1}^{3} H_{mi} Q_{1i}^\top,\\
R_{51} &= -\sum_{i=1}^{3} \tilde{H}_{ri} Q_{1i}^\top,\\
R_{53} &= -Q_{13}^\top C_1^\top - Q_{33} D_{12}^\top,\\
R_{54} &= -Q_{33} + (\sum_{i=1}^{3} H_{mi} Q_{i3})^\top,\\
R_{55} &= He(\sum_{i=1}^{3} \tilde{H}_{ri} Q_{i3}),
\end{aligned}$$

and

$$\begin{aligned}
N &= \begin{pmatrix} -\sum_{i=1}^{3} \tilde{H}_{ri} Q_{1i}^\top & 0 & 0 & 0 & -M_r + \sum_{i=1}^{3} \tilde{H}_{ri} Q_{i3} \end{pmatrix}^\top, && (3.126)\\
M &= -2M_r s_d^{-1}.
\end{aligned}$$

Proof. In order to show the feasibility of the multi-stage magnitude and rate AW, the elimination lemma is applied. First, (3.44) is represented as

$$\Psi + \mathrm{He}\{G^\top [\tilde{X}_r \quad X_r \quad X_m]^\top H\} < 0, \tag{3.127}$$

where Ψ is a part of (3.44) that does not have X_m, X_r, $\tilde{X}_r$, and

$$G = \begin{pmatrix} 0 & 0 & 0 & 0 & 0 & I \\ 0 & 0 & 0 & 0 & I & 0 \\ 0 & 0 & 0 & I & 0 & 0 \end{pmatrix}, \tag{3.128}$$

$$H = \begin{pmatrix} -B_\eta^\top & 0 & 0 & 0 & -D_{u\eta}^\top K & -D_{u\eta}^\top K \end{pmatrix},$$

$$\Psi = \begin{pmatrix} QA^T + AQ & * & * & * & * & * \\ B_w^T & -I & * & * & * & * \\ C_z Q & D_{zw} & -\gamma^2 I & * & * & * \\ M_m B_{q_m}^T + [0 \quad 0 \quad I]Q - Y_m & 0 & M_m D_{zq}^T & -2M_m & * & * \\ M_r B_{q_r}^T + [C_u - [0 \quad 0 \quad I]]KQ & KD_{uw} & 0 & KD_{uq}M_m & -2M_r s_d^{-1} & * \\ \tilde{M}_r B_{q_r}^T + [C_u - [0 \quad 0 \quad I]]KQ - \tilde{Y}_r & KD_{uw} & 0 & KD_{uq}M_m & -\tilde{M}_r & -2\tilde{M}_r \end{pmatrix} < 0, \tag{3.129}$$

Since,

$$\mathscr{N}_G = \begin{pmatrix} I & 0 & 0 & 0 & 0 & 0 \\ 0 & I & 0 & 0 & 0 & 0 \\ 0 & 0 & I & 0 & 0 & 0 \end{pmatrix}^\top, \tag{3.130}$$

$\mathscr{N}_G^\top \Psi \mathscr{N}_G < 0$ results in (3.122). For $\mathscr{N}_H^\top \Psi \mathscr{N}_H < 0$, the Q matrix needs to be partitioned as

$$Q = \begin{pmatrix} Q_{11} & Q_{12} & Q_{13} \\ Q_{12}^\top & Q_{22} & Q_{23} \\ Q_{13}^\top & Q_{23}^\top & Q_{33} \end{pmatrix}. \tag{3.131}$$

Substituting for B_η and $D_{u\eta}$ from (3.14) in the H matrix, the null space of H is given by

$$\mathscr{N}_H = \begin{pmatrix} I & 0 & 0 & 0 & 0 & 0 & 0 & 0 \\ 0 & 0 & 0 & I & 0 & 0 & 0 & 0 \\ 0 & 0 & 0 & 0 & I & 0 & 0 & 0 \\ 0 & 0 & 0 & 0 & 0 & I & 0 & 0 \\ 0 & 0 & -I & 0 & 0 & 0 & I & 0 \\ 0 & 0 & 0 & 0 & 0 & 0 & -I & I \end{pmatrix}^\top . \tag{3.132}$$

The second condition of (3.4) after a row-column manipulation can be expressed as

$$\mathscr{N}_H^\top \Psi \mathscr{N}_H = \left(\begin{array}{c|c} R & N \\ \hline N^\top & M \end{array}\right) < 0, \tag{3.133}$$

with R, M, and N matrices given in (3.124)-(3.126).

Recalling the Schur complement, (3.133) is equivalent to (3.123). $\square$

Note that, (3.122) implies that the nominal (unsaturated) closed-loop has an $\mathscr{L}_2$ gain of γ. This is similar to the conditions encountered in the gain-saturation problem. The condition in (3.123), however, looks quite different from the second condition in magnitude only problem, which is stability and performance of the open-loop. This is in part due to the need for the slack variables, since the nominal open loop has a zero eigenvalue, and in part due to avoiding the assumption on availability of the time derivative of the compensator output.

Finally, we present the equivalent feasibility result for the single-stage (no artificial saturation element case).

Lemma 3.7.2 (Elimination lemma for single-stage design) *The single-stage anti-windup is feasible if and only if*

$$\begin{pmatrix} QA^\top + AQ & * & * \\ B_w^\top & -I & * \\ C_zQ & D_{zw} & -\gamma^2 I \end{pmatrix} < 0, \tag{3.134}$$

and

$$\bar{R} < 0, \tag{3.135}$$

where $\bar{R}$ is equivalent to R in (3.124)*, except for $\tilde{H}_r$ which is replaced by H_r.*

Proof. In the single-stage design the artificial saturation block is removed, thus, we do not have s_d anymore. If we apply *Lemma 3.4.2* to the two saturation elements, the main LMI condition for the single-stage design will be similar to the multi-stage LMI (3.88) excluding its last row and column, and

$$\begin{aligned} \Phi_{5,1} &= M_r B_{q_r}^\top - X_r^\top B_\eta^\top + [C_u - [0 \quad 0 \quad I]]KQ - Y_r, \\ \Phi_{5,5} &= -2M_r - KD_{u\eta}X_r - KX_r^\top D_{u\eta}^\top, \end{aligned} \tag{3.136}$$

where $Y_r = H_r Q$. Following the proof of *Lemma 5.1*, we have

$$G = \begin{pmatrix} 0 & 0 & 0 & 0 & 0 & I \\ 0 & 0 & 0 & 0 & I & 0 \end{pmatrix}, \tag{3.137}$$

$$H = \begin{pmatrix} -B_\eta^\top & 0 & 0 & 0 & -D_{u\eta}^\top K \end{pmatrix},$$

with $\mathscr{N}_G$ similar to (3.130) and $\mathscr{N}_H$ similar to (3.132) after removing its last row and column. The elimination lemma conditions of (3.4) are then lead to (3.134) and (3.135), respectively. $\square$

Remark 3.7.1 *The elimination lemma established that the main inequality of the single-stage design is equivalent to* (3.134) *and* $\bar{R} < 0$*, which is the same as the first line of* (3.135)*, except for* $\tilde{H}_r$ *which is replaced by* H_r *in* $\bar{R}$*. It is clear that this difference will not affect the feasibility conditions, though it may not result in an exactly the same* γ *value.*

Remark 3.7.2 *According to equations* (3.124)-(3.126)*, since the free variable* M_r *only appears in matrix* M*, there exists the possibility to make the second term in* $R + NM^{-1}N^\top < 0$ *arbitrary small, by choosing* M_r *to be large enough. Therefore, the feasibility condition for the multi-stage design reduces to the feasibility condition of the single-stage design. Therefore, if the single stage problem is solvable, then the multi-stage problem (Theorem 3.4.2) will also have solutions.*

3.7.2 New Design: Peak-to-Peak

In this section we show that the feasibility of the multi-stage design (*Theorem* 3.5.5) is the same as the feasibility of the single-stage design (*Theorem* 3.5.4). Note that with $\bar{Q} = Q$ and $\bar{\chi} = \chi$, inequalities (3.99) and (3.112) are equivalent, and inequality (3.112) is the (1:4,1:4) block of (3.111). As a result, if (3.111) is feasible, then there exists at least one set of decision variables that make (3.112) and (3.113) feasible. In fact, the presence of $\bar{Q}, \bar{\chi}$, increases the degrees of freedom and allows for a better performance. Therefore, here we only study inequality (3.111) for the feasibility of the multi-stage design. It thus remains to show that feasibility of (3.111) is equivalent to that of (3.99).

Feasibility of Multi-Stage Design

Lemma 3.7.3 (Elimination Lemma for Multi-stage Design) *The matrix inequality presented in* (3.111) *is feasible if and only if*

$$\begin{pmatrix} QA^\top + AQ + \alpha Q & * \\ B_w^\top & -\alpha I \end{pmatrix} < 0, \tag{3.138}$$

and

$$R < 0 \quad \text{and} \quad R - NM^{-1}N^\top < 0. \tag{3.139}$$

in which $M = -2M_r s_d^{-1}$, *and*

$$N = \begin{pmatrix} -\sum_{i=1}^{3} \tilde{H}_{ri} Q_{1i}^{\top} & 0 & 0 & -M_r + \sum_{i=1}^{3} \tilde{H}_{ri} Q_{i3} \end{pmatrix}^{\top} \tag{3.140}$$

$$R = \begin{pmatrix} R_{11} & * & * & * \\ B_1^{\top} & -\alpha I & * & * \\ R_{31} & 0 & -2M_m & * \\ R_{41} & 0 & R_{43} & R_{44} \end{pmatrix}, \tag{3.141}$$

with

$$R_{11} = He(A_p Q_{11} + B_2 Q_{13}^{\top}) + Q_{11}\alpha, \tag{3.142}$$

$$R_{31} = C_1 Q_{11} + D_{12} Q_{13}^{\top},$$

$$R_{41} = -\sum_{i=1}^{3} \tilde{H}_{ri} Q_{1i}^{\top} + Q_{13}^{\top}\alpha,$$

$$R_{43} = -Q_{33} + \left(\sum_{i=1}^{3} H_{mi} Q_{i3}\right)^{\top},$$

$$R_{44} = He\left(\sum_{i=1}^{3} \tilde{H}_{ri} Q_{i3}\right)^{\top} + Q_{33}\alpha.$$

Proof. In order to show the feasibility of the multi-stage magnitude and rate AW, the elimination lemma is applied. First, (3.111) is represented as

$$\Psi + \mathrm{He}\{G^{\top}[\tilde{X}_r \quad X_r \quad X_m]H\} < 0, \tag{3.143}$$

where Ψ is a part of (3.111) that does not have X_m, X_r, $\tilde{X}_r$, and

$$G = \begin{pmatrix} 0 & 0 & 0 & 0 & I \\ 0 & 0 & 0 & I & 0 \\ 0 & 0 & I & 0 & 0 \end{pmatrix}^\top, \quad \mathscr{N}_G = \begin{pmatrix} I & 0 & 0 & 0 & 0 \\ 0 & I & 0 & 0 & 0 \end{pmatrix}^\top \tag{3.144}$$

$$H = \begin{pmatrix} -B_\eta^\top & 0 & 0 & -D_{u\eta}^\top K & -D_{u\eta}^\top K \end{pmatrix}.$$

Therefore, $\mathscr{N}_G^\top \Psi \mathscr{N}_G < 0$ results in (3.138). For $\mathscr{N}_H^\top \Psi \mathscr{N}_H < 0$, the Q matrix needs to be partitioned as

$$Q = \begin{pmatrix} Q_{11} & Q_{12} & Q_{13} \\ Q_{12}^\top & Q_{22} & Q_{23} \\ Q_{13}^\top & Q_{23}^\top & Q_{33} \end{pmatrix}. \tag{3.145}$$

Substituting for B_η and $D_{u\eta}$ from (3.95) in the H matrix, the null space of H is given by

$$\mathscr{N}_H = \begin{pmatrix} I & 0 & 0 & 0 & 0 & 0 & 0 \\ 0 & 0 & 0 & I & 0 & 0 & 0 \\ 0 & 0 & 0 & 0 & I & 0 & 0 \\ 0 & 0 & I & 0 & 0 & -I & 0 \\ 0 & 0 & 0 & 0 & 0 & -I & I \end{pmatrix}^\top. \tag{3.146}$$

The second condition of (3.4) after a row-column manipulations can be expressed as

$$\mathscr{N}_H^\top \Psi \mathscr{N}_H = \left(\begin{array}{c|c} R & N \\ \hline N^\top & M \end{array}\right) < 0, \tag{3.147}$$

with R, M, and N matrices given in (3.140). Recalling the Schur complement, (3.147) is equivalent to (3.139). □

Feasibility of Single-Stage Design

In this section the feasibility conditions of the single-stage magnitude and rate anti-windup design is studied.

Lemma 3.7.4 (Elimination Lemma for Single-Stage Design) *The matrix inequality presented in* (3.99) *is feasible if and only if*

$$\begin{pmatrix} QA^\top + AQ + \alpha Q & * \\ B_w^\top & -\alpha I \end{pmatrix} < 0, \quad \textit{and} \quad \bar{R} < 0, \tag{3.148}$$

where $\bar{R}$ is equivalent to R in (3.140)*, except for $\tilde{H}_r$ which is replaced by H_r.*

Proof. In the single-stage design the additional saturation block is removed, thus, we do not have s_d anymore. Following the proof of *Lemma 3.7.3*, (3.99) can be represented as (3.143) with

$$G = \begin{pmatrix} 0 & 0 & 0 & I \\ 0 & 0 & I & 0 \end{pmatrix}^{\top}, \quad H = \begin{pmatrix} -B_{\eta}^{\top} & 0 & 0 & -D_{u\eta}^{\top} K \end{pmatrix}, \tag{3.149}$$

with $\mathscr{N}_G$ the same as (3.144) and $\mathscr{N}_H$ similar to (3.146) after removing its last row and column. Next, applying the elimination lemma, the inequalities (3.148) are obtained.

The elimination lemma established that the main inequality (3.99) is equivalent to (3.148) and $\bar{R} < 0$, which is the same as the first line of (3.139), except for $\tilde{H}_r$ which is replaced by H_r in $\bar{R}$. It is clear that this difference will not affect the feasibility conditions, while it may not result in an exact χ value. $\square$

According to (3.140), since the free variable M_r only appears in matrix M, it is possible to make the second term in $R + NM^{-1}N^{\top} < 0$ arbitrary small, by choosing M_r to be large enough. Thus, the feasibility condition for the multi-stage design reduces to the feasibility condition of the single-stage design, i.e. given the feasibility of the single-stage magnitude and rate anti-windup, the multi-stage augmentation would also be feasible.

Chapter 4

Fuel Cell Application

Conventional electricity generation using fossil fuels is neither efficient nor suitable in terms of the high pollutant and greenhouse gas emissions it produces. Increasingly, fuel cells are used in a variety of applications for electricity generation [45, 11]. The ultra-low emission of fuel cells and the high cost of electricity helps fuel cells to be considered as strong candidates for the new generation of power plants. In addition, the fork-lifts with indoor 24-hour operation are another application which benefit from the facts that the fuel cells are emission free compared to combustion engines, and require much less floor space and time for recharging compared to rechargable batteries. Currently over 100000 of these fork-lifts are under operation. There are also more than 100000 small stationary fuel cells applied to telecommunication or residential applications with 1-5 kW capacity. Beside the stationary application of the fuel cells, the are increasingly considered for terrestrial transportation application as well.

In contrast to the typical heat engines that are driven by a temperature difference, the chemical potential difference is the driving force of the fuel cells. The chemical potential difference requires the fuel and air to be separated and the Reduction and Oxidation (RedOx) reactions occur as follow

$$\begin{aligned} &\text{Oxidation:} \quad CH_4 + 2H_2O \rightarrow CO_2 + 8H^+ + 8e^-, \\ &\text{Reduction:} \quad 2O_2 + 8e^- + 8H^+ \rightarrow 4H_2O. \end{aligned} \tag{4.1}$$

While, during a combustion process the reduction and oxidation happens at the same time and place as follows

$$CH_4 + 2O_2 \rightarrow CO_2 + 4H_2O. \tag{4.2}$$

The main product of the fuel cell is the clean desirable electrical energy while the thermal heat is the main product of combustion which requires conversion to mechanical energy first and then electricity in generators. The voltage available from a single fuel cell is typically less than 1V, thus, a stack of a large number of fuel cells is always of interest.

Fuel cells are classified based on their efficiency, operating temperature, and type of electrolyte. A popular class of fuel cells with efficient long term operation and fuel flexibility is Solid Oxide Fuel Cells (SOFC) which is characterized by a solid metal oxide electrolyte. SOFCs, operating at high temperature, are being used in a wide range of mobile and stationary applications taking advantage of the high quality heat byproduct, useful for reformation [1, 13].

One of the main challenges in commercialization of SOFCs is to be able to safely control the system in the presence of disturbances such as power demand variation, and/or nonlinearities such as actuator saturation [63, 36]. One of the objectives of this chapter is to ensure power following while controlling the resulting changes in the temperature profile, in transient operation of solid oxide fuel cells. This would require a high performance control technique for minimizing the temperature gradients and, thus, thermal fatigue and material damage.

For high efficiency and low degradation of the fuel cell due to thermal cycling, the fuel cell temperature should remain fairly constant during operation. This has led to increased attention to SOFC thermal control [53, 10]. To meet the demands of developing control strategies, in [28] a control oriented multi-input multi-output nonlinear thermal model of the SOFC is developed and a temperature controller is proposed. In [57], a systematic approach to the multivariable robust control of a hybrid fuel cell gas turbine plant is presented, and the transient operation of the system is studied using an empirical model. In a recent work [34], a model of the SOFC in frequency domain is developed for system control design and stability. Such models are useful to understand the fuel cell interface with remote power systems for applications such as those found in aviation, terrestrial vehicles, and naval transport industry. In [62], a dynamic states estimator is designed to track and predict the behaviors of unmeasurable states inside SOFC using stochastic filtering algorithms. In [59], dynamic programming strategies are proposed for a hybrid system to achieve an optimal schedule while minimizing fuel consumption. Reference [9] investigate the transient behavior of a 25kW SOFC and an internal combustion engine hybrid power system and apply model predictive control techniques in order to determine control parameters and set-points. Authors in [2] propose a neural network model for prediction of SOFC performance based on the Levenberg Marquardt back propagation algorithm.

The use of compressor/turbine generators with fuel cells in a hybrid format is common [63, 42]. Here, for a 5kW SOFC, we use a variable speed blower for providing oxidant and cooling purposes and assume that there exists an external reformer. The complex dynamics of the SOFC system are modeled and advanced control techniques are applied in order to achieve stable and safe operation while maintaining system performance. The objective is to maximize the usable power of a 5kW SOFC while minimizing the spatial temperature variations. We start by assuming that a controller is designed for the SOFC to primarily meet this thermal control objective. By relying on a high performance MIMO controller, proposed in [15], the non-minimum phase like behavior caused by the fan can be addressed, however, a temporary surge in blower power due to the inertia of the blade will result (overshoot in blower power demand). Large overshoots in the blower power lowers the net power of the FC available for external use. That would necessitate conservative operation of the fuel cell. In order to address this issue, we propose to limit the power sent to the blower with a fictitious saturation bound. While all actuators have a limited range of operation due to physical characteristics and constraints, the approach here creates a limit that is lower than the physical limitations, and attempts to leverage the thermal mass of the fuel cell. By preventing the blower from using too much power, more of the power of the fuel cell can be made available for external demand, while keeping a high performance controller, for tracking smaller changes or when the power demand is reduced.

As in any other physical system, actuation limitations can cause severe performance degradation (even system failure). Of course, actuators can be saturated both in terms of the size of the input generated and the rate at which the input can change, i.e., the magnitude and rate actuator saturation, respectively. In this chapter, the usable power of the fuel cell is maximized by artificially bounding the inlet flow rate, thus, avoiding the overshoots in the blower power. Anti-windup control techniques are then incorporated in order to guarantee stability and provide a satisfactory performance. The effect of AW on cathode inlet temperature, as the second actuator signal, is studied and possible rate bounds are modeled and compensated using anti-windup magnitude and rate augmentations.

The chapter outline is as follows. In *Section* 4.1, the nonlinear model of a solid oxide fuel cell in co-flow configuration is presented followed by the controller which is designed assuming ideal actuation (*Section* 4.2). The issue of maximizing usable power of a SOFC by scheduling the actuator's amplitude bounds is discussed in *Section* 4.3. In *Section* 4.5, the concept of actuator rate saturation to accommodate the maximized power with acceptable performance is discussed. *Section* 4.6 combines both magnitude and rate limitation on actuators and proposes an anti-windup design using the peak-to-peak bound minimization approach to improve the performance of the system constrained by saturation nonlinearities. Simulation results are presented in *Section* 4.6.2, evaluating the effect of the proposed AW augmentations on system performance.

4.1 Solid Oxide Fuel Cell Model

SOFC is composed of a solid electrolyte separating the two electrodes, cathode and anode which are fed by the air and fuel, respectively. As shown in Fig. 4.1, the chemical potential difference requires the fuel and air to be apart in anode and cathode, respectively. Under proper operating conditions, negatively charged oxygen ions from the cathode chamber are transferred to the anode chamber, through the separating layer of electrolyte. The release of electrons in cathode then leads to the current and formation of water.

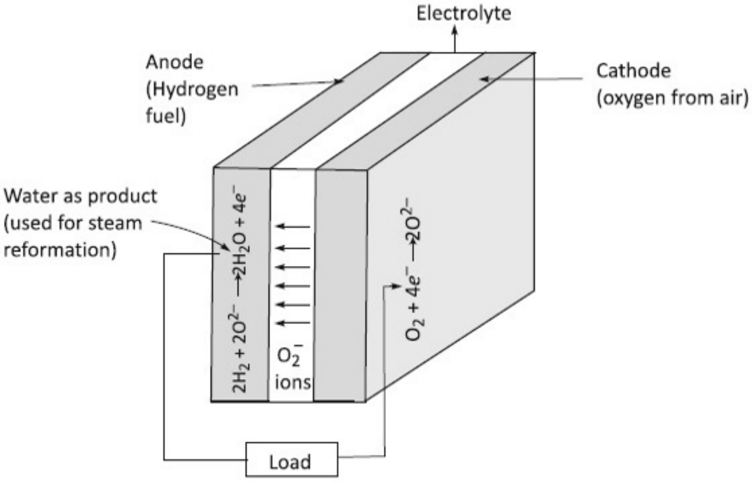

Figure 4.1: Schematic of a SOFC

The integrated nonlinear dynamic model of a SOFC system developed with multiple subsystems used here was presented in [43, 15]. For the sake of completion, some details are repeated here interested reader is not forced to consult several details. The model is a co-flow SOFC which has been evaluated with experimental data. The system is a typical planar co-flow SOFC in the 5 kW scale integrated with a variable speed blower. The model has sufficient spatial resolution (i.e along the flow channels) to capture the effects of power demand variations. A schematic of the SOFC model is shown in Fig. 4.2 representing 4 control volumes: cathode and anode gas channels, Positive-electrode Electrolyte Negative-electrode (PEN), and the top and bottom interconnecting plates which are the same due to the periodic boundary condition assumption.

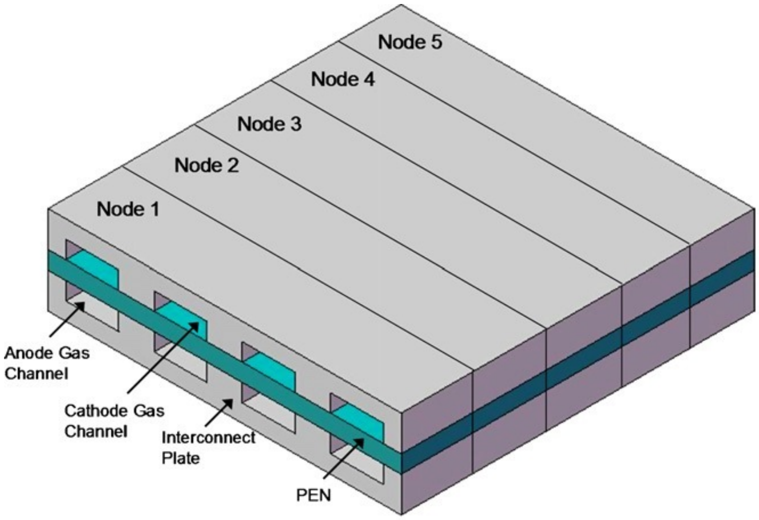

Figure 4.2: Co-flow SOFC control volumes [15].

For brevity, only the key features of the physical modeling are presented here and detailed discussions are provided in the references (e.g. in [43, 15]). Conservation of mass, energy, and species, together with the convective and conductive heat transfer, form the basis of the SOFC dynamic model. The flow throughout the system is solved for temperature, pressure, molar flow rate, and species concentration (for $CH_4, CO, CO_2, H_2, H_2O, N_2, O_2$). For gas channel control volumes, the energy conservation equation is given by

$$NC_v\frac{\mathrm{d}T}{\mathrm{d}t} = \dot{N}_{in}h_{in} - \dot{N}_{out}h_{out} + \Sigma\dot{Q}_{in} - \Sigma\dot{W}_{out}, \tag{4.3}$$

and species conservation

$$N\frac{\mathrm{d}X_i}{\mathrm{d}t} = \dot{N}_{in}X_{i,in} - \dot{N}_{out}X_{i,out} + \dot{R}_i, \tag{4.4}$$

where the exit molar flow rate $\dot{N}_{out}$ is given by

$$\dot{N}_{out} = \dot{N}_{in} + \Sigma\dot{R}_i, \tag{4.5}$$

and the description of other variables is provided in the Nomenclature. The solid-state PEN energy conservation equation for each control volume is also given by

$$\rho VC\frac{\mathrm{d}T}{\mathrm{d}t} = \Sigma\dot{Q}_{in} - \Sigma\dot{W}_{out}. \tag{4.6}$$

which is used to solve for the temperature of the solid control volumes (PEN) based on the heat transfer through the control volumes.

Convection heat transfer between each stream and the plate is modeled using Newton's law of cooling. Also, Fourier's law is used to model conduction heat transfer along the heat exchanger plate. The governing equation of the blower is the shaft torque balance presented in the state space form:

$$Jw\frac{\mathrm{d}w}{\mathrm{d}t} = P_{blower} + P_{impeller}, \tag{4.7}$$

Table 4.1: List of values for SOFC Parameters.

C	0.8	$\mathrm{kJkg^{-1}K^{-1}}$	PEN specific heat capacity
ρ	5000	$\mathrm{kgm^{-3}}$	PEN solid density
R	8.314	$\mathrm{Jmol^{-1}K^{-1}}$	Universal gas constant

where P_{blower} is the motor power supplied to the blower and $P_{impeller}$ is the loss associated with the impeller which is given by

$$P_{impeller} = \frac{1}{\eta}\frac{\gamma R T_{amb}}{\gamma - 1}[(\frac{P_{out}}{P_{amb}})^{\gamma-1/\gamma} - 1], \tag{4.8}$$

with η the blower isentropic efficiency (85%), γ the air specific heat ratio, R the universal gas constant, T_{amb} and P_{amb} the ambient temperature and pressure, respectively. The dynamic nonlinear model of a co-flow SOFC studied here is spatially discretized into 5 nodes along the flow direction (Fig. 4.2). Each node includes 4 control volumes: cathode and anode gas channels, PEN, and the interconnecting plate which adds up to 20 control volumes. A list of the 60 states of the SOFC model is given in Table 4.2, having N_2 and O_2 as anode flow species and $CH_4, CO, CO_2, H_2, H_2O, N_2$ as cathode flow species.

Table 4.2: List of states and numbers of the SOFC model.

Temperature at each of the control volumes	20
Molar fraction of cathode species at each node	10
Molar fraction of anode species at each node	30

4.2 Controller Design

One of the main challenges in transient operation of solid oxide fuel cells is achieving load following with minimum risk of damage. Power variations lead to large changes in temperature profile of the SOFC, which result in undesirable thermal fatigue and possible serious damage to the structure of the fuel cell [30]. Thermal control design aims at minimizing the spatial temperature variation throughout the SOFC, while maintaining a reasonable performance in load following.

For controller design the detailed nonlinear model of the SOFC, integrated with a variable speed blower, is first linearized around the nominal conditions and its order is reduced by removing the unobservable and uncontrollable states, and those with small Hankel singular values, along standard techniques [67]. Compared to the performance of the original nonlinear system, the linearization error observed for a 15% change in power demand is around 1°K, which is negligible compared to the operating temperature of the SOFC being around 1000°K [43]. For simplicity, we assume there is no feed-through term for u and w. The linearized reduced order plant is then given by

$$\begin{aligned} \delta\dot{x}_p &= A_p\delta x_p + B_1\delta w + B_2\delta u_p, \\ \delta z &= C_1\delta x_p, \\ \delta y &= C_2\delta x_p. \end{aligned} \tag{4.9}$$

The δ variables represent the variations from the nominal operating conditions.

The state vector $\delta x_p \in \mathbb{R}^{n_p}$ is the difference between the current state of the system from those at nominal condition, while $\delta u_p \in \mathbb{R}^{n_u}$ is the control commands that would be added to the nominal values of the input to obtain the commands to the actuators. Other variables, i.e., the measurement outputs (sensors) $\delta y \in \mathbb{R}^{n_y}$, and the performance outputs $\delta z \in \mathbb{R}^{n_z}$, similarly denote variations from the nominal conditions. The exogenous input $\delta w \in \mathbb{R}^{n_w}$ is the reference signal, representing the change in power demand.

The block diagram of the SOFC control system is shown in Fig. 4.3. Table 4.3 summarizes the input and output signals associated with the SOFC model. According to the table and figure, cathode inlet temperature and blower power are inputs to the plant u_{p1} and u_{p2}, $u_p = [u_{p1} \quad u_{p2}]^\top$, respectively. The anode outlet temperature, plate temperatures at the first, middle, and the last nodes, and the blower shaft speed are the measurement outputs, y. The electrolyte temperature at each of the five nodes are the performance outputs, z. An outer PID loop uses the power tracking signal to obtain the voltage needed and the nominal voltage is then used as the disturbance w.

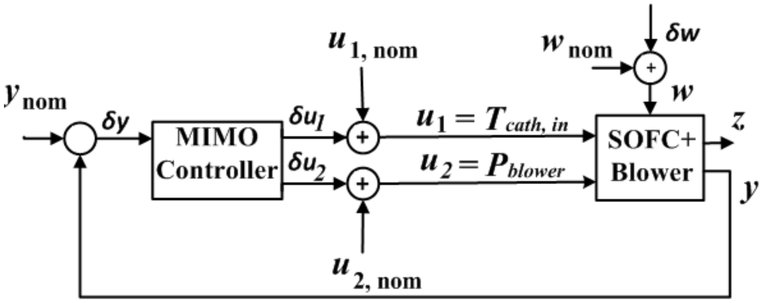

Figure 4.3: SOFC model and controller block diagram.

Table 4.3: List of input, output, and disturbance signals of the SOFC model.

Actuators	Cathode inlet temperature, $T_{cath,in}$
	Blower power, P_{blower}
Measurement outputs	Anode outlet temperature
	Plate temperature, nodes 1, 3, 5
	Blower shaft speed
Performance outputs	Electrolyte temperature, nodes 1-5
Disturbance	Fuel cell Voltage

The unconstrained Multi-Input-Multi-Output (MIMO) controller is then designed for spatial temperature control assuming ideal actuation using $\mathscr{L}_2$-gain (or $\mathscr{H}_\infty$) approach [15]. The controller aims at controlling the actuators to minimize temperature deviations from nominal conditions whenever a power demand disturbance is encountered. The stable linear controller C, with the same order as of the plant, is represented by

$$\begin{aligned}\dot{x}_c &= A_c x_c + B_{cy}\delta y, \\ \delta u &= C_c x_c + D_{cy}\delta y.\end{aligned} \tag{4.10}$$

4.3 Actuator Magnitude Limitations

The fuel cell power is prone to large variations often due to the grid (or micro-grid, for example) demand. Therefore, actuator saturation is likely, particularly for a high performance controller. Addressing the problems created by actuation saturation is one of the challenges in FC controller design. As discussed in [48], fast load following is possible under the assumption of ideal actuation. Under realistic actuation, however, power following degrades and the stability and performance are no longer guaranteed. The main actuation problems are the power needed by the blower to deliver the required cathode air flow, and the proper temperature needed at the cathode inlet. If the power demand change is large it might lead to saturation problem for the blower power. On other hand, due to the inertia of the blower, the MIMO controller designed for the integrated SOFC and the blower model can cause relatively large overshoots in the blower power and consequently limit the available net power of the FC. Since the power of the blower is provided by the fuel cell, any power not used by the blower can be added to net power supplied by the FC. While we can reduce the overshoot, by using a less aggressive controller, we would like to avoid this solution particularly when power demand is lowered and the FC temperature is prone to a significant drop. This might lead to lower efficiency in ion transport and large temperature variations.

The alternative proposed here, in order to avoid the overshoot and increase the range of power available, we use an aggressive controller and rely on artificial saturation (enforced by software) that limits the power sent to the blower. This acts on the controller as a standard saturation bound, which can result in performance degradation or instability. The next step is then to develop anti-windup protection schemes which help maintaining the stability as well as an acceptable performance for the fuel cell under such actuator saturation.

The power demand profile used in the simulations in this chapter corresponds to $\pm 15\%$ variations in power demand. Figure 4.4 shows the demand profile composed

Table 4.4: List of input, output, and disturbance signals of the SOFC model.

$T_{cath,in}$ (K)	985
P_{blower} (kW)	0.288
$T_{elec,ave}$(K)	1071.5

of a 15% decrease in the power at time $t = 11000$s, and then 30% of the nominal power increase at time $t = 12000$s. The times chosen for changes in power are far apart from each other and the start-up time, to focus on the dynamics of power set-point change. The simulation results are presented for the nominal conditions, given in Table 4.5, satisfying the temperature range often used as the most common electrolyte average temperature.

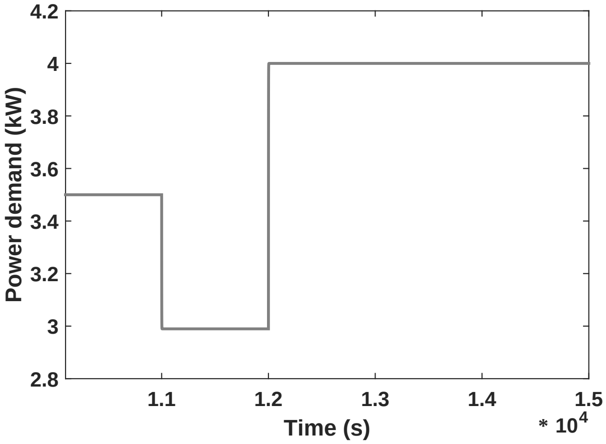

Figure 4.4: Power demand profile

4.3.1 Blower power enforced saturation

The idea of the enforced saturation, presented here, is to intentionally limit the air flow feeding the FC by putting an artificial bound on the power of the blower which is lower than the actual physical constraints. The blower power command is thus subjected to a magnitude limit m and the actuator commands would not exceed this bound. Therefore, for the second plant input (blower power), we require

$$0 \leq u_{p2} \leq u_{lim}, \tag{4.11}$$

with u_{lim} as a known positive constant, and u_{p2} to be the blower power. The inputs to the plant u_p is thus modeled as

$$u_p = \begin{bmatrix} \delta u_1 + u_{1,nom} \\ \text{sat}_m(\delta u_2 + u_{2,nom}) \end{bmatrix}. \tag{4.12}$$

When saturation is not expected to happen frequently, it is possible to design a controller for the unconstrained system, to obtain a high performance controller. Then, augmentations can be introduced to the controller, known as Anti-Windup (AW) compensation, which is responsible for maintaining the characteristics of the linear system in the absence of saturation, and guaranteeing stability together with an improved performance once saturation occurs. As a result, the small signal performance provided by the aggressive unconstrained controller is not compromised in order to achieve an acceptable large signal performance. Figure 4.5 shows the AW augmentations for the SOFC integrated model with blower power saturation. According to the figure, using the saturation block, $\delta u_2 + u_{2,nom}$ is kept within the interval $[0 \quad u_{lim}]$, thus, the actuator signal is

$$u_{p2} = \begin{array}{ll} 0 & \text{if} \quad \delta u_2 + u_{2,nom} < 0, \\ \delta u_2 + u_{2,nom} & \text{if} \quad 0 \leq \delta u_2 + u_{2,nom} \leq u_{lim}, \\ u_{lim} & \text{if} \quad \delta u_2 + u_{2,nom} > u_{lim}. \end{array} \tag{4.13}$$

The position of the saturation element is consistent with actuators with physical limits. To be more consistent with anti-windup models, this element could be moved to the left of where the $u_{2,nom}$ is added to δu_2. In that case the saturation limit would be $-u_{lim} - u_{2,nom}$ and $u_{lim} - u_{2,nom}$. The asymmetry of the bound does not cause any difficulties in the AW development since that requires only the resulting dead-zone function q

$$q = \delta u_2 + u_{2,nom} - u_{p2}, \tag{4.14}$$

to have the same sign as the corresponding δu_2, which holds as long as $u_{lim} - u_{2,nom} > 0$. As a result, the anti-windup gains would be the same in either arrangement. Figure 4.5 shows how this anti-windup augmentation would be implemented, and we use the same setup for our simulations.

4.3.2 Anti-windup design with magnitude bound on blower power

As depicted in Fig. 4.5, the objective here is to design an anti-windup augmentation that introduces suitable additive modification signals $v_1 \in R^{n_c}$ and $v_2 \in R^{n_{u2}}$ and

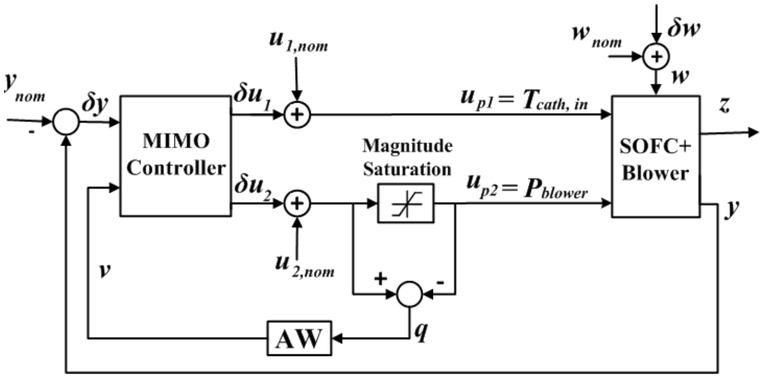

Figure 4.5: SOFC model with blower power actuator saturation

augment the unconstrained compensator (4.10) as

$$\begin{aligned}\dot{x}_c &= A_c x_c + B_{cy}\delta y + v_1, \\ \delta u &= C_c x_c + D_{cy}\delta y + \begin{bmatrix} 0 \\ v_2 \end{bmatrix}.\end{aligned} \tag{4.15}$$

These modifications should make the closed-loop system internally stable with a guaranteed input-output performance level in the presence of saturation nonlinearities in the control loop. In Fig. 4.5, since only the second output of the controller (the blower power actuator) is subject to saturation, the anti-windup term v_2 is added only to the second row of the input vector u, which corresponds to the blower power as From (4.12),

$$\dot{x}_p = A_p x_p + B_1 w + [B_{21} \quad B_{22}] \begin{bmatrix} u_{p1} \\ u_{p2} - q \end{bmatrix}. \tag{4.16}$$

The static anti-windup block containing matrix gain

$$\mathrm{AW}_{(}q) = -\Lambda q, \tag{4.17}$$

is then applied to the dead-zone function defined in(6.52).

Following standard techniques in e.g. [18, 50], and recalling the fact that here only one of the actuators is subject to saturation, it is straight forward to build the augmented system with state vector $x = [\delta x_p^\top \quad x_c^\top]^\top \in R^n$ and w and q as input signals. Given the linearized SOFC state-space model (4.9) and the unconstrained linear controller (4.10), the closed-loop system with magnitude anti-windup gains can be written as

$$\begin{aligned} \dot{x} &= Ax + B_w \delta w + (B_q - B_\eta \Lambda) q, \\ \delta z &= C_z x + D_{zw} \delta w + (D_{zq} - D_{z\eta} \Lambda) q, \\ \delta u &= C_u x + D_{uw} \delta w + (D_{uq} - D_{u\eta} \Lambda) q, \end{aligned} \tag{4.18}$$

with system matrices given by

$$\left[\begin{array}{c} A \\ \hline C_z \\ \hline C_u \end{array}\right] = \left[\begin{array}{cc} A_p + B_2 D_{cy} C_2 & B_2 C_c \\ B_{cy} C_2 & A_c \\ \hline C_1 + D_{12} D_{cy} c_2 & D_{12} C_c \\ \hline D_{cy} C_2 & C_c \end{array}\right], \tag{4.19}$$

$$\left[\begin{array}{c} B_w \\ \hline D_{zw} \\ \hline D_{uw} \end{array}\right] = \left[\begin{array}{c} B_2 D_{uw} + B_1 \\ B_{cy} D_{21} + B_{cw} \\ \hline D_{11} + D_{12} D_{uw} \\ \hline D_{cy} D_{21} \end{array}\right],$$

and

$$\left[\begin{array}{c|c} B_q & B_\eta \\ \hline D_{zq} & D_{z\eta} \end{array}\right] = \left[\begin{array}{c|c} -B_{22} & B_{22}[0 \quad I] \\ 0 & [I \quad 0] \\ \hline -D_{122} & D_{122}[0 \quad I] \end{array}\right], \tag{4.20}$$

$$\left[\begin{array}{c} D_{uq} \\ \hline D_{u\eta} \end{array}\right] = \left[\begin{array}{c} 0 \\ 0 \\ \hline [0 \quad 0; 0 \quad I] \end{array}\right],$$

where B_{22} and D_{122} are the second columns of B_2 and D_{12}, and D_{cy2} is the second row of D_{cy}. The system matrices are slightly different from the general magnitude AW design due to the fact that here only a subset of input signals are subject to saturation (only the blower power, u_2, and not the cathode inlet temperature, u_1).

In order to guarantee the stability of the closed-loop system (4.18) and establish a performance bound for the AW design, an upper bound for the $\mathscr{L}_2$ (or Energy) gain γ, from the disturbance signal w to the performance output z, is minimized and the stabilizing AW gain Λ is obtained.

Algorithm. [Magnitude AW for MIMO systems with partially bounded actuators: Energy gain approach] Consider the plant and the controller introduced in (4.9), (4.10), and (4.12), as well as the magnitude limit m. Given any solution to the optimization problem

$$\min_{Q,M,X,\gamma} \quad \gamma \tag{4.21}$$

subject to the Linear Matrix Inequality constraints

$$\begin{pmatrix} QA^\top + AQ & * & * & * \\ B_w^\top & -\gamma I & * & * \\ C_z Q & D_{zw} & -\gamma I & * \\ \Phi_{4,1} & D_{uw2} & M_m D_{zq}^\top - X^\top D_{z\eta}^\top & \Phi_{4,4} \end{pmatrix} < 0, \tag{4.22}$$

$$Q > 0, \tag{4.23}$$

where

$$
\begin{aligned}
M &= W^{-1}, \quad X_{=}\Lambda M, && (4.24)\\
\Phi_{4,1} &= MB_q^\top - X^\top B_\eta^\top + C_{u2}Q,\\
\Phi_{4,4} &= -2M + D_{uq2}M + MD_{uq2}^\top - D_{u\eta 2}X - X^\top D_{u\eta}^\top,
\end{aligned}
$$

with the AW gain,

$$
\Lambda = XM^{-1}, \tag{4.25}
$$

the augmented closed loop system (4.18), has a guaranteed $\mathscr{L}_2$ gain of γ from w to z.

Inequality (4.22) provides the stability condition for the saturated system with anti-windup gain Λ using the standard Lyapunov stability approach. The minimization is constrained by a Linear Matrix Inequality (LMI) ensuring the stability and performance bound γ (details omitted due to space limitation). While the algorithm presented is to bound the energy of the performance output (by a fix multiple of the energy of the reference input), other techniques that bound the peak norm (i.e., peak-to-peak or energy-to-peak) are straightforward and can be implemented in a similar fashion with ease [50]. Indeed, we use minimization of the upper bound for peak-to-peak gain.

Setting aside a few percentage of power for the balance of plant (BoP) and other parasitic losses, the net power of the fuel cell available for external use is the difference between the total power and the power required for the blower

$$P_{net} = P_{FC} - P_{blower}. \tag{4.26}$$

4.4 Simulation Result

4.4.1 Blower power saturation

In general, in the process of fuel cell modeling, there are two types of the constraints which need to be taken care of: the actuator constraints and the state constraints. The actuator constraints (studied here) are the possible bounds on the FC model inputs, i.e. the cathode inlet temperature and the blower power. On the other hand, there are state constraints on fuel cell electrolyte temperature. Consistent with literature, the average temperature of 1070K is assumed as an acceptable temperature for the fuel cell electrolyte. A higher cathode inlet temperature increases the average electrolyte temperature, while an increase in the blower power helps in cooling down the electrolyte. Therefore, it is possible to maintain $T_{elec,ave}$ approximately constant by increasing $T_{cath,in}$ and P_{blower} at the same time.

In the rest of this section, the simulation results are presented for two sets of the nominal conditions, given in Table 4.5, satisfying the constraint on the electrolyte average temperature. In set 1, nominal values used in [15] are considered, while in set 2, both the cathode inlet temperature and the blower power are increased such that the average electrolyte temperature remains approximately unchanged.

Table 4.5: Nominal conditions.

	$T_{cath,in}$ (K)	P_{blower} (kW)	$T_{elec,ave}$(K)
Set 1	965	0.188	1072.5
Set 2	985	0.288	1071.5

In terms of actuator constraints, as discussed in Sec. 4.3.1, the idea is to apply an intentional limit to the blower power in order to make more power available to use. The limit is applied by adding a saturation element to the blower power. In order to minimize the effects of adding this intentional saturation element, AW gains designed in Sec. 4.3.1 are used, which maintains the overall system stability and recovers the performance of the unconstrained system. The study is performed for both sets of nominal conditions presented in Table. 4.5 in the following sections.

Nominal condition 1

Figures 4.6 and 4.7 show the variation of blower and fuel cell power with respect to time, respectively. According to the Fig. 4.7, the power of the fuel cell undergoes an overshoot for a short period of time between seconds 12000 and 12140. During this period, the power of the fuel cell increases by almost %2.5 to a peak value of 4.443 kW. The idea is to eliminate this excess power by putting a limit on the blower power. Therefore, as shown by Fig. 4.6, the steady-state value of the blower power, 0.355 kW, is selected and used as the saturation limit.

Since the saturation element added only removes the overshoot and is in fact active for a short period of time, the temperature profile of the system is not expected to change significantly. Fig. 4.8 shows the profile of the anode outlet temperature before and after applying the blower power saturation. As expected, limiting the blower power with $u_{\text{lim}} = 0.355$ kW, has not changed the temperature profile more than 2 degrees Kelvin, while saving %2.5 of power for external use.

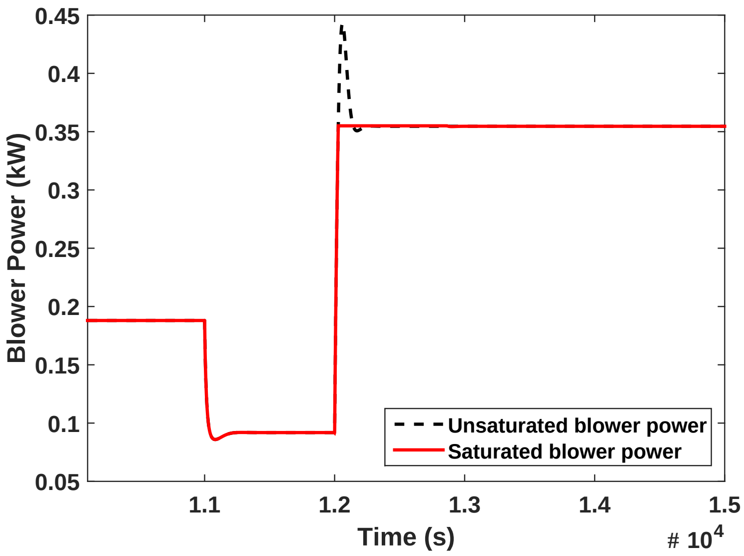

Figure 4.6: Blower power for nominal condition 1 and $u_{lim} = 0.355\text{kW}$.

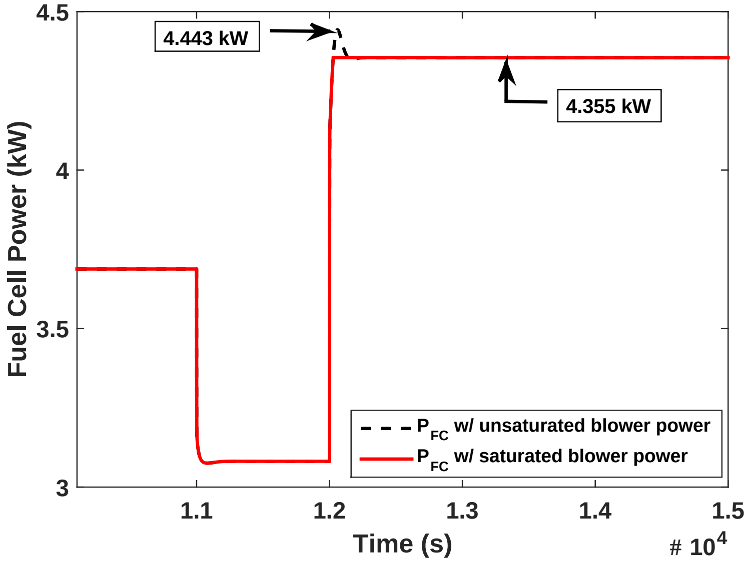

Figure 4.7: Fuel cell power for nominal condition 1 and $u_{lim} = 0.355\text{kW}$.

One way to increase the percentage of the saved power is to decrease the blower power saturation limit. In Figures 4.9, the limit of 0.31 kW is selected for the

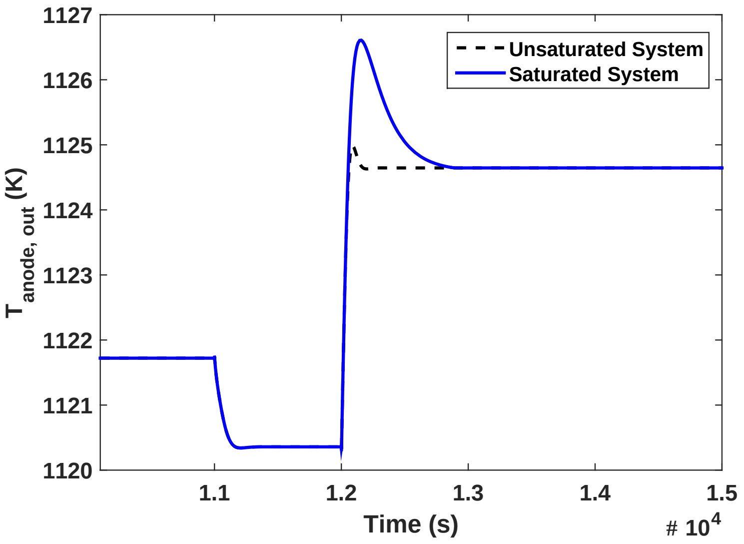

Figure 4.8: Effect of AW on system performance for nominal condition 1 and $u_{\text{lim}} = 0.355\text{kW}$.

blower power saturation element. According to Fig. 4.10, the fuel cell power has now been saved by almost %4.1.

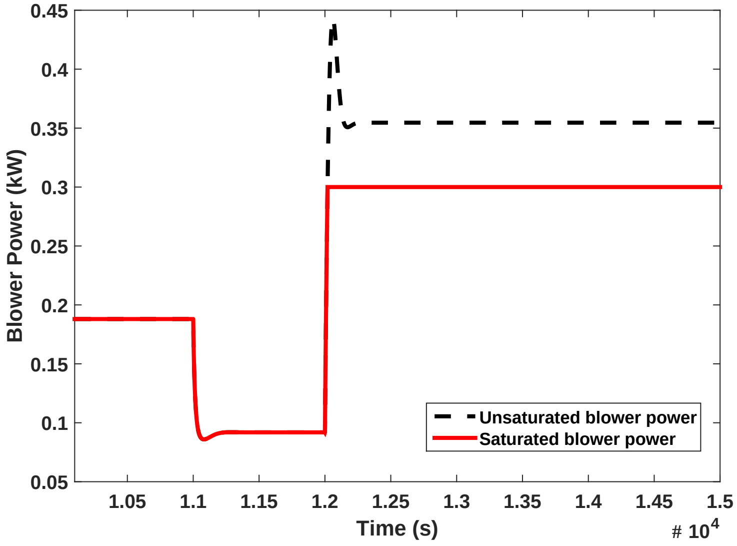

Figure 4.9: Blower power for nominal condition 1 and $u_{\text{lim}} = 0.31$.

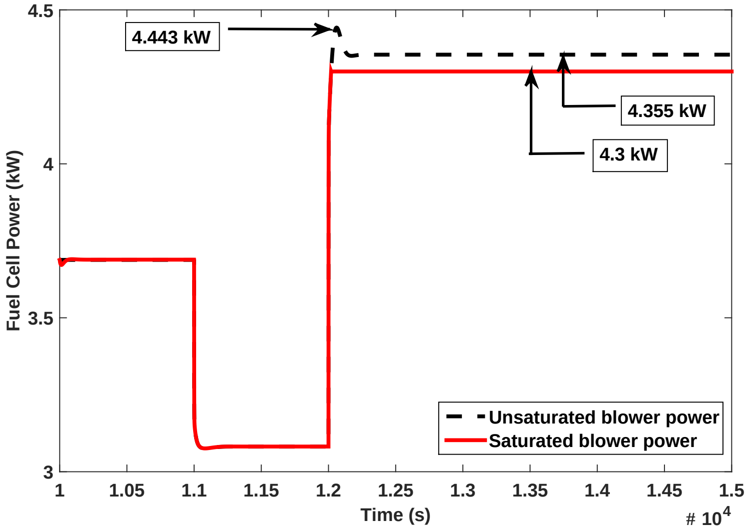

Figure 4.10: Fuel cell power for nominal condition 1 and $u_{\text{lim}} = 0.31$.

As shown by Fig. 4.11, the intentional saturation of the blower power increases the anode outlet temperature by more than 8 degrees Kelvin and there is no guarantee for the stability of the system. However, as shown in the figure, the AW design presented in Sec. 4.3.2, reduces this error to about 2 degrees Kelvin and guarantees system stability.

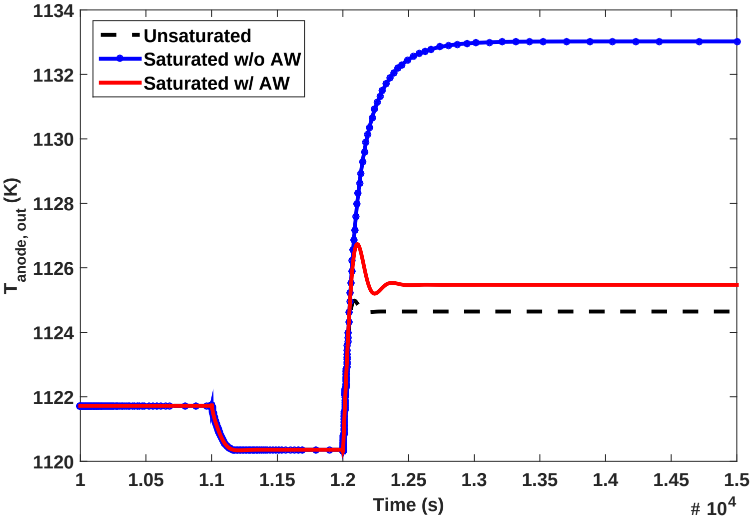

Figure 4.11: Effect of AW on system performance for nominal condition 1 and $u_{\text{lim}} = 0.31$.

Nominal condition 2

In the second nominal condition, the cathode inlet temperature and blower power are increased while maintaining the standard electrolyte average temperature. According to Fig. 4.13, the power of the fuel cell undergoes an overshoot for a short period of time between seconds 12000 and 12200. During this period the power of the fuel cell increases by almost %7 to a peak value of 4.85 kW. The excess power is removed by choosing the steady-state value of the blower power, 0.62 kW (Fig. 4.12), as the blower power saturation limit.

Figure 4.13 shows the profile of the anode outlet temperature before and after applying the blower power saturation. As expected, limiting the blower power with $u_{\text{lim}} = 0.62$ kW, has not changed the temperature profile more than 2 degrees Kelvin, while saving %7 of power for external use. Even for the minor changes in

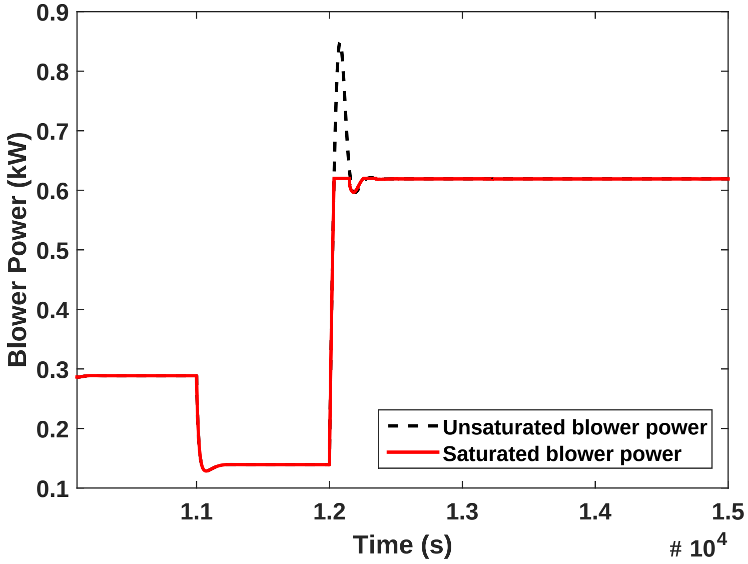

Figure 4.12: Blower power for nominal condition 2 and $u_{lim} = 0.62$kW.

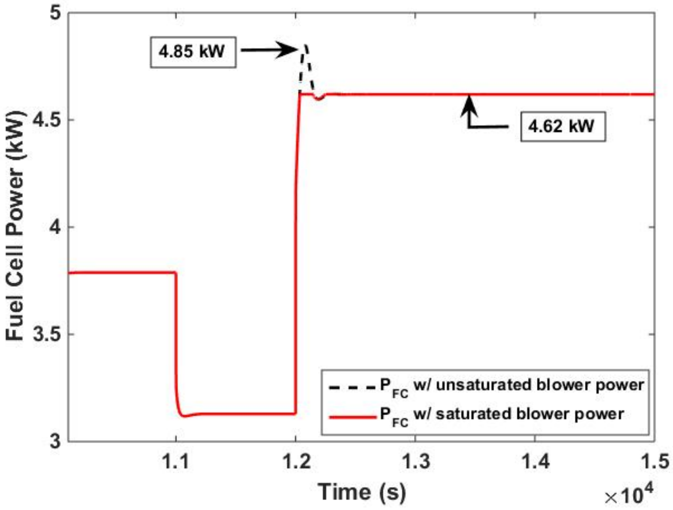

Figure 4.13: Fuel cell power for nominal condition 2 and $u_{lim} = 0.62$kW.

the temperature profile, AW design presented in Sec. 4.3.2, successfully addresses the issue and recovers the performance of the unconstrained system.

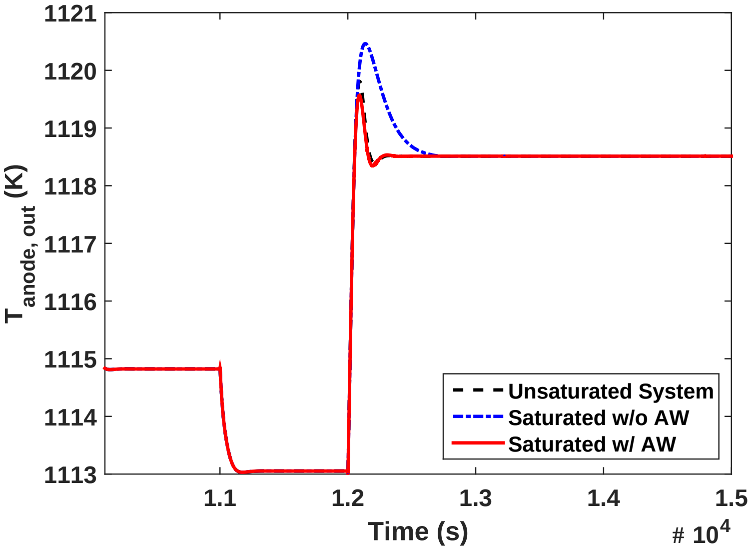

Figure 4.14: Effect of AW on system performance for nominal condition 2 and $u_{\text{lim}} = 0.62\text{kW}$.

Now that the AW design performance looks promising, there is the possibility to decrease the blower power saturation limit to even lower than its steady-state value, in order to save more power with minimal temperature issues. In Fig. 4.15, the limit of 0.31 kW is selected for the blower power saturation element. According to Fig. 4.16, the fuel cell power has been saved by almost %15 and is available for usage.

As shown by Fig. 4.17, without applying the AW results, the new saturation limits increases the anode outlet temperature by more than 25 degrees Kelvin. While, using the AW design, the error reduces to around 2 degrees Kelvin which is not significant. Therefore, the idea of limiting the blower power has saved %15 of the fuel cell power with minimal practical problems.

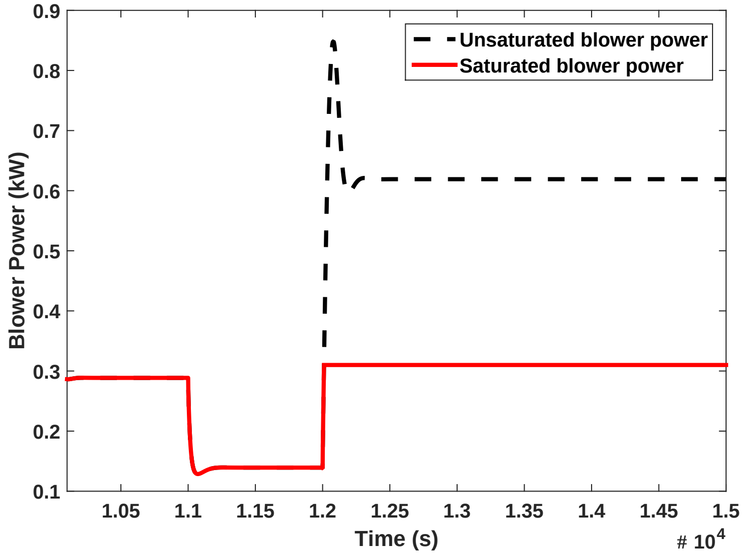

Figure 4.15: Blower power for nominal condition 2.

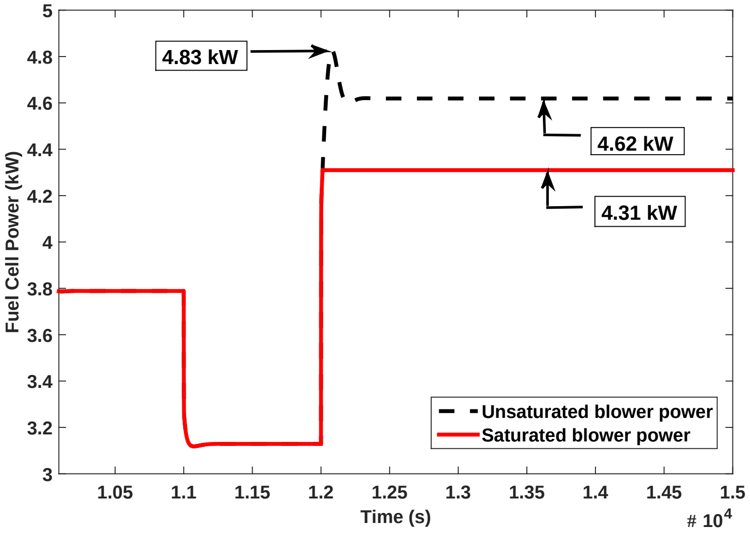

Figure 4.16: Fuel cell power for nominal condition 2.

While the blower power for the nominal condition is 0.288kW (from Table 4.5), increasing the overall power level requires higher air flow rates and thus higher blower power. Furthermore, the overshoot of the blower should also be taken into

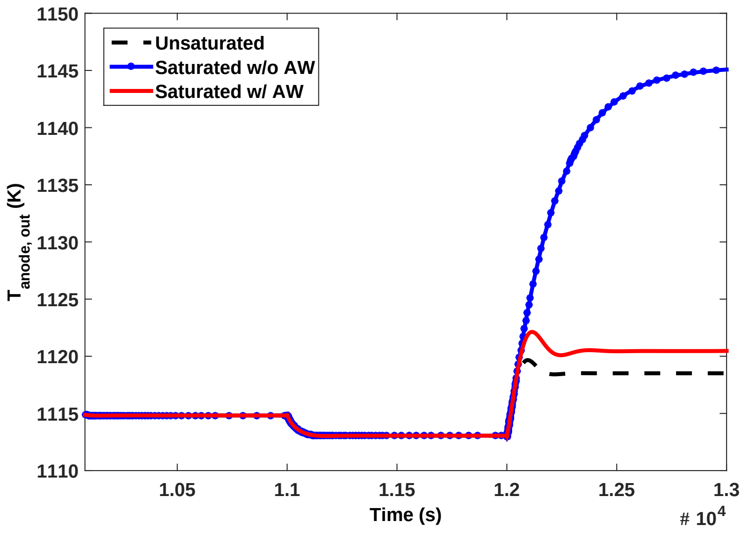

Figure 4.17: Effect of AW on system performance for nominal condition 2.

account. As shown in Fig. 4.18, the peak blower power (for both overshoot and steady operation at higher power levels) reaches to close to 1kW. Therefore, the maximum net power which can be achieved form the fuel cell is limited to 4kW. Assuming a $\pm 15\%$ variation in the nominal power demand, the nominal value of the fuel cell net power should then be approximately 3.5kW, in order to respect the 5kW upper bound of the fuel cell capacity, i.e.

$$P_{net,max} = 3.5\text{kW}. \tag{4.27}$$

In order to increase the maximum net power available by the fuel cell (4.27), the idea of the enforced saturation (bounding the blower power intentionally) is applied, and AW techniques are used to ensure stability and performance. The steady-state value of the blower power (0.66kW) could be selected as the magnitude bound in order to avoid the excess power in overshoot. Due to the thermal mass of the

FC, cutting the power for the short duration of the overshoot would not change the temperature profiles significantly, while a %7 increase in the net power could be achieved.

A lower power bound results in more power saving, particularly if the higher power demand is not permanent and a decrease in tracking profile is expected. Therefore, in Fig. 4.18, the limit of 0.4kW is selected for the blower power saturation element (Recall the nominal value is 0.288kW).

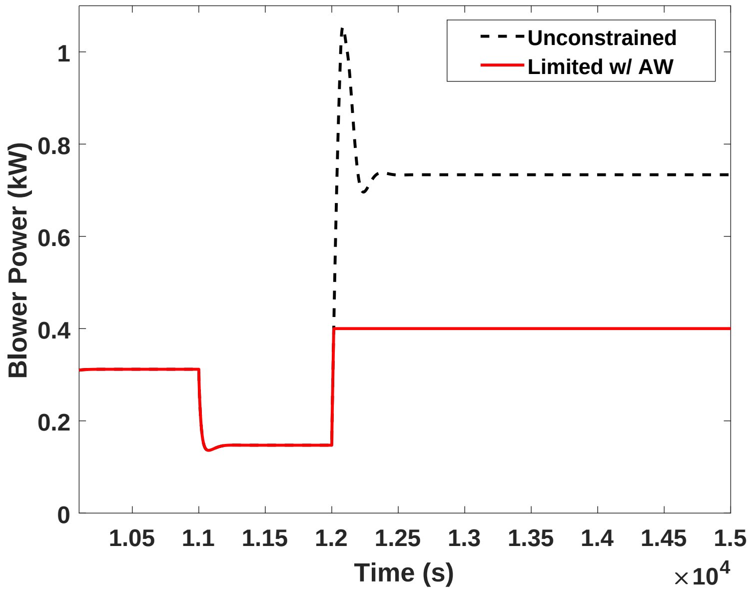

Figure 4.18: Blower power with enforced saturation level of 0.4kW.

Figure 4.19 shows the total power of the fuel cell with or without limiting the blower power. Avoidance of the overshoot shown in Fig. 4.19 allows the nominal power of the fuel cell to be at 0.57kW higher level. Adding this value to the maximum nominal net power of the FC (4.27), gives

$$P_{net,max} = 4.07\text{kW}, \tag{4.28}$$

having $u_{lim} = 0.4\text{kW}$ on P_{blower}.

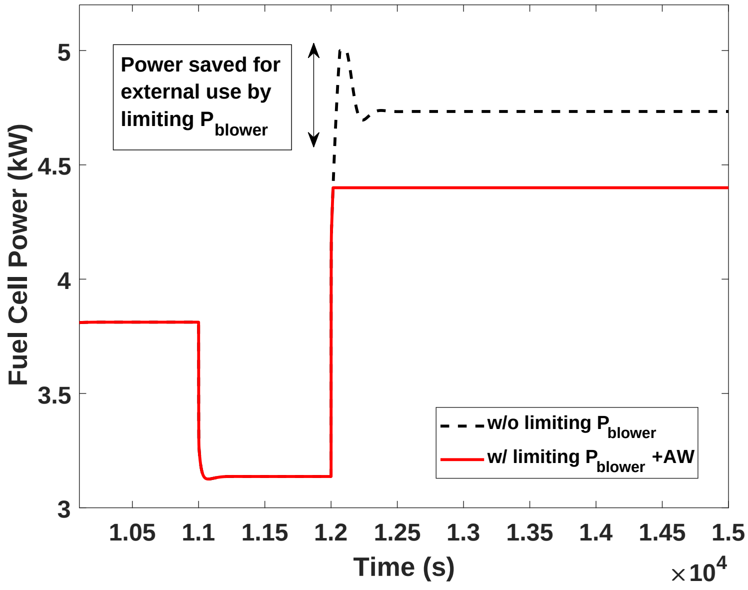

Figure 4.19: Fuel cell power with enforced saturation level of 0.4kW on blower power and nominal power demand of 3.5kW.

This level implies a 16% increase in the FC available net power. Therefore, by putting an aggressive limit on the blower power and taking advantage of the AW techniques, the same SOFC can be used for up to 16% higher power demands.

Without anti-windup, as shown in Fig. 4.20, the 16% additional power made available is at the cost of a large temperature increase while the signal is saturated. By limiting the blower power, not enough air is sent through, causing a large temperature rise along the cell, especially at the outlet. These changes in the temperature profile can have negative impact on the FC and may lead to degradation and thermal fatigue. However, taking advantage of the proposed AW techniques, the error can be reduced to the negligible amount of less than 2 degrees Kelvin.

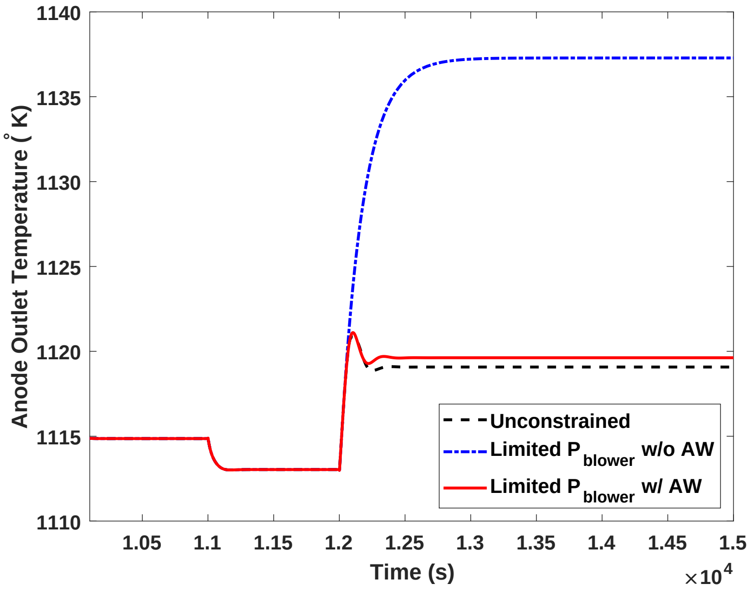

Figure 4.20: Anode outlet temperature.

Figure 4.21 shows the variation of the cathode inlet temperature, the other actuator of the fuel cell system, when it is not subject to any saturation constraint. This figure shows that in order to address the blower power saturation, and reduce the error in the outlet temperature, the augmented controller avoids further heating up of the inlet using the other actuator signal ($T_{cath,in}$). As shown in [15], in co-flow FC, without saturation constraint, both the air flow rate and cathode inlet temperature are increased in response to higher power demand. The elevated airflow rate is aimed at reducing the average temperature while the higher inlet temperature ameliorates potential thermal gradients along the cell.

In order to accommodate the instantaneous drop in inlet temperature observed in Fig. 4.21, an actuator with high rate of change is required. However, in the absence of ideal actuation assumption, the rate at which $T_{cath,in}$ can change is limited by the mechanism used (e.g., heat exchanger, mixing chamber). Under operational conditions, this may lead to actuator rate saturation, causing severe performance degradation. The rate anti-windup design introduced in the next section is used as the remedy, since an artificial rate bound can address this sudden drop in cathode inlet temperature, thus, avoiding large temperature gradients. The objective is to extend anti-windup protection schemes which help maintaining the stability as well as an acceptable performance for the fuel cell under actuator both magnitude and rate saturations.

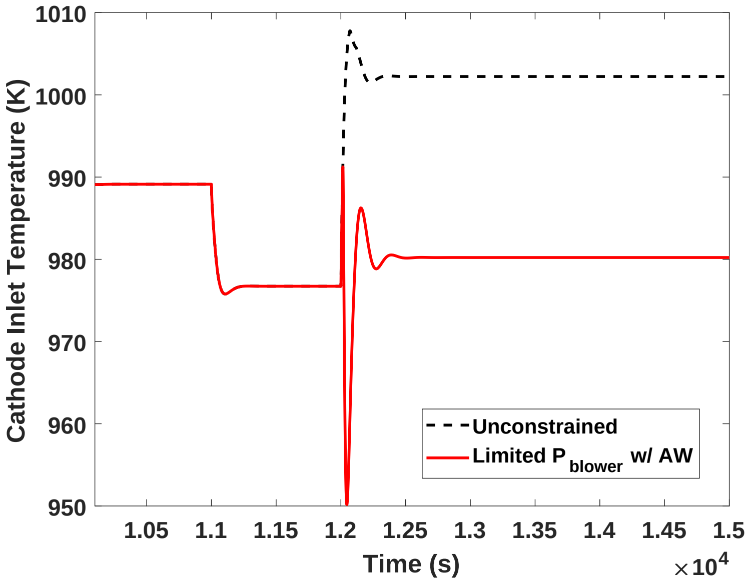

Figure 4.21: Cathode inlet temperature with and without enforced saturation.

4.5 Actuator Rate Saturation

The inlet air temperature is controlled by bypassing the air through a heat exchanger or a mixing chamber with possibly slow dynamics. As the SOFC is a high temperature fuel cell, there might not be a real magnitude bound on the temperature control signal for the cathode inlet. However, the rate at which this temperature can change, in order to satisfy the control commands, can be limited by the heat exchange mechanism or transport delays.

4.5.1 Rate Model

In order to study the effects of actuator rate saturation on the fuel cell performance, we first need to have access to the rate signal (not typically available) and apply rate limits. One common approach to model the rate signal is to insert a first-order filter with gain K in the forward loop connecting the controller's output to the plant's input. As shown in Fig. 4.22, a first order circuit with a saturation element is added before the actuator. As a result, the actuator signal is guaranteed to be rate bounded as was discussed earlier.

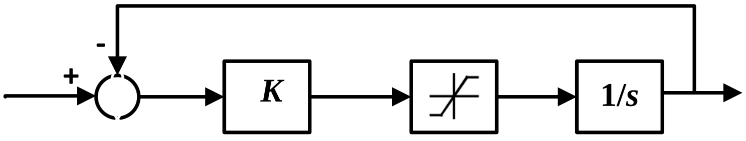

Figure 4.22: Rate saturation model

The gain K needs to be selected large enough in order not to affect the dynamics of the original system. Figures 4.23 and 4.24 illustrate the effect of rate model with different K values on inlet and outlet temperatures, respectively. In fact, gain K controls the delay in system response as this is a first-order filter that may influence the FC behavior. Higher K corresponds to smaller delay and thus faster response compared to the time constants of the original system. For relatively small values of gain K, as shown in Fig. 4.23, the delay is observed in the inlet of the fuel cell. For $K \geq 0.1$ temperature profiles throughout the cell remain unchanged after adding the rate model. Therefore, for the rest of the simulations in this section $K = 0.1$ is selected for the gain of the rate model. The signals are available for the anti-windup loop since the loop in Fig. 4.22 ia a part of the compensator.

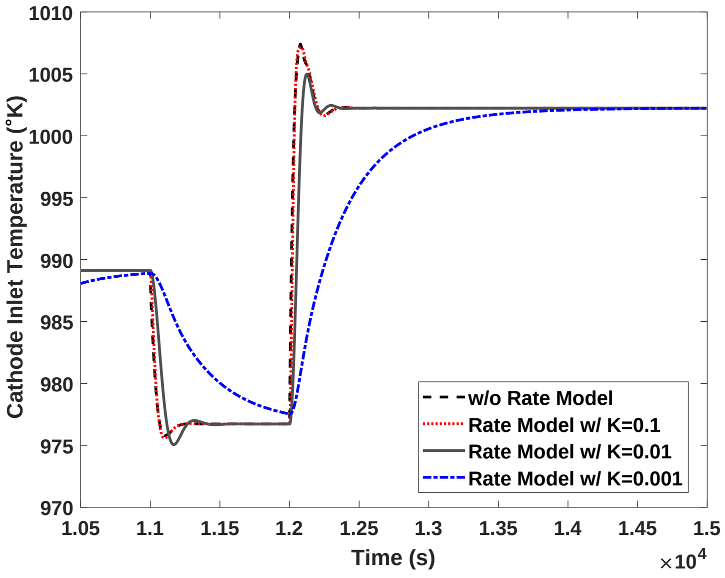

Figure 4.23: Effect of different K values on cathode inlet temperature

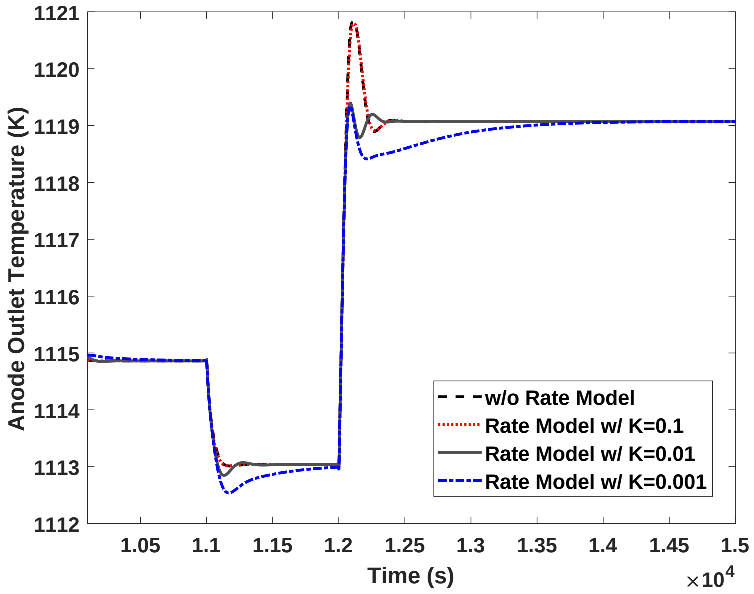

Figure 4.24: Effect of different K values on anode outlet temperature

4.5.2 Cathode Inlet Temperature Rate Saturation

Figure 4.25 shows the block diagram of the SOFC control system with the first-order model added, having the first actuator subject to rate saturation. For the first plant input ($T_{cath,in}$), we require

$$|\dot{u}_{p_1}| \leq \mathsf{r}, \tag{4.29}$$

with r as a known positive constant with unit °K/s. This model guarantees the cathode inlet temperature signal to be rate bounded.

Figure 4.26 shows the effect of different rate saturation bounds on the profile of the cathode inlet temperature. When an increase in power demand is requested, the unconstrained controller increases both inlet temperature and the airflow rate in

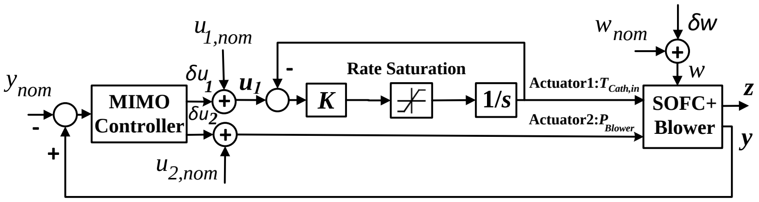

Figure 4.25: SOFC model with cathode inlet temperature rate saturation

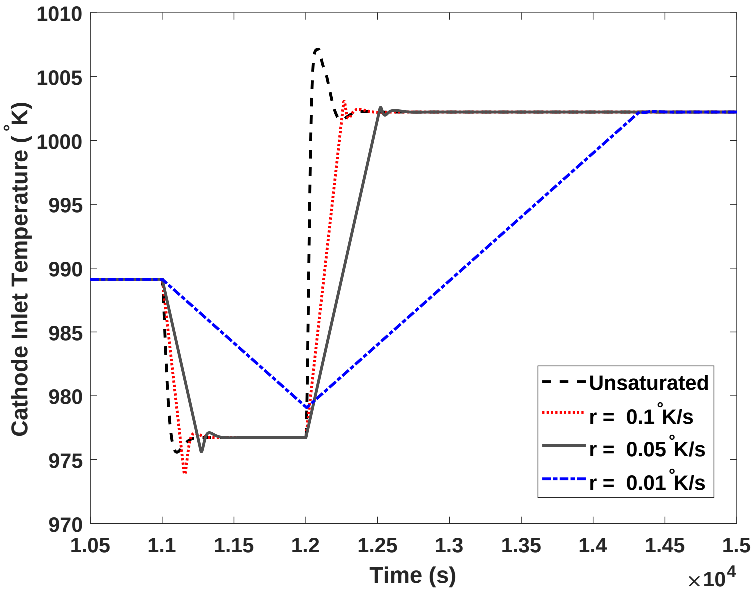

Figure 4.26: Effect of rate saturation on cathode inlet temperature

order to minimize the spatial temperature gradients along the cell (dashed curve). However, as shown in the figure, a limited rate of change of $T_{cath,in}$ causes a lower slope in the inlet temperature rise.

Figure 4.27 shows the effect of different rate saturation levels on the profile of the anode outlet flow temperature. As the rate bound gets tighter, inlet temperature rises slower thus, a drop in temperature at the outlet is expected. Compared to the cathode inlet temperature (Fig. 4.26), the anode outlet temperature, Fig. 4.27,

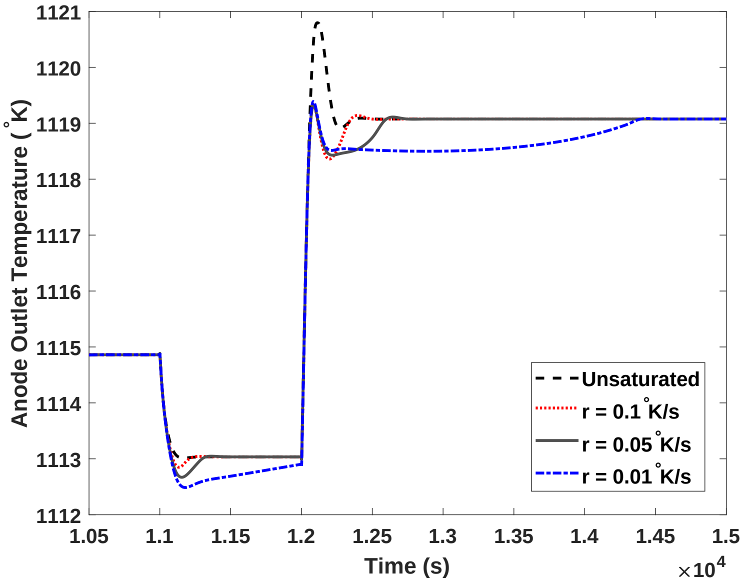

Figure 4.27: Effect of rate saturation on anode outlet temperature

shows less sensitivity to rate saturation since it is located far from the point of restriction and the effects of the bound become less profound toward the end of the cell. The decrease in the inlet temperature and the increase in the outlet temperature may causes a minor increase in spatial temperature gradients along the cell from nominal conditions, particularly at the nodes near the inlet. To address this we add a rate limited anti-windup with details discussed in Section 6.

4.6 Actuator Magnitude and Rate Saturation

The block diagram of the fuel cell control system with a magnitude bound on blower power actuator and rate bound on cathode inlet temperature is shown in Fig. 4.28 which is a combination of Figures 4.5 and 4.25.

Rate bounded cathode inlet temperature and magnitude bounded blower power are modeled as

$$\begin{aligned} \dot{x}_I &= \mathrm{sat}_{\mathsf{r}}(K(u_1 - x_I)), \qquad (4.30) \\ u_{p_2} &= \mathrm{sat}_{\mathsf{m}}(u_2), \end{aligned}$$

where $K = \mathrm{diag}(K_1, \cdots, K_{n_{u_1}}) \in \mathbb{R}^{n_{u_1} \times n_{u_1}}$ and x_I is the integrator's state.

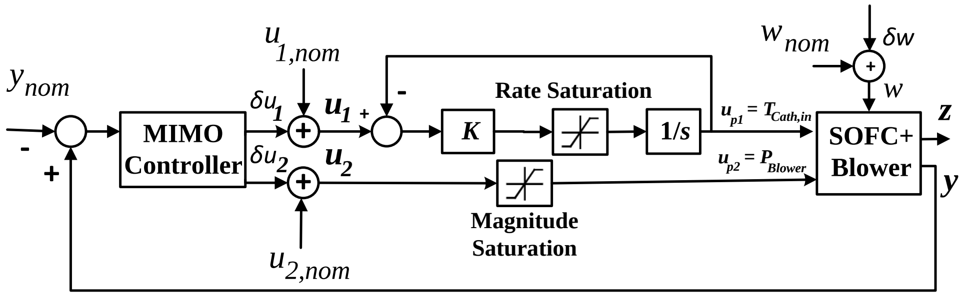

Figure 4.28: SOFC model with blower power magnitude and cathode inlet temperature rate saturation

In order to minimize the negative effects of rate saturation on fuel cell performance and guarantee the system stability, we rely on anti-windup design for both magnitude and rate bounded actuators.

4.6.1 Anti-windup Design

The objective here is to design an anti-windup augmentation $v = [v_1^\top \quad v_2^\top]^\top$ that introduces suitable additive modification signals $v_1 \in \mathbb{R}^{n_c}$ and $v_2 \in \mathbb{R}^{n_{u1}}$ to the unconstrained controller (4.10). According to Fig. 4.29, since the first output of the controller ($T_{cath,in}$) is subject to rate saturation, and the second output (P_{blower}) is magnitude bounded, the anti-windup term v_2 is added to the entire input vector u (see (4.15) for comparison). Therefore,

$$\begin{aligned} \dot{x}_c &= A_c x_c + B_{cy} y + v_1, \\ u &= C_c x_c + D_{cy} y + v_2. \end{aligned} \tag{4.31}$$

The static anti-windup block containing matrix gains

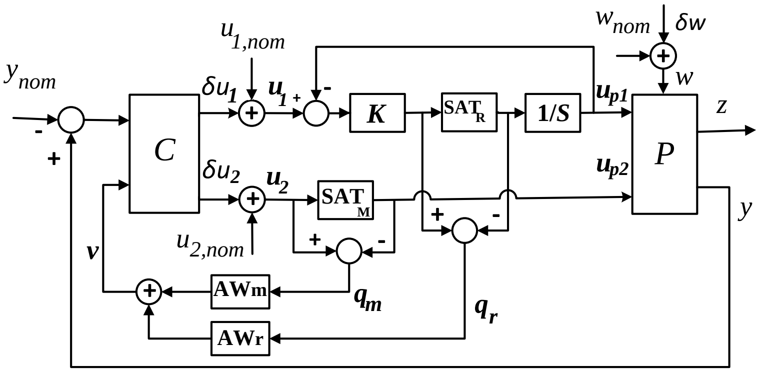

Figure 4.29: Magnitude and rate anti-windup design schematic

$$\begin{aligned} \mathrm{AW}_r(q) &= -\Lambda_r q_r, \\ \mathrm{AW}_m(q) &= -\Lambda_m q_m, \\ \mathrm{AW}(q) &= -\Lambda_m q_m - \Lambda_r q_r, \end{aligned} \tag{4.32}$$

is applied to the dead-zone function $q = \eta - \mathrm{sat}_r(\eta) = \eta - \dot{x}_I$, and the signal x_I is defined as a new state variable with dynamics

$$\dot{x}_I = K(u_1 - x_I) - q_r, \tag{4.33}$$

in which the signal u_1 is the first row of u defined in (4.31). The augmented closed-loop system with state vector $x = [\delta x_p^\top \quad x_c^\top \quad x_I^\top]^\top$, and w and q as input signals in then presented as

$$
\begin{aligned}
\dot{x} &= Ax + B_w \delta w + (B_{qm} - B_\eta \Lambda_m) q_m + (B_{qr} - B_\eta \Lambda_r) q_r, \\
\delta z &= C_z x, \\
\delta u_p &= C_u x + D_{uw} \delta w + (D_{uq} - D_{u\eta} \Lambda_m) q_m \\
&\quad + (D_{uq} - D_{u\eta} \Lambda_r) q_r,
\end{aligned}
\tag{4.34}
$$

with system matrices given by

$$
\left[\begin{array}{c} A \\ \hline C_u \\ \hline C_z \end{array}\right] = \left[\begin{array}{ccc} A_p + B_{22} D_{cy2} C_2 & B_{22} C_{c2} & B_{21} \\ B_{cy} C_2 & A_c & 0 \\ K D_{cy1} C_2 & K C_{c1} & -K \\ \hline D_{cy} C_2 & C_c & 0 \\ \hline C_1 & 0 & 0 \end{array}\right], \tag{4.35}
$$

$$
\left[\begin{array}{c|c|c} B_w & B_q & B_\eta \\ \hline D_{uw} & D_{uq} & D_{u\eta} \end{array}\right] = \left[\begin{array}{c|cc|cc} B_{22} D_{cy2} D_{21} + B_1 & -B_{22} & 0 & [0 \quad 1] & 0 \\ B_{cy} D_{21} & 0 & 0 & [I_{n_c} \quad 0] & [I_{n_c} \quad 0] \\ K D_{cy1} D_{21} & 0 & -I & 0 & K[0 \quad 1] \\ \hline 0 & \multicolumn{2}{c|}{0} & 0 & [0 \quad 1] \\ 0 & \multicolumn{2}{c|}{0} & [0 \quad 1] & 0 \end{array}\right].
$$

Here, we assume that a possibly conservative estimate of the disturbance signal $w(t)$ is known. Therefore, the peak-to-peak approach is applied to the current fuel cell saturation problem.

Algorithm. [Magnitude and Rate AW for MIMO systems with partially bounded actuators: Peak-to-peak approach] Assume that this system is only exposed to peak-bounded disturbances with known upper bound $w_{\max} \in \mathbb{R}$, i.e., $w^\top(t)w(t) \leq w_{\max}^2$. Given the saturation model (4.30) with the magnitude and rate limits m and r, let us assume that for a given $0 < \alpha < \frac{|\mathrm{Re}(\lambda_{min}(A))|}{2}$, there exists a solution for

$$\min_{Q,M_m,M_r,X_m,X_r,Y_m,Y_r,\gamma^2} \quad \gamma^2 \tag{4.36}$$

subject to

$$\begin{pmatrix} QA^\top + AQ + Q\alpha & * & * & * \\ B_w^\top & -\alpha I & * & * \\ \bar{\Phi}_{3,1} & 0 & -2M_m & * \\ \bar{\Phi}_{4,1} & KD_{uw1} & \bar{\Phi}_{4,3} & \bar{\Phi}_{4,4} \end{pmatrix} < 0, \tag{4.37}$$

$$\begin{pmatrix} Q & QC_z^\top \\ C_zQ & \gamma^2/w_{max}^2 \end{pmatrix} > 0, \tag{4.38}$$

$$\begin{pmatrix} \mathsf{r}^2/w_{max}^2 & Y_r \\ Y_r^\top & Q \end{pmatrix} > 0. \tag{4.39}$$

with

$$\begin{aligned}
\bar{\Phi}_{3,1} &= M_m B_{q_m}^\top - X_m^\top B_\eta^\top + [0 \quad 0 \quad I]Q, \\
\bar{\Phi}_{4,1} &= M_r B_{q_r}^\top - X_r^\top B_\eta^\top + K[C_{u1} - [0 \quad 0 \quad I]]Q - Y_r, \\
\bar{\Phi}_{4,3} &= D_{uq} M_m K - K D_{u\eta 1} X_m, \\
\bar{\Phi}_{4,4} &= -2M_r - K D_{u\eta 1} X_r - K X_r^\top D_{u\eta 1}^\top,
\end{aligned} \tag{4.40}$$

Parameter α can be selected by performing a typical line search. The anti-windup gains satisfying the stability and performance are then given by

$$\Lambda_m = X_m M_m^{-1}, \quad \Lambda_r = X_r M_r^{-1}. \tag{4.41}$$

Using the peak-to-peak Lyapunov approach, the stability of the magnitude and rate limited system is guaranteed by inequalities (4.37) and (4.39), and inequality 4.39 provides the optimized performance measure γ. Anti-windup gains Λ_m and Λ_r are then obtained by solving a convex optimization problem subjected to performance and stability constraints. Further technical details could be found in [51].

4.6.2 Results

In this section the behavior of a SOFC under the magnitude and rate actuator bounds discussed in Section 4.6 is studied through simulations. The objective is to achieve a %16 rise in the FC net power by artificially bounding the inlet flow rate, considering the possible physical bounds on the rate of change of the inlet temperature due to slow dynamics of heat exchanger/mixing chamber. The reasonable bound of $.1^{\circ}$K/s is selected as the rate limit with gain $K = 0.1$ based on the discussions in Section 4.5.1.

Figures 4.30 and 4.31 show the performance of the optimized system with maximum net power, compared with the original system. Fig. 4.31 shows the temperature gradients from the nominal conditions at each node along the cell. As discussed in *Section* 2, the cell is discretized into 5 nodes along the flow direction: Node 1 located at the inlet toward Node 5 placed at the outlet. The required magnitude and rate bounds are applied to the actuators in order to achieve a %16 increase in the net power. The maximized power is available at the cost of at most 5°K increase in temperature gradients, from nominal conditions, along the cell.

As an alternative approach, as presented in [49], a magnitude lower bound was used for the cathode inlet temperature, avoiding it to drop significantly due the AW compensation. Here, the rate limit on the inlet temperature, which could be due to physical constraints and/or control design purposes, addresses this issue and keeps the temperature gradients within an acceptable interval. The overall performance here is superior to the one achieved in [49]. As an example, the rate bound eliminates excessive temperature gradients along the cell.

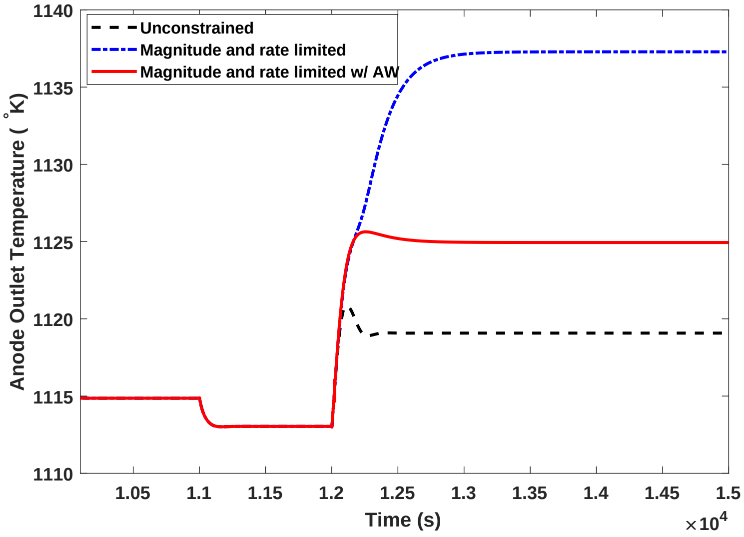

Figure 4.30: Anode outlet temperature for system with optimized net power (with and without AW) and the original system

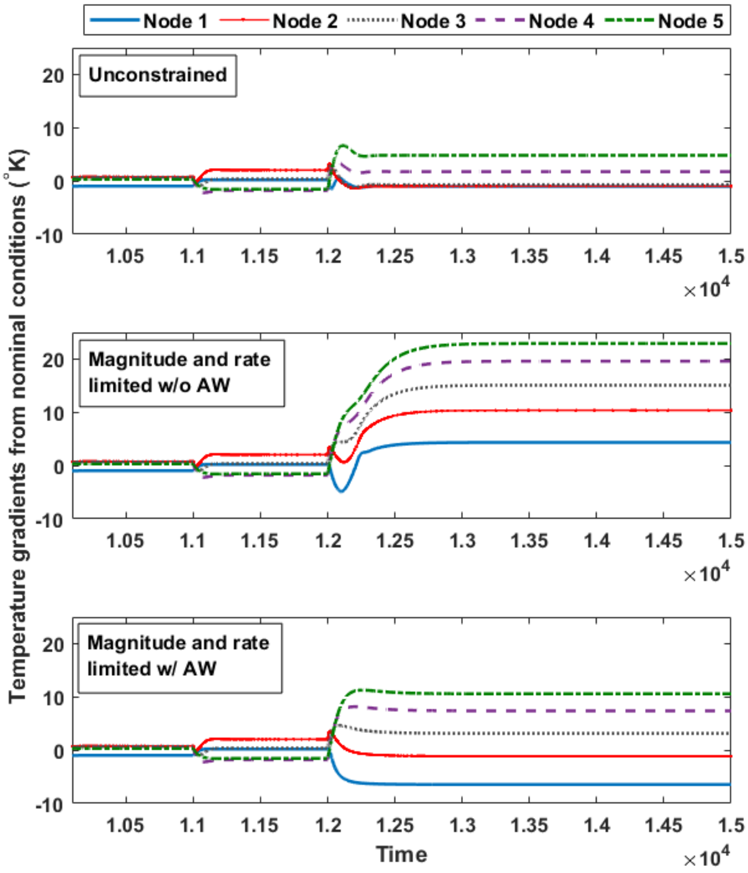

Figure 4.31: Temperature gradients for system with optimized net power (with and without AW) and the original system

Chapter 5

Analog-to-Digital Conversion Application

Delta-sigma analog-to-digital converters (ADCs) have been extensively used for applications that require a wide dynamic range (DR) such as digital audio, wireless communication, and biomedical systems [56, 61]. A wide DR can be achieved by increasing either the number of quantization levels or the loop filter order. The latter often causes instability, while the former needs a highly linear multi-bit digital-to-analog converter (DAC). To avoid instability, the single-loop high-order (> 2) modulators require intensive signal scaling by insertion of loop coefficients and/or reduction of internal signal swing [40], but these restrict the DR. On the other hand, cascading of stable first- or second-order modulators can build stable high-order modulators, but cascaded modulators are sensitive to non-idealities in the analog components, requiring expanded analog performance parameters, and thus, excessive power consumption.

Stability of single-loop high-order ΔΣ modulators (ΔΣMs) is mainly restricted by integrator overloading. Large internal signals may overload the integrator/op-amp, particularly when the input amplitude approaches the modulator's full-scale level. The quantizer then cannot follow the large internal signal effectively, which causes the signal grow further inside the loop even beyond the supply voltage, leading to modulator instability. This signal limitation, caused by integrator overload, will lead to nonlinear behavior, thereby generating harmonic distortion in the output power spectrum. Design efforts have been made in the past to overcome this issue. In [3], the stability is achieved by bounding the internal node voltages through insertion of local feedback loops. The error caused by these loops is then canceled by appropriate digital corrections using a stable estimation of an infinite impulse response, increasing implementation complexity. Authors in [68] propose a compensation architecture for CT ΔΣMs based on variable-structure control techniques offering soft-resetting as a better alternative to the conventional resetting presented in [3]. However, it requires the restrictive assumption of infinite sampling rate for the proof of stability.

In this thesis, we introduce an integrator using a local feedback inspired by the anti-windup (AW) control technique [50], [22] that mitigates overloading effects without aggressive signal scaling, resulting in a higher DR. Since the frequency of overloading can be made very low by proper design, the aim of using AW feedback is to monitor the integrator output constantly and detect any undesired overloading that may lead to instability. We show here, by modeling and simulation results, how the integrator overloading can be avoided and the resulting SNDR degradation can be improved. The sufficient condition for stability is derived using the well-known Lyapunov approach accompanied with a guaranteed performance bound provided by the optimal AW gains for the local feedback. For arbitrary large modulator inputs, the AW compensated integrator eliminates the need for digital integrators and additional cancellation filters used in [3] as well as the infinite sampling rate assumption made in [68].

The chapter outline is as follows: Section 5.1 discusses the behavioral model of typical integrators (or low-pass filters) in a second-order ΔΣ modulator. In Section 5.2, the effects of integrator overload on power spectral density (PSD) and signal to noise and distortion ratio (SNDR) are discussed, the overload region is detected and prevented using an overload prevention (OLP) function. Section 5.3 describes the proposed compensated integrator, incorporating an AW feedback technique for alleviating the leakage and overload shortcomings. Section 5.4 provides the simulations results of the compensated second-order modulator.

5.1 Integrator Modeling

The block diagram of an ideal continuous-time (CT) integrator is shown in Fig. 5.1(a) with transfer function $\frac{V_{out}}{V_{in}} = \frac{1}{sT_s}$. Figure 5.1(b) shows a first-order ΔΣ modulator modeled in SIMULINK for CT realization (similar to [65]). The Relay block from SIMULINK is used for the single-bit quantizer (comparator), modeling offset and hysteresis with minimal effect for relatively small deviation from ideal case, due to the dc gain of the filter.

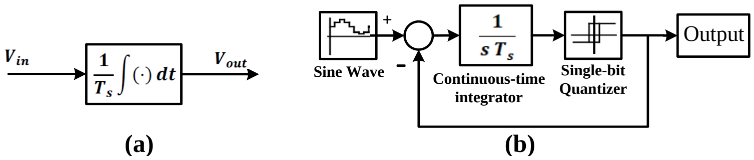

Figure 5.1: Block diagram of an ideal (a) CT integrator (b) first-order low-pass CT $\Delta\Sigma$ modulator.

Leakage is an important non-ideality associated with the integrators in single-loop high-order $\Delta\Sigma$ modulators. Figure 5.2 shows the block diagram of a leaky (or lossy) integrator model in CT domain with transfer function

$$H(s) = \frac{1}{sT_s + 1 - \alpha}, \tag{5.1}$$

where $\alpha < 1$ is the integrator's leakage and $\alpha = 1$ corresponds to an ideal integrator.

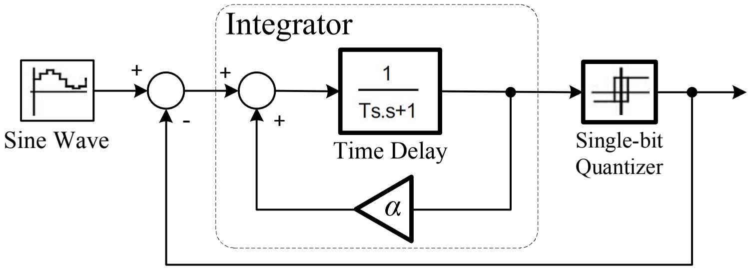

Figure 5.2: Integrator model in SIMULINK.

First-order $\Delta\Sigma$ modulators do not provide the level of performance required in many applications. They suffer from idle tones and require very high sampling frequencies [61]. Therefore, we consider a second-order loop filter in the following discussions. Figure 5.4 shows the common block diagram of a second-order $\Delta\Sigma$ modulator with leakage (i.e. α_1 and α_2 factors). The model consists of two integrators, two DAC feedbacks, and the scaling loop coefficients a_1, a_2, b_1, b_2 to stabilize the loop. The parameter and coefficient values used in Fig. 5.4 are summarized in Table 5.1, where the coefficients are optimized for achieving the best possible performance.

Table 5.1: Optimal coefficients and system parameters.

Coefficient	Value	Parameter	Value
α_1	0.99	Signal bandwidth	$BW = 10.24$kHz
α_2	0.98	Sampling frequency	$f_s = 16.384$MHz
a_1	0.25	Input frequency	$f_{in} = 1.75$kHz
a_2	0.5	Oversampling ratio	$OSR = 800$
$b_1 = b_2$	0.5	Number of output samples	$N = 65536$

The effect of integrator leakage on the modulator PSD and SNDR is shown in Fig. 5.3. For the sake of comparison, a practical value of $\alpha_2 = 0.98$ is selected for the second loop, while the first leakage coefficient α_1 is variable. The ideal case with $\alpha_1 = 1$ gives the highest SNDR of 106dB. While, as expected, for lower values of α_1, leakage is introduced, thus the noise floor increases and the SNDR degrades significantly.

5.2 Integrator Overload

A ΔΣM becomes unstable when the modulator input amplitude exceeds a value that causes quantizer overloading. When the quantizer is subjected to overloading, the modulator output signal no longer increases linearly with the input signal, therefore the SNDR drops substantially and cannot be restored to its previous values even if

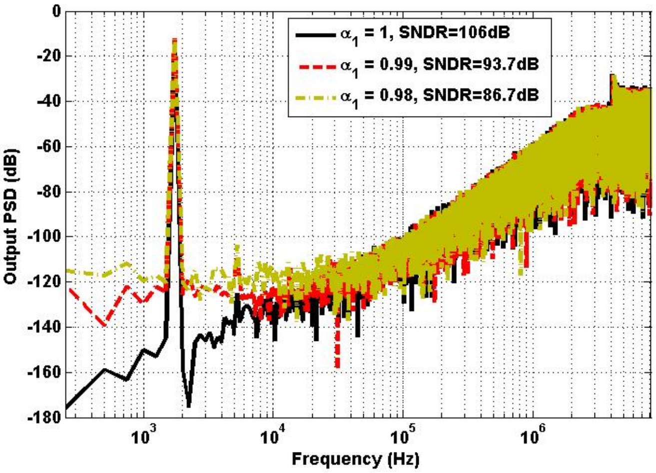

Figure 5.3: Effect of leakage α_1 on PSD and SNDR with $\alpha_2 = 0.98$.

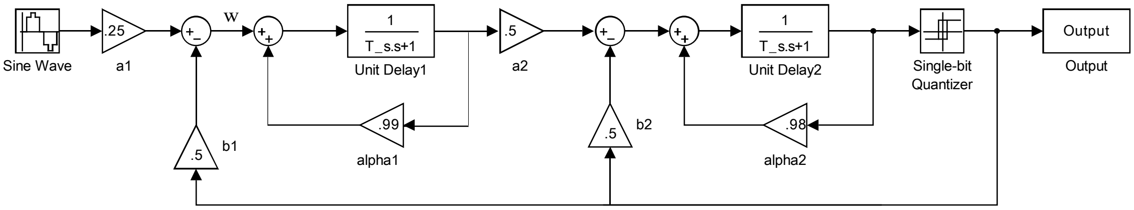

Figure 5.4: The scaled second-order single-loop ΔΣM model in SIMULINK including leakage. The single-bit quantizer realized by a relay consists of the offset and hysteresis.

the input level reduces to its previous amplitude.

5.2.1 Overload Detection

In a ΔΣM the input amplitude range is given as $[0 \quad V_{FS}/2]$, with V_{FS} to be the full-scale amplitude. Figure 5.5 plots the SNDR versus the sinusoidal input signal amplitude in dB full scale (dBFS). The overloading phenomena starts when the modulator input (sinusoid) amplitude approaches $V_{FS}/2$, thus, the nonlinear distortion within signal bandwidth (dc to 10.24kHz in our case) increases, and a significant drop in the SNDR occurs. The maximum SNDR value before that drop is labeled as SNDR$_{peak}$ and the input signal level 3dB below that is often referred to as the overload level of the ΔΣ modulator[60]. According to Fig. 5.5, $V_{OL} = 0.59$V (or equivalently -6dBFS) is estimated as the integrator overload voltage for the modulator shown in Fig. 5.4.

5.2.2 Overload Prevention

When the modulator's input exceeds the overload point, the integrator's output enters the gray zone in Fig. 5.6c, where the modulator is prone to instability. In order to increase the dynamic range in higher-order modulators while allowing for large signal scaling coefficients, we propose an enhanced integrator in which a large overload level or signal clipping can be tolerated. The proposed integrator, shown in Fig. 5.6(a), employs an overload prevention (OLP) function, which prevents the integrator output from entering the overload region, thus, avoids instability. The OLP function, shown in Fig. 5.6(b), is a piecewise-linear function, exhibiting unity gain for $|V_{OUT}| \leq V_{OL}$ and $\pm V_{OL}$ otherwise (*i.e.* standard saturation). The overload voltage estimated in Section 5.2.1 is used here as the V_{OL} in the OLP function introduced in Fig. 5.6(a). Figure 5.7 illustrates the integrator's input-output characteristic. The OLP function ensures that the integrator's output never goes above V_{OL}, and thus, the integrator is never overloaded.

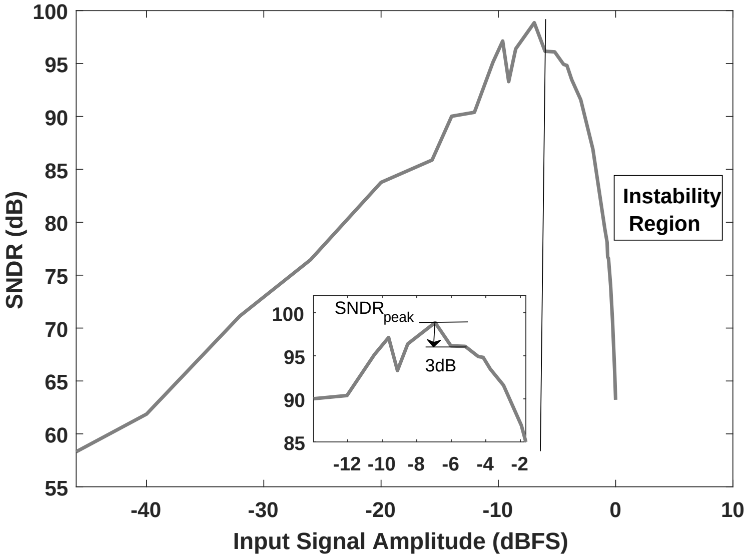

Figure 5.5: Estimating the integrator overload using SNDR curve.

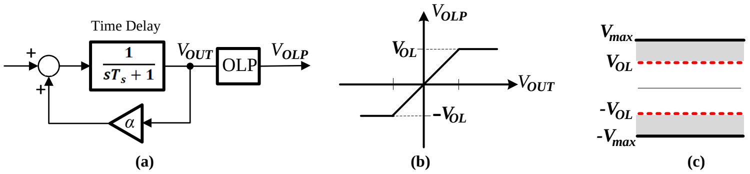

Figure 5.6: CT integrator with OLP function.

OLP, however, creates significant harmonic distortions within the desired bandwidth at the output PSD and causes significant SNDR degradation. To investigate the effects of OLP on ΔΣM's output PSD and SNDR, we introduce an overload factor, K_{OL}, that quantifies how much the integrator output may enter the overloaded region (Fig. 5.7c). The K_{OL} factor is defined as the ratio of the input signal amplitude at $V_{OL} = 0.59$V (here 0.5V) and the current input signal amplitude. For example, $K_{OL} = 1$ corresponds to no overload (inactive OLP) while $K_{OL} = 0.67$ corresponds to input amplitude of 0.75V causing a 50% overload. Figure 5.8 shows the effect of OLP on the output PSD and odd-order in-band harmonics of systems with various K_{OL} values. OLP causes the third- and fifth-order harmonic distortion (*i.e.*, HD3 and HD5 to be relative values with respect to the power of input tone) to grow largely as K_{OL} gets smaller. For instance, for $K_{OL} = 0.56$, the artificial saturation introduced by OLP, which does not allow the integrators outputs to go above the nominal overload level (0.59V obtained from the analysis of Fig. 5.5), increases the HD3 from -101.2dB to -70.8dB and the HD5 from -107.2dB to -75.9dB, respectively. Moreover, the SNDR decreases from 96.3dB to 69.65dB, which is unacceptable in many applications.

As expected, OLP introduces harmonic distortion (or nonlinearity) at the desired low frequencies of the PSD. Thus, while inserting a saturation element may avoid the integrator overload, if left unmitigated, it can cause severe problems and our AW approach is meant to remediate it.

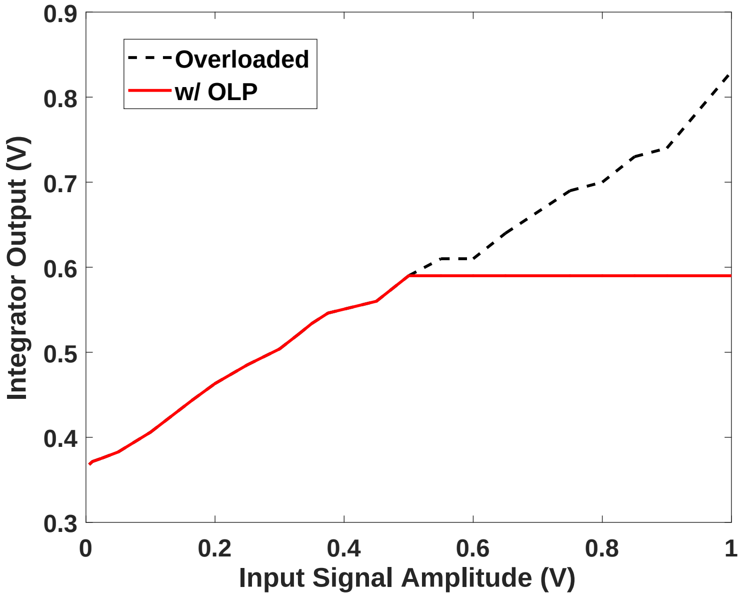

Figure 5.7: Limiting the integrator's output with OLP in order to avoid overloading.

5.3 Anti-windup design

We propose an augmentation technique inspired by anti-windup design for the internal loops in order to minimize the effects of the integrator OLP nonlinearities. Anti-windup compensation is a well-known technique in control systems to guarantee the stability and enhance the performance in the presence of overload. The idea here is to take the error prior and after the OLP (V_{OUT} and V_{OLP} in Fig. 5.6(a), respectively), and add it, after scaling, to the integrator input through a feedback loop. AW feedback loops suppress the integrator input signal amplitude when its output exceeds the overload limit and remains inactive otherwise. By employing AW feedback, we can achieve both stability and SNDR improvement simultaneously through convex minimization of the input-output performance level ($\mathscr{L}_2$ gain), subject to linear matrix inequality constraints.

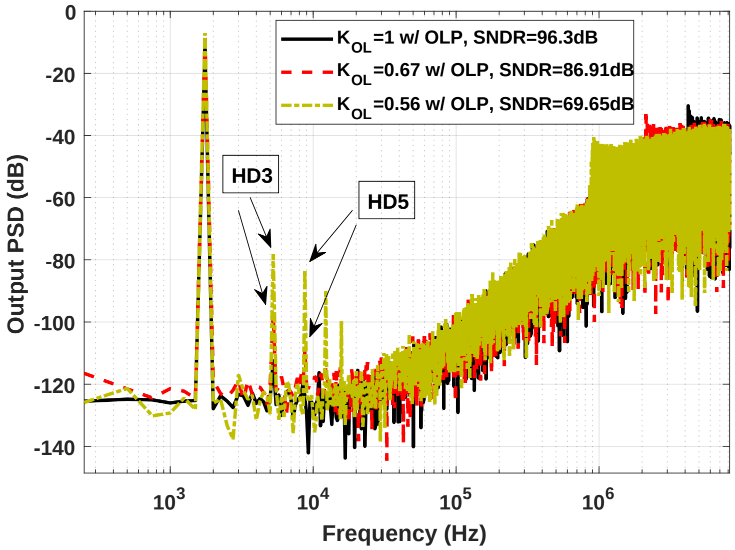

Figure 5.8: Effect of OLP on PSD and SNDR with $\alpha_1 = 0.99$ and $\alpha_2 = 0.98$.

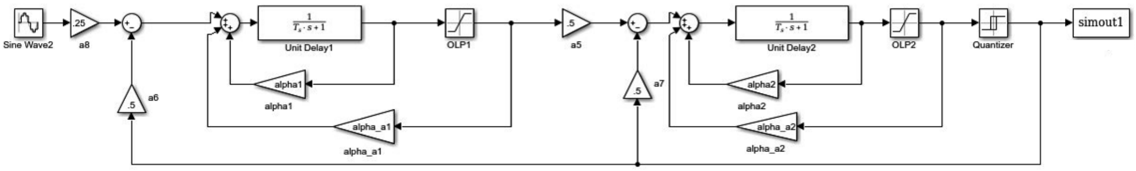

Figure 5.9: The scaled second-order single-loop ΔΣM model in SIMULINK with artificial leakage.

For anti-windup design, the saturation element needs to be inside a closed-loop, however here, according Fig. 5.6(a), the OLP block is not within a closed-loop system. In order to accommodate this condition, as shown in Fig. 5.10, we add an artificial feedback with small leakage gain α_a which closes the loop with negligible effect on system performance. Figure 5.11 also shows that by choosing small values for the artificial leakage (α_{a1} and α_{a2} in Fig. 5.9), system performance remains unchanged (less than 1dB drop in SNDR).

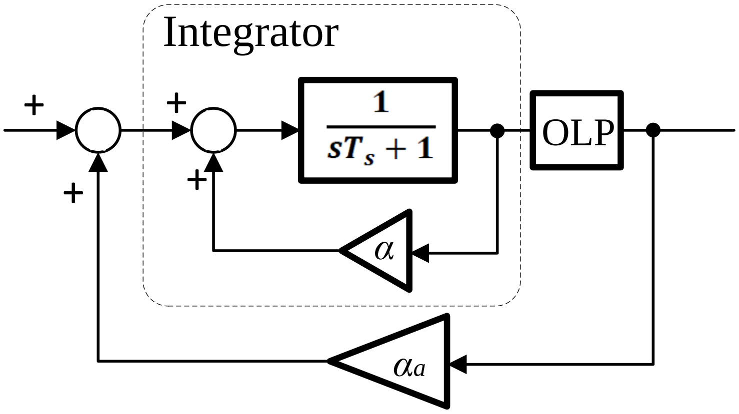

Figure 5.10: Overload prevented integrator with negligible artificial leakage.

The block diagram in Fig. 5.10, could now be interpreted as a control feedback loop for the standard AW design shown in Fig. 5.12. Block *C* shown in Fig. 5.12

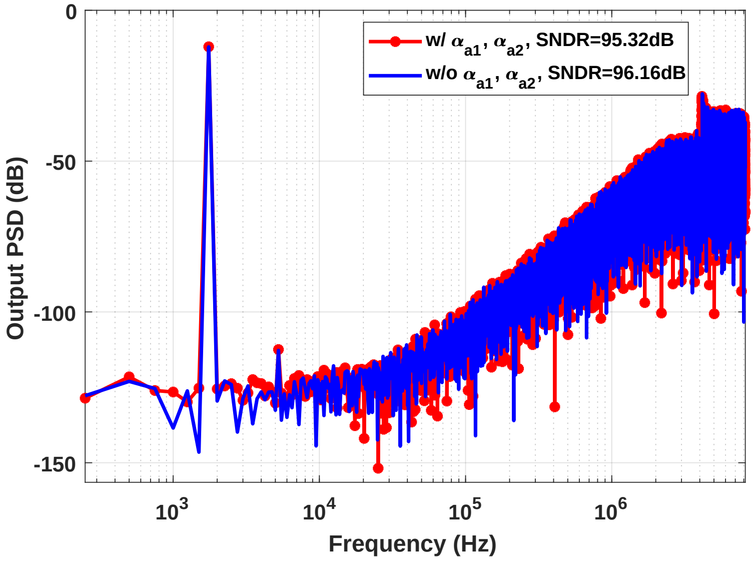

Figure 5.11: Effect of α_a on PSD and SNDR.

corresponds to the integrator shown in Fig. 5.10, while the plant P in Fig. 5.12 corresponds to a simple unity-gain connection in Fig. 5.10.

The integrator block with transfer function $\frac{1}{sT_s+1-\alpha}$ playing the role of the unconstrained controller C with internal state x_c (i.e. integrator state) and a state-space

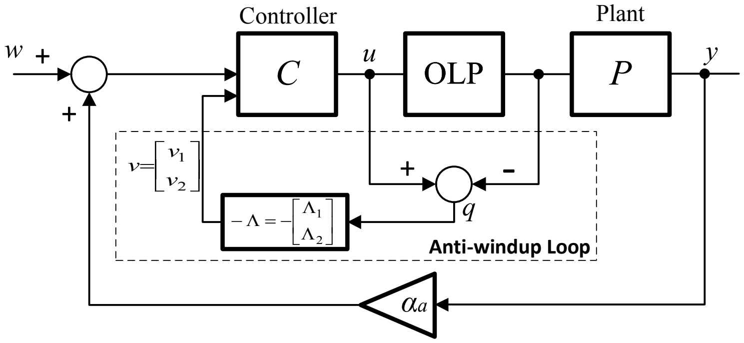

Figure 5.12: Anti-windup schematic.

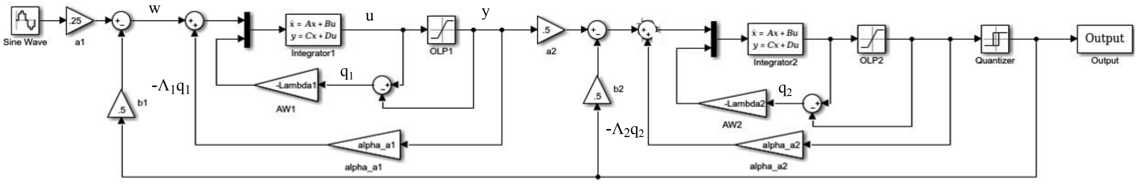

Figure 5.13: Behavioral model of a second-order delta-sigma modulator including anti-windup compensation feedback.

realization of

$$\dot{x}_c = A_c x_c + B_{cy} y + B_{cw} w, \quad u = C_c x_c, \tag{5.2}$$

with w as the input to the integrator and

$$\left[\begin{array}{c|c|c|c} A_c & B_{cy} & B_{cw} & C_c \end{array}\right] = \left[\begin{array}{c|c|c|c} \frac{\alpha_1 - 1}{T_s} & \alpha_{a1} & 1 & 1/T_s \end{array}\right]. \tag{5.3}$$

As shown in Fig. 5.6, the integrator output is subject to OLP *i.e.* $|y| \leq V_{OL}$ with V_{OL} as a known positive constant estimated in Section 5.6. The OLP output y is thus modeled as $y = \text{OLP}(u)$ with the overload function defined in Fig. 5.6.

In the presence of OLP nonlinearities, the stability and the performance guarantees may no longer be valid. The objective here is to design an augmentation that introduces suitable additive signals v_s and v_u to the state dynamics and output of the unconstrained controller (5.2), respectively

$$\begin{aligned} \dot{x}_c &= A_c x_c + B_{cy} y + B_{cw} w + v_s, \\ u &= C_c x_c + v_u. \end{aligned} \tag{5.4}$$

Following the standard approach in anti-windup design [50, 22], the error between the input and output of the OLP element, q, is used to generate anti-windup compensation, with SIMULINK modulator model shown in Fig. 5.13. The vector signal v in (3.9) ($v^\top = [v_s \quad v_u]$) is then $v = -\Lambda q$ with $\Lambda = [\Lambda_s \quad \Lambda_u]^\top$ as shown in the figure.

These modifications should make the closed-loop system stable with a guaranteed input-output performance level in the presence of OLP nonlinearities in the control loop.

Substituting $y = u - q$ in (3.9), it is straightforward to build the closed-loop system with state x_c, and w and q as input signals. The closed-loop system with anti-windup gains can be written as

$$\begin{aligned} \dot{x}_c &= (A_c + B_{cy}C_c)x_c + B_{cw}w - ([1 \quad B_{cy}]\Lambda + B_{cy})q, \\ u &= C_c x_c - [0 \quad 1]\Lambda q, \end{aligned} \tag{5.5}$$

with y to be the performance measurement and $\alpha_1 = 0.99$.

Theorem 5.3.1 ***(Integrator stability: Sufficiency condition)***
Consider the block diagram shown in Fig. 5.12 with a unity-gain for plant P and the integrator (5.2) *as the nominal controller C. Then, given the OLP function shown in Fig. 5.6, there exists a solution for the convex minimization problem*

$$\min_{Q,M,X,\gamma^2} \quad \gamma^2 \tag{5.6}$$

subject to the linear matrix inequality

$$\begin{pmatrix} 2Q(A_c+B_{cy}C_c) & * & * & * \\ B_{cw} & -\gamma & * & * \\ C_cQ & 0 & -\gamma & * \\ \Phi_{4,1} & 0 & -X^\top[0 \quad 1]^\top - M & \Phi_{4,4} \end{pmatrix} < 0, \tag{5.7}$$

with $M = W^{-1}, \quad X = \Lambda M$ *and*

$$\begin{aligned} \Phi_{4,1} &= -X^\top[1 \quad B_{cy}]^\top - MB_{cy} + C_cQ, \\ \Phi_{4,4} &= -2M - [0 \quad 1]X - X^\top[0 \quad 1]^\top. \end{aligned} \tag{5.8}$$

Then, the trajectories of the closed-loop system (5.5)*, using anti-windup gain*

$$\Lambda = XM^{-1}, \tag{5.9}$$

is stable with performance bound

$$y^\top(t)y(t) \le \gamma^2, \quad t \ge 0. \tag{5.10}$$

Proof 5.3.1 *Consider a quadratic Lyapunov function* $V = Q^{-1}x_c^2$ *with* $Q > 0$*. By applying the Schur compliment followed by a congruent transformation the inequality* (5.7) *can be written as*

$$\frac{d}{dt}(Q^{-1}x_c^2) + \gamma^{-1}y^2 - \gamma w^2 - 2qW(q-u) < 0. \tag{5.11}$$

Using the definition of OLP nonlinearity (Fig. 5.6), $2qW(q-u) \geq 0$, *thus,* (5.11) *reduces to*

$$\dot{V} + \gamma^{-1}y^2 - \gamma w^2 < 0. \tag{5.12}$$

An integration with zero initial condition, ensures stability with performance measure γ *as the guaranteed* $\mathscr{L}_2$ *gain from* w *to* y *(more details in [6]).* □

The anti-windup design requires the closed-loop system to be stable; i.e. the coefficient multiplying x_c on the right-hand side of (5.5) should have a strictly negative eigenvalue. Substituting the values in (5.3), this coefficient is given by

$$A_c + B_{cy}C_c = (\alpha_1 + \alpha_{a1} - 1)/T_s, \tag{5.13}$$

which is stable for $\alpha_1 + \alpha_{a1}$ values strictly less than one.

5.4 Simulation results

Results are presented for 0.75V input signal amplitude, corresponding to $K_{OL} = 0.67$. The overload voltage $V_{OL} = 0.59$V estimated in Section 5.2.1 is used for the OLP function. The AW gains $\Lambda_1 = [-1.5, 0.5]^\top$ and $\Lambda_2 = [-1.7, 0.7]^\top$ are obtained from Matlab convex optimization tools satisfying stability and performance constraints in Theorem 3.5.4.

Figure 5.14 shows the quantizer input signal with and without the AW protection technique proposed here. As shown in the figure, without the overload protection technique, the quantizer input (thus its error) rises at a high rate, resulting in integrator overload and instability. However, using the overload prevention technique, the quantizer input is guaranteed to be bounded avoiding the integrator overload.

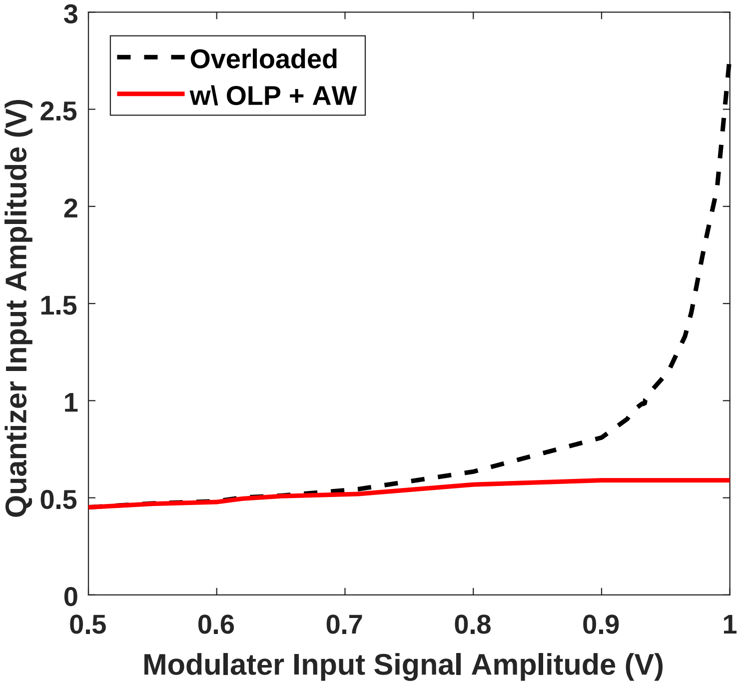

Figure 5.14: Effect of OLP and AW on quantizer overload.

Figure 5.15 shows the PSD of the system when the output of the integrators are subject to OLP with $\pm V_{OL}$. For this considerable level of overload, the proposed AW technique has achieved a less than 1dB drop from $SNDR_{peak}$ while ensuring stability for almost %50 larger input amplitudes. Note also, using AW, the third and fifth harmonic distortions have been significantly reduced. Therefore, the AW augmentations have significantly improved the performance of the modulator with OLP while maintaining the stability by reducing the quantizer input and avoiding its overload. This shows that the anti-windup compensated system is able to increase the dynamic range of the modulator and accommodate larger input signals safely, without overloading the integrator.

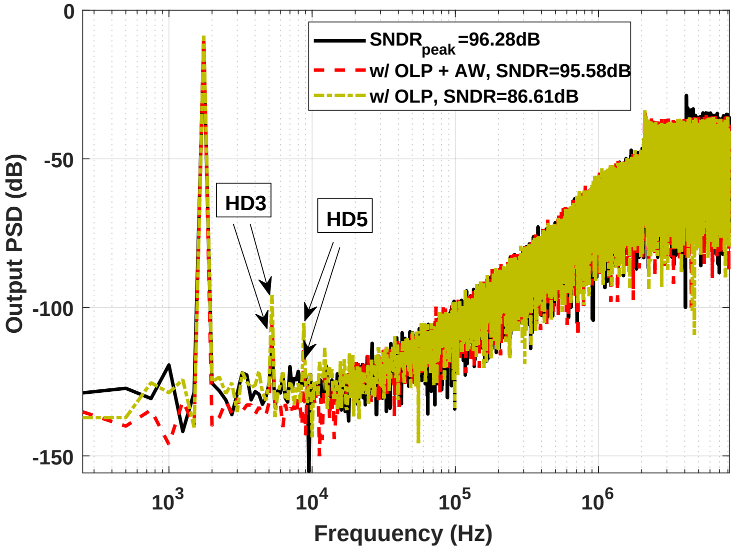

Figure 5.15: Effect of AW on PSD and SNDR with $K_{OL} = 0.67$.

5.5 Conclusion

A compensated integrator using an AW feedback technique was proposed to stabilize $\Delta\Sigma$ modulators by avoiding integrator overload while minimizing the resulting performance degradation. Using the compensated integrator in a second-order modulator, SNDR can be retrieved quite close to its peak value while accommodating a 50% higher DR. Meanwhile, the overload caused by limited integrator slew-rate can also be dealt with using this technique (not the focus of this thesis), facilitating the design of low-power integrators employing amplifiers with relaxed slew-rate.

Chapter 6

Cooperative Control Application

6.1 INTRODUCTION

Control of a network of cooperative agents has received tremendous attention in recent years and a variety of issues have been studied, including control, communications, security or connection preserving. A proper review of the full range of results is beyond the scope of this note. Among the various consensus and cooperation problems in networked multi-agent systems (e.g. [47, 16]), here we study the problem of tracking (or following) a leader by a group of agents. In the majority of related results such as [66, 37, 23], the leader's input is considered to be either zero or available to all follower agents. However, this can be a highly restrictive assumption in many applications, specifically for large networks. The leader may require a nonzero control input in order to take specific actions, and/or its input might not be available to a subset, or even any of the followers, for instance, when the leader appears to be an uncooperative target.

In this thesis we study the distributed tracking control of multi-agent systems with an active leader with bounded nonzero time-variant input signal. Furthermore, the restrictive assumption of the availability of the leader's input to all agents is not a requirement here. In fact, we consider a case in which the leader receives no information from any of the followers and its input is not available to any of the following agents. As a result, we assume an undirected graph among the followers and a directed path from the leader to all followers. We do not require the followers to be stable, however, they are assumed to be stabilizable.

Distributed tracking control of homogeneous multi-agent systems has been studied in [66, 37], assuming that the leader and the followers share exactly the same dynamics, thus, not applicable to the tracking problem of a leader with an unknown nonzero input. In [38], a distributed discontinuous tracking controller is proposed and non-smooth analysis tools are used to solve the tracking problem for multi-agent systems with nonzero leader input. The suggested algorithm also requires the leader's input to be bounded in order to handle the nonlinear term in the controller, which might not be practical given the unavailable nature of the signal. Here, we investigate the same problem studied in [38], however, we propose a linear state feedback controller capable of achieving tracking, avoiding discontinuities in the control process, as well as the boundedness assumption for the leader's input.

The availability of full-state information, for control design, could be a restrictive assumption in many applications. Therefore, the results have been extended to an output feedback controller using measured output information. In [66], taking advantage of the duality of the controller and observer design, an output feedback controller has been designed for synchronization problem of general linear systems using an LQR based optimization method. However, in [66], the leader is assumed to have zero input, therefore, the results presented are not applicable here.

Among the issues that have received relatively limited attention, in cooperative control of multi-agent systems, is the potential for encountering actuator limitations, which is one of the most common problems faced in high performance control of single agent (non-network) systems. References [55, 21, 20], address this problem through robustness or reliability techniques by roughly speaking, designing controllers that can withstand severe degradation in actuation authority. Such approaches may lead to conservative results, as the control system requires resiliency to such failures. An alternative approach, that has been studied extensively for single agent systems ([8, 22, 27]), is to maintain a high performance controller but design anti-windup augmentation loops that become active only if actuators are saturated. In this note, we also develop an anti-windup approach for use in cooperative control problems. Although the stability of the uncontrolled agents is not a requirement for the state and output feedback controllers proposed, the magnitude anti-windup design requires that. However, this condition may be lifted through magnitude and rate anti-windup design using an approach similar to the one used in [52]. Such technical details are not covered here due to space limitations.

6.2 Preliminaries

Notations: Let $0_{n\times m}$ be the n by m matrix of zeros, I_n the $n\times n$ identity matrix, and $\mathbf{1}$ the vector with all entries be one. For a symmetric matrix A, $A>0$ indicates that A is positive definite. $A=\mathrm{diag}(a_i)$ is a diagonal matrix with a_i diagonal entries. He(A) is $A+A^\top$. We denote the Kronecker product by $\otimes$. Here, $x\mapsto y\in[0,I_n]$ denotes a decentralized nonlinear map, where $x_i\mapsto y_i$ belongs to sector $[0,1]$ and $y_i^\top(x_i-y_i)\geq 0$ for all $x_i\in\mathbb{R}^n$ ([31]). It is easy to see that if W is diagonal positive definite, then $y^\top W(x-y)\geq 0$ as well with $x=[x_1,...,x_n]^\top$ and $y=[y_1,...,y_n]^\top$.

6.2.1 Graph Theory Basics

A directed graph $\mathscr{G}$ is composed of a node set $\mathscr{V}$ and an edge set $\mathscr{G}\subseteq\mathscr{V}\times\mathscr{V}$ with an edge representation (v_i,v_j), where v_i is the parent node, v_j is the child node, and v_i is a neighbor of v_j. A graph is undirected if for all $v_i,v_j\in\mathscr{V}$, $(v_i,v_j)\in\mathscr{E}$ implies that $(v_j,v_i)\in\mathscr{E}$.

For an unweighted graph $\mathscr{G}$, the adjacency matrix $\mathscr{A}=[a_{ij}]\in\mathbb{R}^{N\times N}$ is defined by

$$a_{ij}=\begin{cases}0 & \text{if} \quad i=j \quad \text{or} \quad (v_j,v_i)\notin\mathscr{E}\\ 1 & \text{if} \quad (v_j,v_i)\in\mathscr{E}\end{cases}$$

The Laplacian matrix $\mathscr{L}=[\mathscr{L}_{ij}]\in\mathbb{R}^{N\times N}$ is also defined as $\mathscr{L}_{ii}=\sum_{j\neq i}a_{ij}$ and $\mathscr{L}_{ij}=-a_{ij}, i\neq j$, which is symmetric for an undirected graph.

6.2.2 Problem Statement

A group of agents with general dynamics

$$\dot{x}_i = Ax_i + Bu_i, \quad i = 0, \ldots, N \tag{6.1}$$

are considered, with agent 0 the leader and agents $1, \ldots, N$ the followers. As mentioned earlier, similar to [38], we assume that the leader receives no information from the followers and its control input is not available to any follower, but a subset of the followers have access to its states. Therefore, the following assumption holds for the interaction graph.

Assumption 6 *A directed graph $\mathscr{G}$, represents the interaction between all agents. However , an undirected subgraph $\mathscr{G}_s$ represents the interaction of the N followers. Moreover, graph $\mathscr{G}$ contains a directed spanning tree with the leader as the root.*

The Laplacian matrix associated with graph $\mathscr{G}$ is given by $\mathscr{L}$ which can be partitioned as

$$L = \begin{bmatrix} 0 & 0_{1\times N} \\ \mathscr{L}_2 & \mathscr{L}_1 \end{bmatrix}, \tag{6.2}$$

where matrix $\mathscr{L}_1$ is associated with the undirected subgraph $\mathscr{G}_s$ and is thus symmetric.

In this thesis, different from [66, 37, 23], but similar to [38], we consider the general case in which the leader input u_0 is nonzero, changes with time, and none of the follower agents have access to it.

For a given $w_{max} \in \mathbb{R}_{>0}$, we wish to design a controller which makes the closed-loop system internally stable with a guaranteed input-output performance measure χ, such that

$$z^{\top}(t)z(t) \leq \chi^2, \text{ for } u_0^{\top}(t)u_0(t) \leq w_{max}^2, \ \forall t \geq 0, \tag{6.3}$$

where z is the performance output, to be defined later. We do not require u_0 to be bounded, for a larger w_{max}, we simply get a scaled performance measure χ. Moreover, the basic approach can be used to solve other objectives such as energy-to-peak, etc.

Assumption 7 (No feed-through terms in performance output) For simplicity, the performance output is assumed to depend only on the states and have no feed-through terms; i.e., $z = C_z x$. □

This assumption is only made for representation simplicity. Including the u term in the performance output is relatively straightforward but complicates the resulting LMIs, and inclusion of the w term would require an additional line search.

6.3 State Feedback Controller

The linear state feedback controller

$$u_i = K \sum_{j=0}^{N} a_{ij}(x_i - x_j) \tag{6.4}$$

is used for the distributed tracking problem with unknown leader input. Compared to the discontinuous controllers proposed in [38, 7], the signum term required for tracking of an active leader with non-zero input, as well as the corresponding non-smooth analysis, have been avoided and a fully linear controller is used.

The error dynamics $\dot{\zeta}_i = \dot{x}_i - \dot{x}_0$ together with (6.1) and (6.4) lead to the closed-loop dynamics

$$\dot{\zeta}_i = A\zeta_i + BK \left[\sum_{j=1}^{N} a_{ij}(\zeta_i - \zeta_j) + a_{i0}\zeta_i \right] - Bu_0, \tag{6.5}$$

for $i = 1, ..., N$. The compact form of the closed-loop system is then given by

$$\dot{\zeta} = (I_N \otimes A + \mathscr{L}_1 \otimes BK)\zeta - (\mathbf{1} \otimes B)u_0 \tag{6.6}$$

Due to the unknown nature of the leader's input, and in order to avoid the nonlinear controllers used in [38], we propose to consider u_0 a disturbance $\underline{w}$, thus,

$$\dot{x}_0 = Ax_0 + B\underline{w}. \tag{6.7}$$

Theorem 6.3.1 (Leader Tracking using Peak-to-Peak Synthesis) *Consider the agents* *and leader dynamics given by* (6.1) *and* (6.7)*. The state feedback controller* (6.4) *solves the distributed tracking control problem with* $K = GP^{-1}$*, where* $P > 0$ *and* G *are solutions to the convex minimization problem*

$$\min_{P,G,\chi^2} \quad \chi^2 \tag{6.8}$$

subject to the Linear Matrix Inequalities

$$\begin{pmatrix} AP + PA^\top + \lambda_i(BG + G^\top B^\top) + \alpha P & -B \\ -B^\top & -\alpha I \end{pmatrix} < 0,$$

$$i = 1, ..., N, \tag{6.9}$$

$$\begin{pmatrix} P & PC_z^\top \\ C_z P & \frac{\chi^2}{w_{max}^2} I \end{pmatrix} > 0. \tag{6.10}$$

Also the closed-loop system (6.5) *has reachable set*

$$\zeta(t) \in \mathscr{E}(P^{-1}, w_{max}^2) = \{\zeta : \zeta^\top (I_N \otimes P^{-1})\zeta < w_{max}^2\}, \tag{6.11}$$

and performance measure χ *from* w *to* z*.*

Proof 6.3.1 *Consider the positive definite Lyapunov function*

$$V = \zeta^\top (I_N \otimes P^{-1})\zeta, \tag{6.12}$$

with $P > 0$. Using the peak-to-peak approach, the reachable set (6.11) *is achieved if*

$$\dot{V}(\zeta(t)) + \alpha(V(\zeta(t)) - w(t)^\top w(t)) < 0, \tag{6.13}$$

with $w = \mathbf{1} \otimes \underline{w}$. Taking the derivative of V along the closed-loop dynamics (6.6) *gives*

$$\begin{aligned}
&\dot{V} + \alpha(V - w^\top w) = \frac{d}{dt}(\zeta^\top (I_N \otimes P^{-1})\zeta) + \\
&\alpha(\zeta^\top (I_N \otimes P^{-1})\zeta - w^\top w) \\
&= He[\zeta^\top (I_N \otimes P^{-1}A + \mathscr{L}_1 \otimes P^{-1}BK)\zeta \\
&- \zeta^\top (\mathbf{1} \otimes P^{-1}B)\underline{w}] + \alpha(\zeta^\top (I_N \otimes P^{-1})\zeta - w^\top w).
\end{aligned} \tag{6.14}$$

By changing the variable $\tilde{\zeta} = (I_N \otimes P^{-1})\zeta$, (6.14) *can be written as*

$$\begin{aligned}
\dot{V} + \alpha(V - w^\top w) = \tilde{\zeta}^\top (I_N \otimes (AP + PA^\top) \\
+ \mathscr{L}_1 \otimes PK^\top B^\top)\tilde{\zeta} - He[\tilde{\zeta}^\top (I_N \otimes B)w] \\
+ \alpha(\tilde{\zeta}^\top (I_N \otimes P)\tilde{\zeta} - w^\top w).
\end{aligned} \tag{6.15}$$

We now let $U \in \Re^{N \times N}$ be a unitary matrix such that $U^\top \mathscr{L}_1 U = \Lambda = diag(\lambda_i)$,

$\bar{\zeta} = (U^\top \otimes I_n)\tilde{\zeta}$, and $\bar{w} = (U^\top \otimes I_m)w$. Then (6.15) *gives*

$$\begin{aligned}
&\dot{V} + \alpha(V - w^\top w) = \bar{\zeta}^\top (I_N \otimes (AP + PA^\top) \\
&+ \Lambda \otimes BKP + \Lambda \otimes PK^\top B^\top)\bar{\zeta} - He[\bar{\zeta}^\top (I_N \otimes B)\bar{w}] \\
&+ \alpha(\bar{\zeta}^\top (I_N \otimes P)\bar{\zeta} - \bar{w}^\top \bar{w}) < 0. \qquad (6.16)
\end{aligned}$$

By setting $G = KP$, it can be shown that (6.16) *is equivalent to*

$$\begin{pmatrix} \bar{\zeta}^\top \bar{w}^\top \end{pmatrix} \begin{pmatrix} F_1 & 0 & \dots \\ 0 & \ddots & \\ \vdots & & F_N \end{pmatrix} \begin{pmatrix} \bar{\zeta} \\ \bar{w} \end{pmatrix} < 0, \qquad (6.17)$$

with F_i to be the main matrix in inequality (6.9) *(i.e.* (6.9) *can be written as $F_i < 0$).*

Given the disturbance bound $\underline{w}^\top(t)\underline{w}(t) \leq w_{max}^2$, and the performance output $z_i = C_z\zeta_i$ for each agent, the performance measure $z^\top z \leq \chi^2$ with $z = [z_1^\top ... z_N^\top]^\top$, is guaranteed by

$$\zeta^\top [(I_N \otimes P^{-1}) - \frac{w_{max}^2}{\chi^2}(I_N \otimes C_z)^\top (I_N \otimes C_z)]\zeta > 0. \qquad (6.18)$$

Recalling the Schur complement, (6.18) *is equivalent to*

$$\begin{pmatrix} I_N \otimes P^{-1} & (I_N \otimes C_z)^\top \\ I_N \otimes C_z & \frac{\chi^2}{w_{max}^2} I_N \end{pmatrix} > 0. \qquad (6.19)$$

After expanding the Kronecker products and conducting a few row/column manipulations, (6.19) *reduces to* (6.10)*.*

Remark 6.3.1 *In Theorem 6.3.1, α enters the inequality in a product form. For optimized performance, a line search is done, as in other peak-to-peak gain problems. However, other standard techniques such as the energy-to-peak approach could also be used which removes parameter α from the analysis.*

Remark 6.3.2 *Theorem 6.3.1 uses the same P matrix in all of the LMIs and it requires the eigenvalues of the Laplacian matrix $\lambda_1, ..., \lambda_N$ to be known. As a result, the computation of the controller is done centrally.*

In order to relax this restriction, the traditional technique used in [66, 38], can be used here to obtain a controller that is easier to calculate, and can accommodate possible network topology changes (as long as the graph stays connected).

Consider the linear distributed state feedback controller

$$u_i = cK \sum_{j=0}^{N} a_{ij}(x_i - x_j) \tag{6.20}$$

with $c > 0$.

Theorem 6.3.2 (Distributed Tracking using Peak-to-Peak Synthesis) *Consider the agents and leader dynamics given by* (6.1) *and* (6.7). *The state feedback controller* (6.20) *with $c \geq 1/\lambda_1$, solves the distributed tracking control problem with $K = -B^\top P^{-1}$, where $P > 0$ is a solution to the convex minimization problem*

$$\min_{P, \chi^2} \quad \chi^2 \tag{6.21}$$

subject to the Linear Matrix Inequalities

$$AP + PA^\top + \alpha P + BB^\top(1/\alpha - 2) < 0, \tag{6.22}$$

$$\begin{pmatrix} P & PC_z^\top \\ C_zP & \chi^2/w_{max}^2 I \end{pmatrix} > 0. \tag{6.23}$$

Proof 6.3.2 *Following the proof of Theorem 6.3.1, substitute* $K = -B^\top P^{-1}$ *in* (6.16). *The Lypunov stability condition is then given by* (6.17) *with*

$$F_i = \begin{pmatrix} AP + PA^\top - 2c\lambda_i BB^\top + \alpha P & -B \\ -B^\top & -\alpha I \end{pmatrix}, \tag{6.24}$$

for $i = 1, ..., N$. *Recalling the Schur complement,* (6.24) *is equivalent to*

$$AP + PA^\top + \alpha P - 2c\lambda_i BB^\top + BB^\top/\alpha < 0, \tag{6.25}$$

$$i = 1, ..., N.$$

Since $c \geq 1/\lambda_i$ *for* $i = 1, ..., N$*, all inequalities in* (6.25) *are satisfied if* (6.22) *holds.*

Similar to the proof of Theorem 6.3.1, the performance measure χ *is also guaranteed by* (6.23).

Remark 6.3.3 *Compared to Theorem 6.3.1, Theorem 6.3.2 only requires a lower bound for the smallest non-zero eigenvalue of* $\mathscr{L}_1$ *to be known. However, this mild assumption could also be removed by using the adaptive version of the proposed* *controller in a similar way as suggested in [38]. As a result, both computation and implementation of* (6.20) *are decentralized.*

6.4 Output Feedback Controller

In many applications, having access to all of the state variables is a limiting assumption, thus, the state feedback controller might not be a feasible option. In this section, a fully distributed output feedback controller is designed for the tracking problem which is based on the relative measurement of neighbor agents.

Consider the general linear dynamics for agents $i = 1, ..., N$. Given the agents and leader's dynamics

$$\begin{aligned} \dot{x}_i &= Ax_i + Bu_i, \\ y_{ai} &= Cx_i, \end{aligned} \tag{6.26}$$

for $i = 0, ..., N$ and $u_0 = \underline{w}$, the tracking error dynamics can be written as

$$\begin{aligned} \dot{\zeta}_i &= A\zeta_i + Bu_i - B\underline{w}, \\ y_i &= C\zeta_i, \end{aligned} \tag{6.27}$$

for $i = 1, ..., N$. The goal is to design the controller

$$\begin{aligned} \dot{\zeta}_{ci} &= A_{ci}\zeta_{ci} + B_c\bar{y}_i, \\ u_i &= C_c\zeta_{ci} + D_c\bar{y}_i, \end{aligned} \tag{6.28}$$

using the output feedback approach, where $\bar{y}_i$ is the relative measurement of agent i with respect to its neighbors and is given by

$$\bar{y}_i = \sum_{j=1}^{N} a_{ij}C(\zeta_i - \zeta_j) + a_{i0}C\zeta_i. \tag{6.29}$$

According to (6.29), agent i can only obtain information from agent j if they are connected through the communication graph, i.e. $a_{ij} = 1$. Substituting for u_i and $\bar{y}_i$, and using the Kronecker products, the plant and controller dynamics can be written in compact form as

$$\begin{aligned} \dot{\zeta}_{cl} = &\begin{bmatrix} I_N \otimes A + \mathscr{L}_1 \otimes BD_cC & I_N \otimes BC_c \\ \mathscr{L}_1 \otimes B_cC & I_N \otimes A_c \end{bmatrix} \zeta_{cl} \\ &+ \begin{bmatrix} -\mathbf{1} \otimes B \\ 0 \end{bmatrix} \underline{w}, \end{aligned} \tag{6.30}$$

where $\zeta_{cl}^\top = [\zeta^\top \quad \zeta_c^\top]$. The following Theorem proposes a linear matrix inequality approach for output feedback controller design in multi-agent systems, motived by critical convexing change of variables used in [41, 32] for single agent case.

Theorem 6.4.1 (Leader Following using Output feedback Approach) *Consider* *the agents and leader dynamics given by* (6.26). *The output feedback controller* (6.28) *solves the tracking control problem with*

$$\begin{aligned} D_c &= D_c, \\ C_c &= W_c X^{-1} - D_c C, \\ B_c &= S^{-1}(YBD_c - W_o), \\ A_{ci} &= S^{-1}[-L_i X^{-1} + YA + YBC_c + YBD_c C] - \lambda_i B_c C, \end{aligned} \tag{6.31}$$

where $S = Y - X^{-1}$*, and* D_c, X, Y, L_i, W_c *and* W_o *are solutions to the convex minimization problem*

$$\min_{X,Y,W_c,W_o,D_c,\chi^2} \quad \chi^2 \tag{6.32}$$

subject to the Linear Matrix Inequalities

$$\begin{pmatrix} He[YA + \lambda_i W_o C] + \alpha Y & * & * \\ L_i^\top + A + \lambda_i BD_c C + \alpha I & He[AX + BW_c] + \alpha X & * \\ -B^\top Y & -B^\top & -\alpha \end{pmatrix} < 0, \tag{6.33}$$

for $i = 1, ..., N$ *and*

$$\begin{pmatrix} Y & I \\ I & X \end{pmatrix} > 0, \quad \begin{pmatrix} Y & I & C^\top \\ I & X & XC^\top \\ C & CX & \frac{\chi^2}{w_{max}^2} I \end{pmatrix} > 0. \tag{6.34}$$

Then the closed-loop system (6.30) *has reachable set*

$$\zeta_{cl}(t) \in \mathscr{E}(P^{-1}, w_{max}^2), \tag{6.35}$$

and performance measure χ *from* w *to* z*.*

Proof 6.4.1 *We let* $U \in \Re^{N\times N}$ *be a unitary matrix such that* $U^\top \mathscr{L}_1 U = \Lambda = diag(\lambda_i)$*,* $\bar{\zeta}_{cl} = (U^\top \otimes I_n)\zeta_{cl}$*, and* $\bar{w} = (U^\top \otimes I_m)w$*. It is straightforward to show that the closed-loop dynamics* (6.30)*, after a few row/column manipulations can be written as*

$$\begin{aligned}\dot{\bar{\zeta}}_{cl} &= diag(\begin{bmatrix} A+\lambda_i BD_cC & BC_c \\ \lambda_i B_cC & A_c \end{bmatrix})\bar{\zeta}_{cl} + (I_N \otimes \begin{bmatrix} -B \\ 0 \end{bmatrix})\bar{w}, \\ &= diag(A_{cli})\bar{\zeta}_{cl} + (I_N \otimes B_{cl})\bar{w}.\end{aligned} \tag{6.36}$$

Consider the positive definite Lyapunov function

$$V = \bar{\zeta}_{cl}^\top (I_N \otimes P^{-1})\bar{\zeta}_{cl}, \tag{6.37}$$

with $P > 0$*. For a peak bounded disturbance signal* $\bar{w}$*, the reachable set* (6.35) *is achieved if*

$$\dot{V} + \alpha(V - \bar{w}^\top \bar{w}) < 0. \tag{6.38}$$

Taking the derivative of V along the closed-loop dynamics (6.36) *gives*

$$\begin{aligned}&\dot{V}+\alpha(V-\bar{w}^\top\bar{w})=\\&He[\bar{\zeta}_{cl}^\top(diag(P^{-1}A_{cli}\bar{\zeta}_{cl})-I_N\otimes P^{-1}B_{cl}\bar{w}]\\&+\alpha(\bar{\zeta}_{cl}^\top(I_N\otimes P^{-1})\bar{\zeta}_{cl}-\bar{w}^\top\bar{w})<0.\end{aligned}\tag{6.39}$$

With $\tilde{\zeta}_{cl}=(I_N\otimes P^{-1})\bar{\zeta}_{cl}$, (6.39) *can be written as*

$$\begin{aligned}\dot{V}+\alpha(V-\bar{w}^\top\bar{w})&=\tilde{\zeta}_{cl}^\top(diag(A_{cli}P+PA_{cli}^\top)\tilde{\zeta}_{cl}\\-He[\tilde{\zeta}_{cl}^\top(I_N\otimes B_{cl})\bar{w}]&+\alpha(\tilde{\zeta}_{cl}^\top(I_N\otimes P)\tilde{\zeta}_{cl}-\bar{w}^\top\bar{w})<0.\end{aligned}\tag{6.40}$$

As shown in proof of Theorem 6.3.1, with

$$\bar{A}_i=\begin{pmatrix}A_{cli}P+PA_{cli}^\top+\alpha P & B_{cl}\\ B_{cl}^\top & -\alpha I\end{pmatrix},\quad i=1,...,N,\tag{6.41}$$

and A_{cli} and B_{cl} as defined in (6.36), *inequality* (6.40) *is equivalent to*

$$\begin{pmatrix}\tilde{\zeta}_{cl}^\top & \bar{w}^\top\end{pmatrix}\begin{pmatrix}\bar{A}_1 & 0 & \dots\\ 0 & \ddots & \\ \vdots & & \bar{A}_N\end{pmatrix}\begin{pmatrix}\tilde{\zeta}_{cl}\\ \bar{w}\end{pmatrix}<0.\tag{6.42}$$

We now apply a congruence transformation to (6.41) *as*

$$\begin{aligned}
&\begin{pmatrix} T_3 & 0 \\ 0 & I \end{pmatrix} \begin{pmatrix} A_{cli}P + PA_{cli} + \alpha P & B_{cl} \\ B_{cl}^{\top} & -\alpha \end{pmatrix} \begin{pmatrix} T_3^{\top} & 0 \\ 0 & I \end{pmatrix} \\
&= \begin{pmatrix} He[T_3 A_{cli} P T_3^{\top}] + \alpha T_3 P T_3^{\top} & T_3 B_{cl} \\ B_{cl}^{\top} T_3^{\top} & -\alpha \end{pmatrix} < 0,
\end{aligned} \tag{6.43}$$

with $T_3 = \begin{pmatrix} Y & -S \\ I & 0 \end{pmatrix}$. *Taking* $P = \begin{pmatrix} X & X \\ X & S^{-1} + X \end{pmatrix}$, *enforcing* $XY - XS = I$, *and substituting for* $\bar{A}_i, \bar{B}$, (6.43) *can be written as*

$$\begin{pmatrix} \Phi_{1,1} & \Phi_{1,2} & -YB \\ \Phi_{1,2}^{\top} & \Phi_{2,2} & -B \\ -B^{\top}Y & -B^{\top} & -\alpha \end{pmatrix}_i < 0, \tag{6.44}$$

with

$$\begin{aligned}
\Phi_{1,1} &= YA + A^{\top}Y - \lambda_i He[SB_cC + YBD_cC], \qquad (6.45) \\
\Phi_{1,2} &= Y[A + BC_c + \lambda_i BD_cC]X - S[\lambda_i B_cC + A_{ci}]X \\
&\quad + A^{\top} + \lambda_i C^{\top} D_c^{\top} B^{\top}, \\
\Phi_{2,2} &= AX + XA^{\top} + He[BC_cX + \lambda_i BD_cCX],
\end{aligned}$$

While (6.44) *is not linear in terms of the unknowns* $X, Y, S, A_{ci}, B_c, C_c, D_c$, *we intro-*

duce the variables

$$\begin{aligned} W_o &= -SB_c + YBD_c, \\ W_c &= (C_c + D_cC)X, \\ L_i &= Y[A + BC_c + BD_cC]X - S[\lambda_i B_cC + A_{ci}]X \\ &= YAX + YBW_c + \lambda_i W_oCX - SA_{ci}X, \end{aligned} \tag{6.46}$$

for $i = 1, ..., N$*, to render the search linear.*

Incorporating the new variables (6.46)*, the inequality* (6.44) *converts to* (6.33) *which is a linear matrix inequality with* D_c, X, Y, W_c, W_o, L_i *as unknowns. The controllers' matrices* A_{ci}, B_c, C_c, D_c *are the achieved from* (6.31)*.*

For performance measure, we follow the sketch of the proof of Theorem 6.3.1. Given the disturbance bound

$$\bar{w}^\top(t)\bar{w}(t) \leq w_{max}^2, \quad \forall t \geq 0, \tag{6.47}$$

and the performance output $z_i = C_z\tilde{\zeta}_{cli}$ *for each agent, the performance measure* $z^\top z \leq \chi^2$ *with* $z = [z_1^\top ... z_N^\top]^\top$*, is guaranteed by*

$$\begin{pmatrix} P & PC_z^\top \\ C_zP & \frac{\chi^2}{w_{max}^2} \end{pmatrix} > 0. \tag{6.48}$$

Applying the congruence transformation

$$\begin{pmatrix} T_3 & 0 \\ 0 & I \end{pmatrix} \begin{pmatrix} P & PC_z^\top \\ C_zP & \frac{\chi^2}{w_{max}^2} \end{pmatrix} \begin{pmatrix} T_3^\top & 0 \\ 0 & I \end{pmatrix} \tag{6.49}$$
$$= \begin{pmatrix} T_3PT_3^\top & T_3PC_z^\top \\ C_zPT_3^\top & \frac{\chi^2}{w_{max}^2} \end{pmatrix} < 0,$$

and substituting for P and T_3, it can be shown that (6.49) *is equivalent to the right hand side inequality in* (6.34)*, guaranteeing a performance level χ.*

6.5 Anti-Windup Compensation

Consider the error dynamics (6.27), and the unconstrained output feedback controller (6.28). We assume that agents' actuators have magnitude limits and commands sent to the actuators should not exceed these bounds; i.e., for every input, we require

$$|u_{pi}| \leq \mathsf{m}_i, \tag{6.50}$$

where $\mathsf{m}_i > 0$ are known constants.

Figure 6.1 shows the schematic of the augmented control system in terms of a block diagram. Our objective is to obtain suitable additive signals $v_1 \in \mathbb{R}^{n_c}$ and $v_2 \in \mathbb{R}^{n_u}$

to the unconstrained controller (6.28), i.e., rendering the compensator as

$$\begin{aligned}\dot{\zeta}_{ci} &= A_{ci}\zeta_{ci} + B_c\bar{y}_i + v_{1i},\\ u_i &= C_c\zeta_{ci} + D_c\bar{y}_i + v_{2i},\end{aligned} \tag{6.51}$$

such that the closed-loop system is internally stable with a guaranteed input-output performance measure γ.

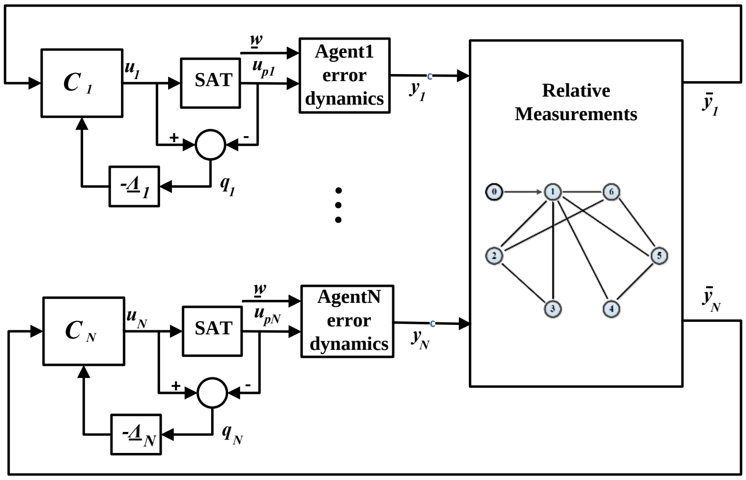

Figure 6.1: Output feedback control system with anti-windup augmentations.

The static anti-windup block containing matrix gain $\mathrm{AW}(q_i) = -\underline{\Delta}_i q_i$, is applied to the dead-zone function

$$q_i = \mathrm{dz}(u_i) = u_i - \mathrm{sat}_m(u_i) = u_i - u_{pi}. \tag{6.52}$$

The AW additive terms v_{1i} and v_{2i} are then given by

$$v_{1i} = -[I_{n_c} \quad 0](\underline{\Delta}_i q_i), \quad v_{2i} = -[0 \quad I_{n_u}](\underline{\Delta}_i q_i). \tag{6.53}$$

Following standard techniques explained in e.g. [50, 52], with the error dynamics (6.27) , controller (6.28) and (6.52) , it is straightforward to build the augmented system with state vector $x = [x_1^\top, ..., x_N^\top]$, where $x_i = [\zeta_i^\top \quad \zeta_{ci}^\top]^\top \in R^n$, and $\underline{w}$ and q as input signals. Given the error dynamics (6.27) and the compensated output feedback controller (6.51), the closed-loop system with magnitude AW gains can be written as

$$
\begin{aligned}
\dot{x} &= Ax + B_w \underline{w} + (B_q - B_\eta \underline{\Delta})q, \\
u &= C_u x - D_{u\eta} \underline{\Delta} q, \\
z &= C_z x,
\end{aligned}
\tag{6.54}
$$

with $\underline{\Delta} = \operatorname{diag}(\underline{\Delta}_i)$ and system matrices

$$
\left[\begin{array}{c} A \\ \hline B_\eta \\ \hline C_z \\ \hline C_u \end{array}\right] = \left[\begin{array}{cc} I_N \otimes A + \mathscr{L}_1 \otimes BD_cC & I_N \otimes BC_c \\ \mathscr{L}_1 \otimes BC_c & \operatorname{diag}(A_{ci}) \\ \hline I_N \otimes B[0 \quad I_{n_u}] & I_N \otimes [I_{n_c} \quad 0] \\ \hline I_N \otimes C & 0 \\ \hline \mathscr{L}_1 \otimes D_cC & I_N \otimes C_c \end{array}\right], \tag{6.55}
$$

$$
\left[\begin{array}{c|c} B_w & B_q \\ \hline D_{u\eta} & \end{array}\right] = \left[\begin{array}{c|c} -\mathbf{1} \otimes B & -I_N \otimes B \\ 0 & 0 \\ \hline I_N \otimes [0 \quad I_{n_u}] & \end{array}\right],
$$

Using the sector condition defined in Notations, the anti-windup augmentation with static gain $\underline{\Delta}$ is designed by the following Theorem.

Theorem 6.5.1 (Anti-windup Compensation for Distributed Tracking Control with Limited Inputs) *Consider the error dynamics* (6.27)*, and the unconstrained output feedback controller* (6.28)*. Given any solution to the optimization problem*

$$\min_{Q,M,X_i,\gamma^2} \quad \gamma^2 \tag{6.56}$$

subject to the Linear Matrix Inequalities

$$\begin{pmatrix} A_{cli}Q + QA_{cli}^\top + \alpha Q & * & * \\ B_w & -\alpha I & * \\ \Phi_{3,1} & 0 & \Phi_{3,3} \end{pmatrix}_i < 0, \tag{6.57}$$

where

$$\begin{aligned} \Phi_{3,1i} &= MB_q^\top - X_i^\top B_\eta^\top + C_u Q, \\ \Phi_{3,3i} &= -2M - D_{u\eta}X_i - X_i^\top D_{u\eta}^\top, \end{aligned} \tag{6.58}$$

for $i = 1,...,N$ *and*

$$\begin{pmatrix} Q & QC_z^\top \\ C_z Q & \gamma^2/w_{max}^2 \end{pmatrix} > 0. \tag{6.59}$$

Then, with $\underline{\Lambda}_i = X_i M^{-1}$ *for* $i = 1,...,N$*, the closed-loop system* (6.54) *has reachable* *set*

$$x(t) \in \mathscr{E}(Q^{-1}, w_{max}^2), \tag{6.60}$$

and performance measure γ from w to z.

Proof 6.5.1 *Following the sketch of proof of Theorem 6.4.1, let $U \in \Re^{N\times N}$ be a unitary matrix such that $U^\top \mathscr{L}_1 U = \Lambda = diag(\lambda_i)$, $\bar{x} = (U^\top \otimes I_N)x$, $\bar{q} = (U^\top \otimes I_N)q$ and $\bar{w} = (U^\top \otimes I_N)w$. It is straightforward to show that the closed-loop dynamics* (6.54)*, after a few row/column manipulations can be written as*

$$\begin{aligned}
\dot{\bar{x}} &= diag(\begin{bmatrix} A+\lambda_i BD_cC & BC_c \\ \lambda_i B_cC & A_c \end{bmatrix})\bar{x} + (I_N \otimes \begin{bmatrix} -B \\ 0 \end{bmatrix})\bar{w} \\
&+ (I_N \otimes \begin{bmatrix} -B \\ 0 \end{bmatrix})\bar{q} - (I_N \otimes \begin{bmatrix} B[0 \quad I_{nu}] \\ [I_{nc} \quad 0] \end{bmatrix})\underline{\Delta\bar{q}} = \\
&diag(A_{cli})\bar{x} + (I_N \otimes \bar{B}_w)\bar{w} + (I_N \otimes \bar{B}_q)\bar{q} - (I_N \otimes \bar{B}_\eta)\underline{\Delta\bar{q}},
\end{aligned} \tag{6.61}$$

$$\begin{aligned}
\bar{u} &= diag(\begin{bmatrix} \lambda_i D_cC & C_c \end{bmatrix})\bar{x} - (I_N \otimes [0 \quad I_{nu}])\underline{\Delta\bar{q}} \\
&= diag(\bar{C}_{ui})\bar{x} - (I_N \otimes \bar{D}_{u\eta})\underline{\Delta\bar{q}}
\end{aligned} \tag{6.62}$$

Consider the positive definite Lyapunov function

$$V = \bar{x}^\top (I_N \otimes Q^{-1})\bar{x}, \tag{6.63}$$

with $Q > 0$. For a peak bounded disturbance signal $\bar{w}$, recalling the sector condition

$u \longmapsto q \in [0,I] \Rightarrow q^\top W(q-u) \leq 0$ *and applying the S-procedure, the reachable set* (6.60) *is achieved if*

$$\dot{V} + \alpha(V - \bar{w}^\top \bar{w}) + 2\bar{q}^\top (I_N \otimes W)(\bar{u} - \bar{q}) < 0. \tag{6.64}$$

Taking the derivative of V along the closed-loop dynamics and following the sketch of proof of Theorem 6.4.1, (6.61) *is equivalent to*

$$\begin{pmatrix} Q^{-1}A_{cli} + A_{cli}^\top Q^{-1} + \alpha Q^{-1} & * & * \\ Q^{-1}\bar{B}_w & -\alpha I & * \\ \underline{\Phi}_{3,1} & 0 & \underline{\Phi}_{3,3} \end{pmatrix} < 0, \tag{6.65}$$

with

$$\begin{aligned} \underline{\Phi}_{3,1} &= \bar{B}_q^\top Q^{-1} - \underline{\Lambda}_i^\top \bar{B}_\eta^\top Q^{-1} + W\bar{C}_{ui}, \\ \underline{\Phi}_{3,3} &= -2W - W\bar{D}_{u\eta}\underline{\Lambda}_i - \underline{\Lambda}_i^\top \bar{D}_{u\eta}^\top W. \end{aligned} \tag{6.66}$$

At the first glance, (6.65) *is not linear in terms of the unknowns Q, W, and $\underline{\Lambda}_i$. Introducing $M = W^{-1}$ and $X_i = \underline{\Lambda}_i M$, and applying a few congruence transformations to* (6.66)*, it is straightforward to show that the inequality* (6.66) *is equivalent to the LMI* (6.57) *with unknowns Q, M, and X_i for $i = 1, \ldots, N$. The anti-windup gains are then achieved by*

$$\underline{\Lambda}_i = X_i M^{-1}, \quad i = 1, \ldots, N. \tag{6.67}$$

Remark 6.5.1 *Applying the elimination lemma to* (6.57)*, results in a set of LMIs requiring the open loop system to be stable. This is the same standard necessary condition in static anti-windup design for single agent cases. In order to relax this condition, the technique presented in e.g. [52] can be used alternatively to provide stability and performance guarantees. Further technical details are out of the scope of this thesis and considered as future work.*

6.6 Simulation Results

In order to examine the benefits of the results presented in this chapter, we apply the proposed controllers to a networked multi-agent system with communication graph 6.2. As mentioned before, the leader (agent 0) receives no information from the followers and its state is only available to agent 1. We borrow the numerical example used in [38] which solves the same problem using a nonlinear controller.

All agents are assumed to have unstable second order dynamics (6.1) with

$$A = \begin{bmatrix} 0 & 1 \\ -1 & 2 \end{bmatrix}, \quad B = \begin{bmatrix} 0 \\ 1 \end{bmatrix}. \tag{6.68}$$

A state feedback control $u_0 = K_0 x_0$ with $K_0 = [0 \quad -2]$ is selected providing an oscillatory closed-loop dynamics for the leader.

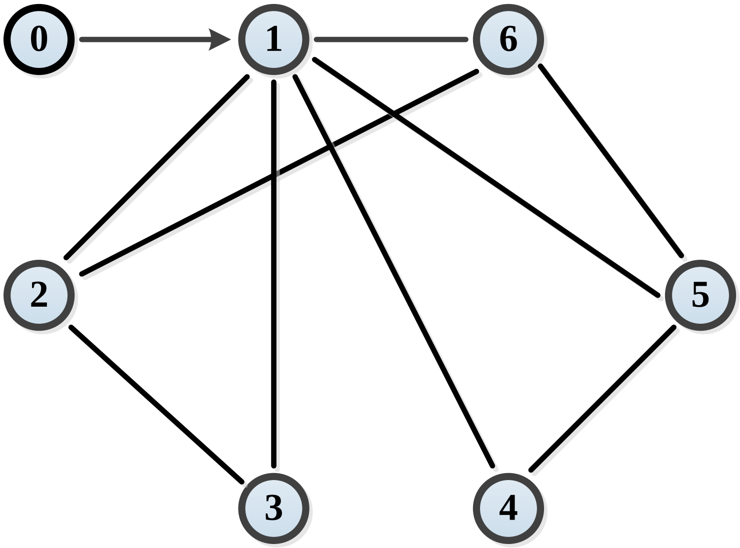

Figure 6.2: Communication graph.

The linear controller (6.4) is used with

$$K = \begin{bmatrix} -278.1988 & -108.9699 \end{bmatrix}, \tag{6.69}$$

solved from the LMIs in Theorem 6.3.2 using the MATLAB LMI solver tool, and $\alpha = 2.5$ selected based on a line search. Figure 6.3 shows that using the state feedback controller (6.4) the trajectories of the agents converge to the trajectory of the leader in less than 2 seconds which is much faster than the convergence rate achieved in [38] using a nonlinear controller.

As mentioned earlier, the controller used in (6.3), assumes the availability of all eigenvalues of the Laplacian matrix. In order to relax this condition, in this part we evaluate the results presented in Theorem 6.3.2. The linear controller (6.20) is used

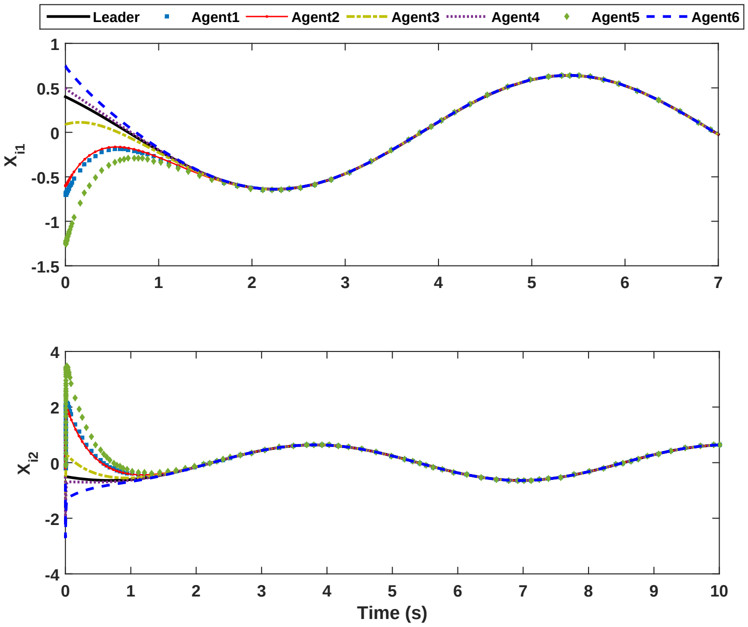

Figure 6.3: State trajectories of the leader (solid line) and 1-6 follower agents using the state feedback controller (6.4).

with

$$K = -B^{\top}P = \begin{bmatrix} -79.2854 & -15.8256 \end{bmatrix}, \tag{6.70}$$

and P from solving the LMIs using the MATLAB LMI solver tool. Figure 6.4 shows the trajectories for $c_1 = 0.1$ which is much lower than the limit $1/\lambda_1 = 7.18$. As expected, convergence would not be guaranteed. However, as shown in Fig. 6.4, by selecting $c_1 \geq 1/\lambda_1$ the trajectories of the agents converge to the trajectory of the leader in less than 1 seconds.

The maximum optimization iteration number for the controller (6.70) has been limited to 10 in order to avoid too large gains. However, by increasing this limit to 25

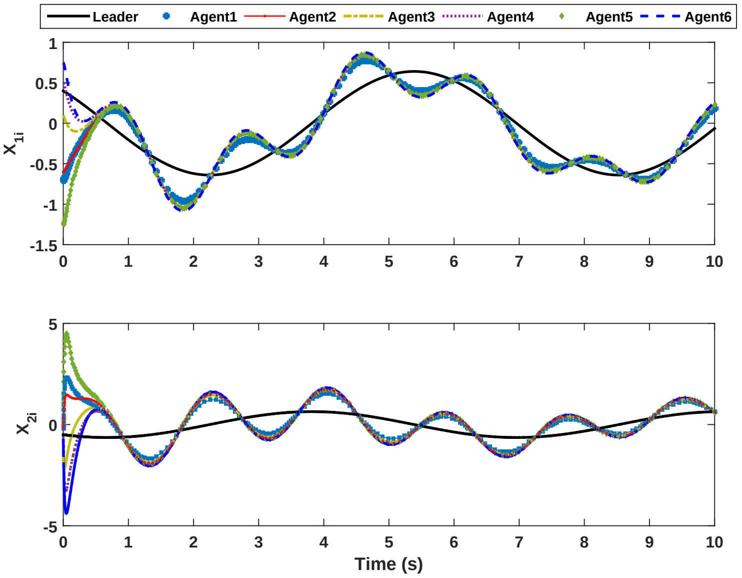

Figure 6.4: State trajectories of the leader (solid line) and 1-6 follower agents using the state feedback controller (6.20), with $K = -B^\top P$ and $c_1 = 0.1$.

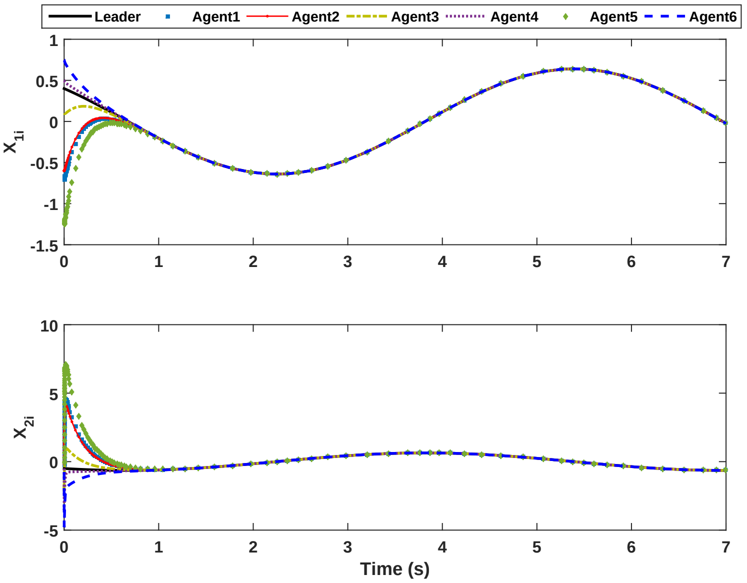

Figure 6.5: State trajectories of the leader (solid line) and 1-6 follower agents using the state feedback controller (6.20), with $K = -B^\top P$ and $c_1 = 1/\lambda_1$.

the performance level, i.e. peak-to-peak upper bound decreases to $\chi = 5.6259e-05$ from 0.2401, and as shown in Fig. 6.6 a much faster convergence compared to Fig. 6.5 is achieved in order of mili seconds. This is due the so called 'matched disturbance' nature of the problem. Possible limitation caused by large control signals could also be handled with the proposed anti-windup compensation technique (simulations omitted due to space limitation).

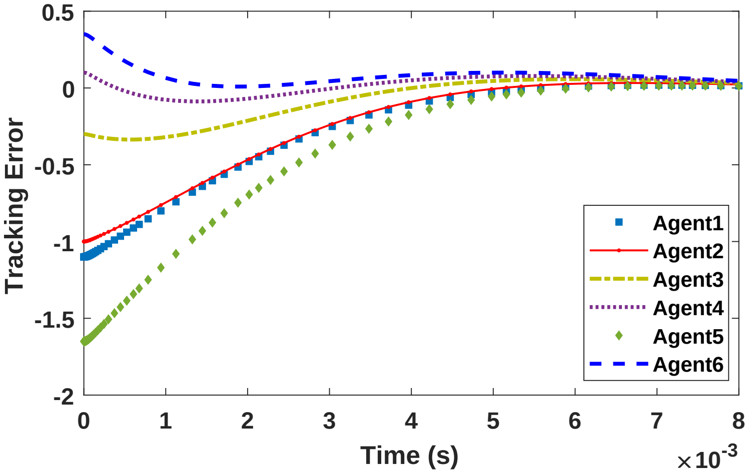

Figure 6.6: Tracking error of 1-6 follower agents using the state feedback controller with $K = 1e5[-4.1410 \quad -0.0081]$.

6.7 Conclusions

This chapter investigates the tracking problem for multi-agent systems with linear dynamics while assuming a nonzero input for the leader which is not available to any of the followers. The communication graph is assumed to be undirected with a directed path from the leader to all agents. A distributed linear state feedback as well as a general output feedback controller are designed based on the relative states and measurements of the neighboring agents, respectively. The performance of the controllers are optimized using the Lyapunov peak-to-peak approach. Finally, anti-windup augmentation technique is conducted in order to guarantee the stability of the network and improve the performance in case of actuator saturation.

Chapter 7

Summary and Conclusions

In this thesis I studied the issue of actuator amplitude and rate saturation due to the limited capacity of the device. Anti-windup augmentation technique is employed for situations in which saturation is not expected to occur frequently. Multiple anti-windup compensation designs are developed to guarantee the stability of the closed-loop system and an improved performance level in the presence of saturation under energy and peak bounded exogenous inputs.

The performance of the proposed techniques are evaluated on a few unconventional fields of application. First, a high temperature solid oxide fuel cell is studied as a clean and efficient source of electricity. The generated power of the fuel cell is maximized by enforcing artificial limits to system actuators and anti-windup augmentation is used to minimize the drawbacks of saturation. A 16% rise in usable power is achieved with minimal effects on spatial temperature gradients.

Second, the challenging issue of integrator overload is studied in a Delta-Sigma modulator as a common high resolution analog-to-digital converter. In order to increase the dynamic range of the modulator, the integrator overload is prevented using a saturation element and the performance of the system is recovered using anti-windup compensation. According to the simulations, a 50% higher dynamic range is achieved by avoiding the integrator overload at the cost of less than 1dB drop in SNDR.

Third, a specific leader-follower tracking problem is studied in multi-agents and the unknown input to the leader is treated as a disturbance signal. Using the peak-to-peak analysis, a linear state feedback controller is designed which performs as well as the nonlinear controller available in the literature. A centralized output feedback compensator is also designed which can be augmented with AW gains and address the issue of actuator saturation.

Bibliography

[1] K. Ahmed and K. Fger. Perspectives in solid oxide fuel cell-based micro-combined heat and power systems. *ASME. J. Electrochem. En. Conv. Stor.*, 14(3):031005–031005–12, 2017.

[2] M. A. Ansari, S. M. A. Rizvi, and S. Khan. Optimization of electrochemical performance of a solid oxide fuel cell using artificial neural network. In *International Conference on Electrical, Electronics, and Optimization Techniques*, Chennai, India, March 2016.

[3] S. Au and B. H. Leungn. A 1.95-v, 0.34-mw, 12-b sigma-delta modulator stabilized by local feedback loops. *IEEE Journal of Solid-State Circuits: Fundamental Theory and Applications*, 32(3):321–328, 1997.

[4] C. Barbu, R. Reginatto, A. R. Teel, and L. Zaccarian. Anti-windup for exponentially unstable linear systems with inputs limited in magnitude and rate. pages 1230–1234, Chicago, IL, June 2000.

[5] A. Bateman and Z. Lin. An analysis and design method for linear systems under nested saturation. 48(1):41–52, 2003.

[6] S. Boyd, L. E. Ghaoui, E. Feron, and V. Balakrishnan. *Linear Matrix Inequalities in System and Control Theory*. 1st edition, 1994.

[7] Y. Cao and W. Ren. Distributed coordinated tracking with reduced interaction via a variable structure approacht. *IEEE Trans. Automatic Control*, 57(1):33–38, 2012.

[8] Y. Y. Cao and Z. Lin. An anti-windup design for polytopic systems by a parameter-dependent lyapunov function approach. 37(2):129–139, 2006.

[9] A. Chaudhari, A. Plianos, and R. Stobart. Development of model predictive controller for sofc-ic engine hybrid system. *SAE Int. J. Engines*, 2(1):56–99, 2009.

[10] J. Chen, H. Zhang, and S. Weng. Study on nonlinear identification SOFC temperature model based on particle swarm optimizationleast-squares support vector regression. *ASME. J. Electrochem. En. Conv. Stor.*, 14(3):031003–031003–10, 2017.

[11] D. Crunkleton and R. Strattan. Fuel economy and emission performance of fuel cell-based diesel HEVs. *ASME. J. Fuel Cell Sci. Technol.*, 5(1):011013–011013–5, 2008.

[12] J. M. G. da Silva and S. Tarbouriech. Anti-windup design with guaranteed regions of stability: An lmi-based approach. 50(1):106–111, 2005.

[13] N. Dekker and G. Rietveld. Highly efficient conversion of ammonia in electricity by solid oxide fuel cells. *ASME. J. Fuel Cell Sci. Technol.*, 3(4):499–502, 2006.

[14] R. C. Dorf and R. H. Bishop. *Modern Control Systems*. 11th edition, 2008.

[15] M. Fardadi, F. Mueller, and F. Jabbari. Feedback control of solid oxide fuel cell spatial temperature variation. *Journal of Power Sources*, 195(13):4222–4233, 2010.

[16] J. A. Fax and R. M. Murray. Information flow and cooperative control of vehicle formations. *IEEE Trans. Automatic Control*, 49(9):1465–1476, 2004.

[17] F. Forni, S. Galeani, and L. Zaccarian. Model recovery anti-windup for continuous-time rate and magnitude saturated linear plants. 48(8):1502–1513, 2012.

[18] S. Galeani, S. Onori, A. R. Teel, and L. Zaccarian. Further results on static linear anti-windup design for control systems subject to magnitude and rate saturation. pages 6373–6378, San Diego, CA, December 2006.

[19] S. Galeani, S. Onori, A. R. Teel, and L. Zaccarian. A magnitude and rate saturation model and its use in the solution of a static anti-windup problem. 57(1):1–9, 2008.

[20] Z. Gallehdari, N. Meskin, and K. Khorasani. Adaptive cooperative output tracking control for input and output constrained multiagent systems with actuator faults. pages 745–750, Boston, MA, July 2016.

[21] Z. Gallehdari, N. Meskin, and K. Khorasani. Control reconfiguration for multiple autonomous vehicles subject to actuator faults and disturbance. pages 1924–1929, Boston, MA, July 2016.

[22] G. Grimm, J. Hatfield, I. Postlethwaite, A. R. Teel, M. C. Turner, and L. Zaccariani. Anti-windup for stable linear systems with input saturation: An lmi based synthesis. 48(9):1509–1525, 2003.

[23] Y. Hong, G. Chen, and L. Bushnell. Distributed observers design for leader-following control of multi-agent networks. *Automatica*, 44(3):846–850, 2008.

[24] T. Hu, Z. Lin, and B. M. Chen. Analysis and design for discrete-time linear systems subject to actuator saturation. 45(2):97–112, 2002.

[25] T. Hu, A. R. Teel, M. C. Turner, and L. Zaccarian. Nonlinear $\mathscr{L}_2$ gain and regional analysis for linear systems with anti-windup compensation. pages 3391–3396, Portland, OR, June 2005.

[26] T. Hu, A. R. Teel, M. C. Turner, and L. Zaccarian. Regional anti-windup compensation for linear systems with input saturation. pages 3397–3402, Portland, OR, June 2005.

[27] T. Hu, A. R. Teel, and L. Zaccarian. Anti-windup synthesis for linear control systems with input saturation: Achieving regional, nonlinear performance. 44(2):512–519, 2008.

[28] H. Huo, Y. Wu, Y. Liu, S. Gan, and X. Kuang. Control-oriented nonlinear modeling and temperature control for solid oxide fuel cell. *ASME. J. Fuel Cell Sci. Technol.*, 7(4):0410051–0410051–9, 2010.

[29] F. Jabbari and I. Kose. Rate and magnitude-bounded actuators: Scheduled output feedback design. 14(13), 2004.

[30] W. Jiang, Y. Luo, W. Zhang, W. Woo, and S. Tu. Effect of temperature fluctuation on creep and failure probability for planar solid oxide fuel cell. *ASME. J. Fuel Cell Sci. Technol.*, 12(5):051004–051004–10, 2015.

[31] H. K. Khalil. *Nonlinear Systems*. 3rd edition, 2002.

[32] S. Kia and F. Jabbari. Controllers for linear systems with bounded actuators: Slab scheduling and anti-windup. *Automatica*, 49(3):762–769, 2013.

[33] S. S. Kia and F. Jabbari. Multi-stage anti-windup compensation for open loop stable plants. 56(9):2166–2172, 2011.

[34] G. Kopasakis, T. Brinson, and S. Credle. A theoretical solid oxide fuel cell model for system control and stability design. *ASME. J. Fuel Cell Sci. Technol.*, 7(4):041007–041007–8, 2008.

[35] M. V. Kothare, P. J. Campo, M. Morari, and C. N. Nett. A unified framework for the study of anti-windup designs. 30(12):1869–1883, 1994.

[36] A. Leone and P. Lanzini. Experimental modeling of transients in large SOFC systems. *ASME. J. Fuel Cell Sci. Technol.*, 10(1):011004–011004–11, 2013.

[37] Z. Li, Z. Duan, G. Chen, and L. Huang. Consensus of multiagent systems and synchronization of complex networks: A unified viewpoint. *IEEE Trans. Circuit Syst. I: Reg. Papers*, 57(1):213–224, 2010.

[38] Z. Li, X. Liu, and W. Ren. Distributed tracking control for linear multiagent systems with a leader of bounded unknown input. *IEEE Trans. Automatic Control*, 58(2):518–523, 2013.

[39] Z. Lin. Semi-global stabilization of discrete-time linear systems with position and rate-limited actuators. 34(5):313–322, 1998.

[40] A. Marques, V. Peluso, M. S. Steyaert, and W. M. Sansen. Optimal parameters for modulator topologies. *IEEE Trans. Circuit Syst. II: Analog and Digital Signal Processing*, 49(9):1232–1241, 1998.

[41] I. Masubuchi, A. Ohara, and N. Suda. Lmi-based controller synthesis: A unified formulation and solution. *Int. J. Robust and Nonlinear Control*, 8(8):669–686, 1998.

[42] F. Mueller, F. Jabbari, and J. Brouwer. Control design for a bottoming solid oxide fuel cell gas turbine hybrid system. *ASME. J. Fuel Cell Sci. Technol.*, 4(3):221–230, 2006.

[43] F. Mueller, F. Jabbari, R. Gaynor, and J. Brouwer. Novel solid oxide fuel cell controller for rapid load following. *Journal of Power Sources*, 172(1):308–323, 2007.

[44] E. F. Mulder, M. V. Kothare, and M. Morari. Multivariable anti-windup controller synthesis using linear matrix inequalities. 37(9):1407–1416, 2001.

[45] A. Narjiss, D. Depernet, F. Gustin, D. Hissel, and A. Berthon. Design of a high efficiency fuel cell dc/dc converter dedicated to transportation applications. *ASME. J. Fuel Cell Sci. Technol.*, 5(4):041004–041004–11, 2008.

[46] T. Nguyen and F. Jabbari. Output feedback controllers for disturbance attenuation with actuator amplitude and rate saturation. 36(9):1339–1346, 2000.

[47] R. Olfati-Saber, J. A. Fax, and R. M. Murray. Consensus and cooperation in networked multi-agent systems. *in Proceedings of the IEEE*, 95(1):215–233, 2007.

[48] M. S. Reineh and F. Jabbari. Use of anti-windup techniques for control of solid oxide fuel cells. Charleston, SC, November 2016.

[49] M. S. Reineh and F. Jabbari. Thermal control of SOFC: An anti-windup approach for maximizing usable power. In *IEEE Conference on Control Technology and Applications*, Kohala Coast, HI, August 2017.

[50] M. S. Reineh, S. Kia, and F. Jabbari. Multi-stage anti-windup for LTI systems with actuator magnitude and rate saturation. pages 5455–5460, Boston, MA, July 2016.

[51] M. S. Reineh, S. Kia, and F. Jabbari. Anti-windup designs for systems with amplitude and rate bounded actuators. In *20th IFAC World Congress*, Toulouse, France, July 2017.

[52] M. S. Reineh, S. Kia, and F. Jabbari. Anti-windup designs for systems with magnitude and rate bound actuators. pages 11509–11514, Tolouse, France, July 2017.

[53] B. Restrepo, D. Tucker, and L. Banta. Recursive system identification and simulation of model predictive control based on experimental data to control the cathode side parameters of the hybrid fuel cell/gas turbine. *ASME. J. Electrochem. En. Conv. Stor.*, 14(3):031004–031004–16, 2017.

[54] J. Sofroni, M. Turner, and I. Postlethwaite. Anti-windup synthesis for systems with rate-limits using riccati equations. 83(2):233–245, 2000.

[55] H. Su, M. Z. Q. Chen, and J. Lam. Semi-global leader-following consensus for linear multi-agent systems with input saturation via low gain feedback. *IEEE Trans. Circuit Syst. I: Reg. Papers*, 60(7):1881–1889, 2013.

[56] Y. H. L. T. C. Wang and C. C. Liu. A 0.022 mm^2 98.5 db sndr hybrid audio $\delta\sigma$ modulator with digital eld compensation in 28 nm cmos. *IEEE Journal of Solid-State Circuits: Fundamental Theory and Applications*, 50(11):2655–2664, 2015.

[57] A. Tsai, L. Banta, D. Tucker, and R. Gemmen. Multivariable robust control of a simulated hybrid solid oxide fuel cell gas turbine plant. *ASME. J. Fuel Cell Sci. Technol.*, 7(4):041008–041008–9, 2010.

[58] F. Tyan and D. S. Bernstein. Dynamic output feedback compensation for linear systems with independent amplitude and rate saturations. 67(1):89–116, 1997.

[59] Y. Wang, J. Siegel, and A. Stefanopoulou. Control strategies for power quantized solid oxide fuel cell hybrid powertrains: In mobile robot applications. *SAE Int. J. Alt. Power.*, 5(1):58–67, 2016.

[60] L. Yao, M. Steyaert, and W. Sansen. *Low-Power Low-Voltage Sigma-Delta Mlators in Nanometer CMOS*. 1st edition, 2006.

[61] A. Yeknami, F. Qazi, and A. Alvandpour. Low-power dt modulators using sc passive filters in 65 nm cmos. *IEEE Trans. Circuit Syst. I: Reg. Papers*, 61(2):358–370, 2014.

[62] S. Yu, T. Fernando, and H. Iu. Dynamic behavior study and state estimator design for solid oxide fuel cells in hybrid power systems. *IEEE Transactions on Power Systems*, 31(6):5190–5199, 2010.

[63] V. Zaccaria, Z. Branum, and D. Tucker. Fuel cell temperature control with a precombustor in SOFC gas turbine hybrids during load changes. *ASME. J. Electrochem. En. Conv. Stor.*, 14(3):031006–031006–8, 2017.

[64] L. Zaccarian and A. R. Teel. *Modern Anti-windup Synthesis*. 1st edition, 2011.

[65] H. Zare-Hoseini, I. Kale, and O. Shoae. Modeling of switched-capacitor delta-sigma modulators in simulink. *IEEE Trans. on Instrumentation and Measurement*, 54(4):1646–1654, 2003.

[66] H. Zhang, F. L. Lewis, and A. Das. Optimal design for synchronization of cooperative systems: State feedback, observer and output feedback. *IEEE Trans. Automatic Control*, 56(8):1948–1952, 2011.

[67] K. Zhou and J. Doyle. Fundamentals of robust control. *Prentice-Hall*.

[68] T. Zourntos and D. A. Johns. Variable-structure compensation of delta-sigma modulators: Stability and performance. *IEEE Trans. on Circuits and Systems I: Fundamental Theory and Applications*, 49(1):41–53, 2002.